POLITECNICO DI MILANO

FACOLTA' DI INGEGNERIA

CORSO DI LAUREA IN INGEGNERIA CIVILE
INDIRIZZO STRUTTURE
LAUREA MAGISTRALE

NUMERICAL AND EXPERIMENTAL ANALYSIS OF PEAK PRESSURE LOADS ON RECTANGULAR BUILDING

Supervisor:

Prof. Alberto Zasso
Prof. Federico Perotti
Prof. Tetsuro Tamura

Assistant supervisor:

Ing. Paolo Schito
Ing. Stefano Giappino
Ing. Giuseppe Vazzana

By:

Luca Amerio
mat. 787784

July 2014

A nonno Angelo

Contents

List of Figures

List of Tables

Abstract

The current state-of-the-art for the design of buildings' façade relies mainly on the prescription given by national codes. These prescriptions, even if valid for ordinary building, are often not detailed enough for the design of building out of the ordinary. For these buildings, designers that want to have a deeper knowledge of the wind pressures on the building and on the building elements can only rely on the wind tunnel tests.

CFD techniques are nowadays not sufficiently reliable for the evaluation of localised peak pressures. CFD however offers several benefits, such as an easier analysis of the flow without the need of acquisition instrumentation or an easier model geometry manipulation. The definition of a reliable standardised method for the calculation of design loads using CFD would allow to reduce the building façades oversize; reducing the cladding cost.

Sommario

Lo stato dell'arte attuale per la progettazione delle facciate degli edifici si affida principalmente alle prescrizioni fornite dalle normative nazionali. Queste normative, sebbene valide per edifici ordinari, sono spesso non sufficientemente dettagliate per il progetto di edifici di natura straordinaria. Per questi ultimi, il progettista che desiderasse una conoscenza più approfondita delle pressioni generate dal vento sui singoli elementi può fare affidamento solamente sulle prove in galleria del vento.

La tecniche CFD, al giorno d'oggi, non sono sufficientemente affidabili per la valutazione dei picchi di pressione localizzati. La CFD però offre diversi vantaggi, come un'analisi più facile del flusso senza la necessità di strumenti di acquisizione o una più facile manipolazione della geometria del modello. La definizione di un metodo affidabile e standardizzato per il calcolo dei carichi eolici con la CFD permetterebbe di ridurre il sovradimensionamento delle facciate, riducendo i costi dei rivestimenti degli edifici.

Chapter 1

Introduction

The accuracy of wind loading calculations has a considerable effect on the sizing of many structural elements.

The surface pressures caused by the interaction between the wind and the structure can lead to many different kinds of collapse mechanism, some local and some global. For instance, the external surface pressure can be a major design consideration to determine the glass thickness and glass selection in façades. The recent trend to cover entire buildings, both high-rise and low-rise, with glass façades increased the interest in the calculation of the wind loads on these elements. A façade can be up to 25% of the total building costs, being the average cost of a façade approximately \$700 per m^2, possibly reaching \$2500 per m^2 for high specification façades. Thus, a failure can cause considerable economic damages.

In addition, there are various safety implications related to glazing design such as glass breakage due to imposed dynamic pressures or flying debris and the possible domino effect in façade failure caused by the breakage of a single glass panel. Furthermore, windstorms account for about 70% of total insured losses and a direct link is apparent between major storms and world wide insurance losses from major natural disasters. It is therefore evident that an accurate method for determining wind loading on façades is essential for ensuring a safe and economic glazing design.

Another important issue that has led to several failures and collapses is

the calculation of the internal pressure. In some long span roof buildings, such as hangars, the sudden or periodic variations of the internal pressure can cause an important variations of the loading of some structural elements and lead to the local, or even global, collapse of the whole structure.

However, there are often several discrepancies between the existing guidelines available for determining wind loading on façades in different countries. These codes of practice are based upon generic building geometries and simplified models of wind loading and great accuracy cannot be expected from them. Because of this, in case of special buildings that cannot be described using simple geometries or that do not fit in any standard category, the codes themselves often suggest using *proven and/or properly validated methods*. Nowadays these *methods* are mainly wind tunnel tests. However, they present various issues.

The first problem is that a proper scaling that allows to reproduce exactly the same fluid-dynamic condition (same Reynolds number) is not possible as it would require incredibly fast flows inside the wind tunnel. The problem is therefore minimized using the fastest velocity that is possible to achieve in the wind tunnel, assuming phenomena not to be *Reynolds dependent*. However, this hypothesis is not always true. Another issue in the wind tunnel is the ability to reproduce correctly as many details as possible. Small details, such as gutters or balconies, can heavily alter the flow pattern. Using a large scale model makes the reproduction of smaller details easier, but might increase the blockage ratio of the Wind Tunnel to unacceptable levels. A third problem with the experimental approach is the spatial resolution of the acquired data. The surface pressure is usually measured by ducting the pressure through tubes from holes in the surface, known as tappings. This method creates a knowledge of the surface pressure pattern that is poorly spatially resolved; the usual density of pressure taps is about one every $10m^2$. A further problem is that it has been proven that the surface pressures obtained from wind tunnel testing are very sensitive to the successful simulation of the natural wind flow. This involves the artificial "growing" of the Atmospheric Boundary Layer (ABL) by modelling artificial ground roughness in order to develop the required turbulence levels.

Although wind tunnel testing is an established technique widely used in wind engineering, it is still a simulation prone to error and must therefore be benchmarked. Comparisons between full-scale tests on existing buildings and wind tunnel tests have shown good correlation although discrepancies do exist.

The Computational Fluid Dynamic (CFD) offers little advantage over experimental tests when overall wind forces for building stability calculations are required. However, when the detailed and localised flow structure is required, such as when pressures are required for façade design or when the flow pattern is important to study the pollution dispersion, the set up used in experimental techniques becomes complicated and the design loading data is very sensitive to errors in localised pressures. In such cases, numerical methods can be useful for determining the detailed flow characteristics, like pressure and velocity distributions.

Hence, a properly validated CFD method would allow us to overcome most of these problems. For example, in a CFD simulation the building could be reproduced with the full-scale dimensions and modelling every small detail of the building. Moreover, the flow variables are extremely easy to extract in any point of the domain without affecting the flow pattern in any way.

CFD however presents other problems that are currently being investigated. Unfortunately, in flows above a particular Reynolds number (governed by fluid density, velocity and viscosity), the fluid motion is turbulent and apparently random. To correctly reproduce this turbulence the correct simulation of the turbulence power spectrum is needed. It has been proved by the Russian scientist Andrej Kolmogorov that the viscous contribution shows up in the smallest turbulence scales that, for civil applications, are in the order of magnitude of $10^{-6}m$. To solve such small scales would require an enormous computational power. E.g. to simulate the flow around a $100m$ tall and $30m$ wide building would require a number of cells with an order of magnitude equal to 10^{25} or even larger, each one with several variables stored in it. Such a large number of variables is not nowadays affordable by existing computers.

In the past decades, the CFD research focused on the investigation of

turbulence models. These models try to correctly reproduce the larger scale of the flow - which are relevant for engineering problems, without having to reproduce the smaller scales. The most common and widely validated approach is the Reynolds-averaged Navier-Stokes equations' (RANS) model. Instantaneous flow velocities are divided into mean and fluctuating components, which are replaced into the equations of motion. The mean components are then solved with the usual Navier-Stokes equations' while the fluctuating ones are *modelled*. Several turbulence models are available, some much more widely validated than others, such as the $k - \varepsilon$ model. Easom (2000) provides a comprehensive review of different turbulence models relevant to computational wind engineering. This solution however does not allow to directly simulate the pressure variations. When only the mean value of the pressure is required, such approach produces good results. This is the case when overall wind force on a given surface is required for a quasi-static analysis, as the effects of localised differences of wind pressure on the building surface tend to cancel each other.

When the main interest is the peak value or the dynamic variation of the pressure, the RANS method is unsuitable. An intermediate approach that allows to reproduce the time-variation of the flow has been developed: the Large Eddies Simulation (LES) method.

This method allows to directly resolve the fluctuating large turbulent eddies, while still relying on turbulence models to compute the less significant small-scale turbulence. The main hypothesis that lies at the base of this technique is that the small scales turbulent structures are identical for any flow with any boundary condition. This topic will be discussed in section 3.2.

Another discussed CFD issue is the inlet boundary condition. It has been demonstrated that CFD results are as sensitive to the inlet boundary conditions as wind tunnel tests are.

There are two main approaches to this problem. The first approach is to "attach" to the building domain a rough *driver region* where the wind flows above some arbitrary ground roughness to evolve in a correct ABL profile. This approach is very similar to the one used in the wind tunnel

placing the artificial roughness on the floor to obtain a correct incoming flow. The flaw of this method is that it further increases the size of the domain causing more computational power to be necessary. Some *recycle* techniques, such as the Lund (1998) or the Kataoka and Mizuno (2002) techniques, have been developed to reduce the driver region length. A second approach is to use an inlet flow with a synthetic overlying turbulence. These techniques allow to drastically reduce the domain size, but the generation of the synthetic turbulence has proved to be very tricky. Artificial flows that are not completely physically correct decay rapidly and then evolve again in a turbulent flow i.e. if the turbulence is not correctly generated, the boundary layer is not stable. The correct turbulent inlet condition is proving to be elusive, but encouraging results have been recently obtained.

The main target for the CFD applied to civil engineering research at the moment is to produce a proven procedure or a code that allows to *thrust* a simulation result without the need of a benchmark. At the moment the AIJ (Architectural Institute of Japan) is redacting a code for the wind analysis using CFD method.

With regard to both wind tunnel and CFD tests, a common problem is that the outputs generated are time-discrete pressure time-history. What the designer needs to correctly design the façade is a single design value. This value represent the maximum wind load that is expected to happen during the lifetime of the structure and that is expected to be tolerated without damage. The determination of this value starting from the time-histories is not straightforward. The nature of the phenomena makes the probability density function of the pressure to be non-Gaussian, moreover the definition of *peak* itself is not obvious. Provided that these problems have been addressed, the random nature of the wind makes it necessary to determine the minimum duration of the test (both experimental or numerical) needed to compute this maximum value with sufficient accuracy. There have been many proposals about this topic that will be analysed in Chapter 6; a satisfactory review of the most used ones has been done by **?**.

In the case of glazed façades the problem is even more complex. The research since the '80s showed that when glass panels are subjected to high

loads, the relationship between the applied loads and the resulting stresses becomes non-linear. They also have shown that the strength of glass varies with load duration and glass size. The molecular structure of glass cause damage accumulation phenomena to occur due to the propagation of microscopic cracks on the glass surface. Other phenomena also occur, such as the *healing* of cracks with an increase in resistance of the glass component and the interaction between the molecular structure of glass and the water that penetrate the cracks. (Haldimann, 2006). These features make the wind load even more critical and demanding.

The aim of this thesis is a numerical-experimental evaluation inherent part of the sizing of the façades, aimed at identifying the main critical points / opportunities offered by High Performance Computing (HPC) techniques applied to a wind-structure interaction case.

Chapter 2 will introduce the study of the wind, from its causes to the quantities that characterise it. Computation Fluid Dynamic and the numerical techniques, used to simulate the fluids behaviour, are reviewed in chapter 3. Here the main problems in the simulation of the turbulence will be also summarized together with the present models to workaround these problems. In chapter 4 the test executed in the Politecnico di Milano Wind Tunnel will be presented, describing both the test equipment and the obtained results. Subsequently chapter 5 will show the simulations carried out to reproduce the Wind Tunnel experiments; in the first part of the chapter the initial benchmark executed to validate the model will be presented, later on the wind tunnel and a building simulation are illustrated. Finally, in chapter 6, an overview of the present methods for the estimation of the peak pressure is discussed and, then, applied to the CFD and the Wind Tunnel results.

Chapter 2

The wind

The correct simulation of wind load on the elements of the building requires a quantitative knowledge of the wind. In this part we will introduce briefly some notions of macro-meteorology and how the winds are generated, and then focus on their characterization.

2.1 The atmospheric circulation

The atmosphere is a sphere of gas and suspended particles that extends from the earth's surface for tens of kilometres. The 99.99997 % of the atmosphere is located below the altitude of 100 km above sea level called "Karman line" that is the arbitrary upper limit of the atmosphere.

The inner layer, the troposphere, ranges from ground up to an altitude of $12km \div 16Km$ and contains over 80 percent of the mass of the atmosphere and almost all of the water vapour, clouds, and precipitation: nearly all weather phenomena occur there. The source of wind is to be found in the complex mechanical and thermo-dynamic phenomena that occur within this layer. All weather phenomena, in general, are caused by heating due to the action of the Sun, although in an indirect way: contrary to what one might think, in fact, the caloric radiation that weigh more on them are not the ones coming from the star but those emitted from the Earth's surface and atmosphere as a result of their heating by the first.

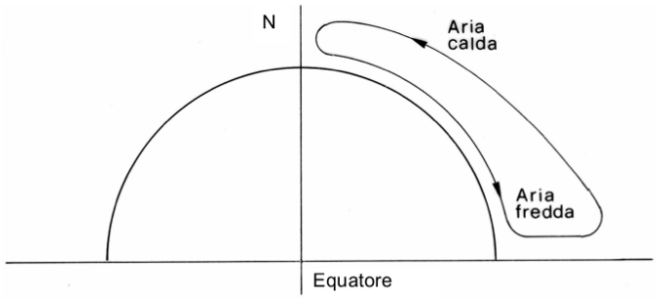

Figure 2.1: Single-cell model

The amount of energy emitted depends, however, by the inclination of the solar rays on the horizon; is clear, therefore, that it is strongly influenced by latitude. In particular, in the equatorial areas the temperature is higher than the terrestrial average while in the polar zones it is lower; it follows that in the first a regime of low pressure is established, while a high pressure one is established in the latter. If there were no other factors, this situation would generate an airflow that could be schematised by a single cell that extend from the Equator to the Pole.(figure 2.1).

Because of the uneven distribution of land and oceans the real phenomenon is actually much more complex and is characterized by the presence of three cells between equator and pole: the Hadley cell, the Ferrel cell and the Polar cell 2.2. These cells have an alternating direction of rotation: the first and the last generating winds from the pole to the equator, while the Ferrel cell generates winds directed from the equator to the pole. We will not go further into detail in this thesis and more details can be found in the specialized literature.

The secondary circulation is the collection of motions that are generated in response to localized increases and decreases in temperature and pressure that are called cyclones and anti-cyclones. These phenomena are typically transient with a time scale ranging from one day to few weeks and a spatial scale ranging from 100 to 1000 kilometres. The secondary circulation is the one associated with the local weather.

The motion of the atmosphere can therefore be thought of as the superposition of interdependent flows, characterized by different dimensions and

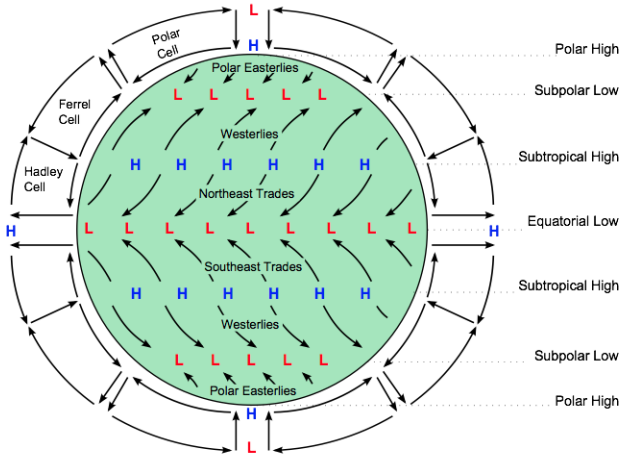

Figure 2.2: Three-cell circulation model

time durations. It can be observed as the duration and size of these phenomena are proportional (Figure 2.3).

It is therefore possible to identify three main categories:

- a *microscale*, which includes the motions having a size not exceeding 20 km and duration lower than one hour;
- a macroscale (or synoptic scale), which includes the motions with size of at least 500 km and a minimum duration of two days;
- a *mesoscale* (or convective scale), which includes the motions of convective cells in a planetary scale.

An effective representation of the various phenomena involved in the atmospheric circulation is provided by the Van der Hoven's spectrum. This is the power spectrum $S_V(n)$ of the wind speed as a function of frequency n, evaluated over a long period of time.

Looking at the spectrum of Van der Hoven (figure 2.4), considered valid for any site and throughout the development of the boundary layer height, you can see two distinct harmonic contributions. The first, located in the area of low frequencies, is the one corresponding to the macro meteorological phenomena and has two peaks: one at the daily periodicity (i.e. breezes) and

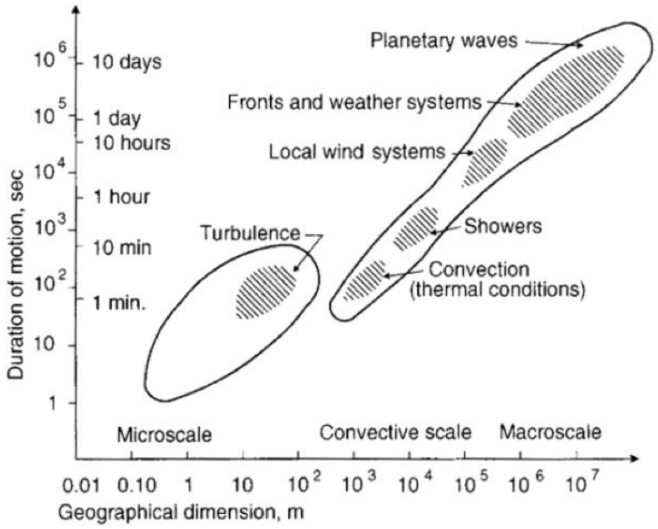

Figure 2.3: Comparison between the time-scale and the length-scale of atmospheric phenomena

the other relating to the storms, the development of which is about four days (there's also a third peak, even more to the left, corresponding to the annual periodicity). The second, localized in the area of high frequencies is due to phenomena of the duration of 1 - 2 minutes, i.e. to atmospheric turbulence.

In the central area, for periods between ten minutes and one hour, the spectrum has virtually no harmonic content. This band is called the *spectral gap* and provides useful information for the reference speed of the wind at a given site.

From the above arises the subdivision of the wind speed in two contributions: the first that expresses the average speed over an interval of 10 minutes and is characterized by long-term variations, and the second representing the fluctuating component of the velocity (turbulence) and is characterized by fluctuations at high frequency with zero mean. Therefore set a Cartesian orthogonal reference system (x, y, z) the wind speed at a point can be written as:

$$\mathbf{V}(t) = u(t)\mathbf{i} + v(t)\mathbf{j} + w(t)\mathbf{k} \tag{2.1}$$

where $\mathbf{i}$, $\mathbf{j}$, $\mathbf{k}$ are versors of the three Cartesian axes. Separating the com-

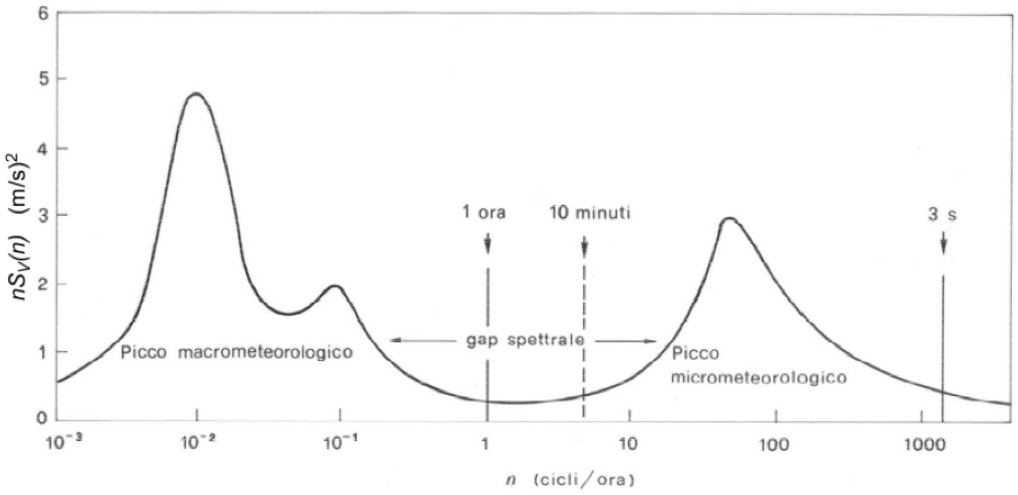

Figure 2.4: Van der Hoven's spectrum of horizontal wind speed

ponents averaged over 10 minutes from the fluctuating components can be written:

$$\begin{aligned} u(t) &= U + u'(t) \\ v(t) &= V + v'(t) \\ w(t) &= W + w'(t) \end{aligned} \tag{2.2}$$

In addition, typically the axis x is assumed coincident with the direction of the mean wind speed. By making this assumption, the average components V and W are cancelled and one can write:

$$\begin{aligned} u(t) &= U + u'(t) \\ v(t) &= v'(t) \\ w(t) &= w'(t) \end{aligned} \tag{2.3}$$

2.2 The atmospheric boundary layer

As the wind approaches the Earth's surface, frictional forces caused by the terrain become more important. Friction slows down the wind and makes it a turbulent flow that varies in a random way both in space and time.The height z_g where the surface friction effects are zero is called *gradient height*

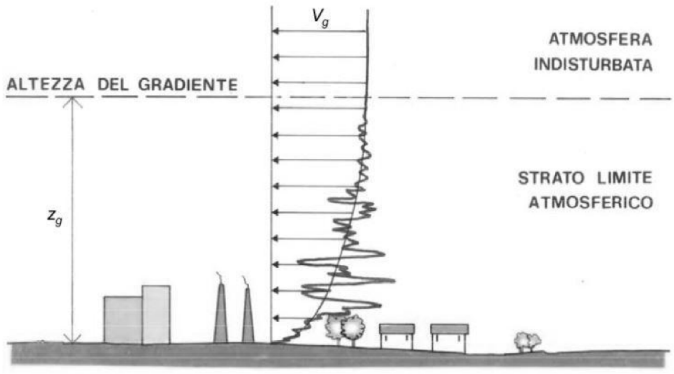

Figure 2.5: The Atmosferic Boundary Layer

2.5. The lowest part of the atmosphere, below the gradient height, is named *Atmospheric Boundary Layer* (ABL) and typically extends up to $500-1000m$ while the rest of the air in the troposphere is called *free atmosphere.*The near earth characteristics are not typical of what we observe in the rest of the atmosphere because of the dominating influence of the ground on the lowest layers of the air. This region is extremely important for civil engineering studies since almost every of the structure is immersed in the ABL.

2.3 Wind characteristics

In order to study and, as in this thesis, reproduce the Atmosphere Boundary Layer is important to characterize it through *quantitative* magnitudes.

The knowledge of wind characteristics in the atmospheric boundary layer that we have nowadays is due mainly to the analysis of large databases of anemometric records performed in different locations of the world for many years. Long-term weather stations are present in the airports, in the air force locations and many interesting points distributed on the ground. By convention, the weather stations are located at 10m above the ground, but there are also measurements taken throughout the development of a vertical from the ground, usually thanks to a weather balloon. Thank to case studies ranging from islands to mountainous areas it has been possible to characterize the ABL and identify the main parameters.

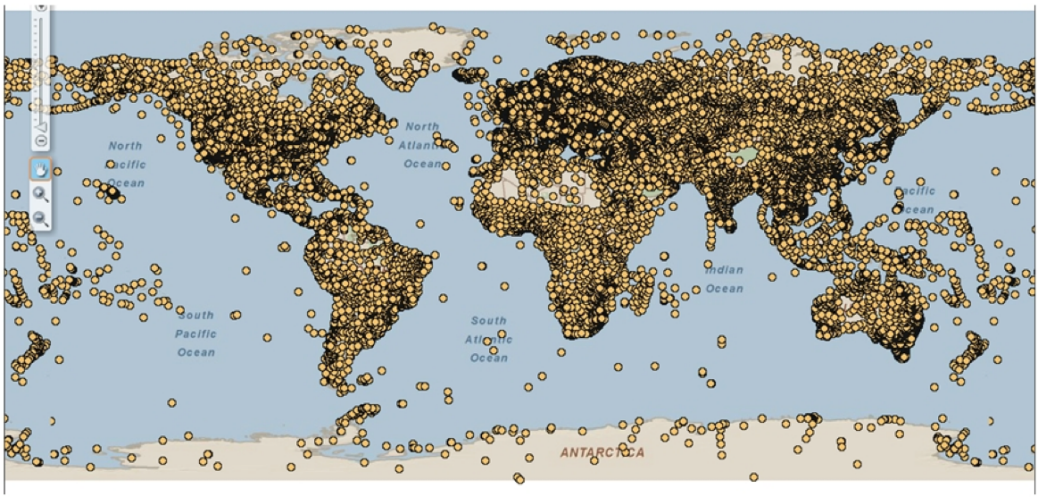

Figure 2.6: Locations of weather stations all over the world (source: NOAA National Climatic Data Center www.ncdc.noaa.gov)

Looking at the wind data at different heights some preliminary observations about the atmospheric boundary layer can be made:

- the average wind velocity increases with the height from ground;
- the amplitude of the fluctuations around the mean decreases with increasing altitude;
- there is a similarity in the pattern of gusts across the entire height; this is indicative of a spatial correlation of turbulence.

Due to the stochastic nature of the wind, it is evident how the variables that characterize it are statistical. The wind, however, is not a completely random phenomenon, but it shows spatial and temporal correlation of different scales. The following section tries to identify the main parameters that characterize it.

Nevertheless, the definition of how many and which are the parameters to fully characterize the ABL is an unresolved issue that manifests itself in the numeric context in the generation of a synthetic stable ABL.

2.3.1 Taylor hypothesis

As mentioned earlier, the wind presents coherent spatial structures typical of turbulent flows. These structures are called *eddies* and are the main contributors to the random nature of turbulent flows (this topic will be discussed in detail in chapter 3.2). Since these structures evolve simultaneously in space and time, to grasp correctly the turbulence we should be able to simultaneously measure the time-history in more points more or less close together in order to recreate a "photograph" of the space distribution of velocity for any given instant of time. This involves considerable technical difficulties. Since the presence itself of the measurement instrumentation alters the flow, during the experiments the measurements are usually performed in a single point at a time.

To reconstruct the spatial coherence of the turbulent structures *Taylor's hypothesis* is used. This is to assume that the vortices are *frozen* in time and that they are dragged along by the average speed of the flow 2.7. Analytically, this corresponds to say:

$$\mathbf{u}(\mathbf{x_p}, t + \Delta t) = u(\mathbf{x_p} - U\Delta t, t) \tag{2.4}$$

With this assumption one can think to know the turbulence along a whole stream line (assumed straight and parallel to the mean velocity) by measuring the velocity at a single point.

This hypothesis turns out to be a good approximation of natural wind in open field.

2.3.2 Mean velocity

Following up what has been previously said in section 2.1 , using the spectral gap is possible to distinguish between a high-frequency (turbulence) contributions and a low frequency (daily or seasonal variations) ones.

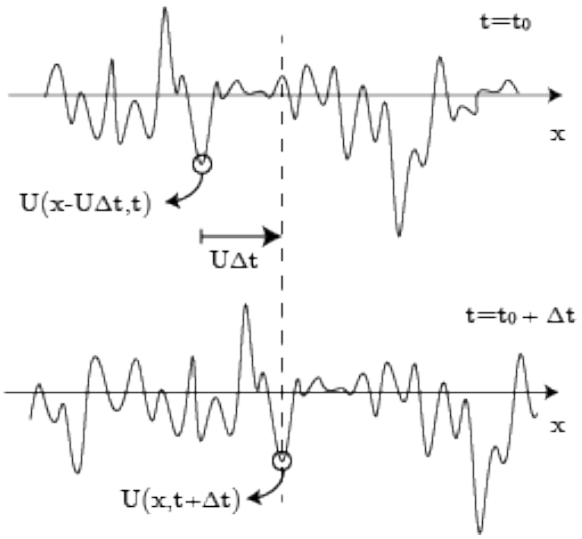

Figure 2.7: Taylor hypothesis

The average wind speed can then be assumed to be equal to:

$$U(z) = \frac{1}{T}\int_{t}^{t+T} u(z,t)\ \mathrm{d}t \qquad \text{where } T = 10min...1hour$$
$$u(z,t) = U(z) + u'(z,t) \tag{2.5}$$

The expression just written is mathematically wrong, because the left-hand side should still be dependent on the time t. However, considering a typical structural engineering problem, such member may be considered constant when studying phenomena whose duration is less than the time T of the moving average operator width . One can then think of the component $U(z)$ as the one responsible for the quasi-static effects on the structure and the component $u'(z,t)$ as the one responsible for the dynamic effects

National codes provide different alternatives for the equation of $U(z)$. These are generally characterized by the parameter z_0 called *aerodynamic roughness length*. This parameter can be interpreted as the height at which the average wind speed is equal to zero. The larger this parameter, the greater the slowing down of the flow near the ground. z_0 is influenced by the geometric dimensions of the obstacles and their density; typical values of z_0 vary from $10^{-5} - 10^{-4}m$, respectively for ice and calm seas, to $1m$ for forests

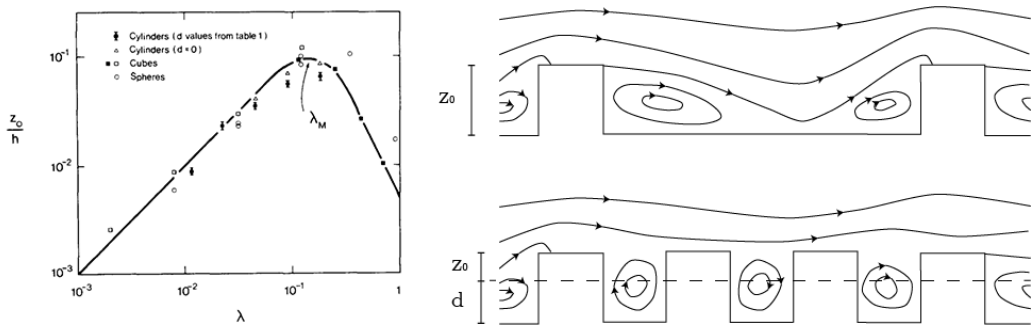

Figure 2.8: On the left, the dependency of z_0 from the non-dimensional roughness density. On the right, conceptual streamlines below the critical density and above the critical density - note the zero displacement plane in the latter case

and towns. National codes assign a value of z_0 depending on the context of the construction.

It is important to notice that could happen to have different values of z_0 depending on the direction of the wind. This is the typical case of coastal buildings for which you have a small z_0 for the wind coming from the sea, while you may have a very large z_0 for the wind coming from the inland.

Is interesting to mention the study by Raupach et al. (1980) in wind tunnel with regular shaped obstacles. This study shows that above a critical density the value of z_0 decrease as the density increase (figure 2.8.a). This result, seemingly counter-intuitive, can be understood thinking that if the obstacles are too close to each other, streamlines are unable to creep between them and they "behave" as the obstacles were lower than they are. In other words it is as above the critical density the plane $z = 0$ is displaced upward by a value d called *zero displacement plane*.

The logarithmic profile

Plotting the $U(z)$ profile acquired experimentally on a semi-logarithmic plane (figure 2.9) is straightforward to see that the lowest part of this profile (up to 100-200 meters) is well represented by a logarithmic law.

Using the Buckingham pi theorem we can assume that there are only two dimensionless groups relevant to the description of the velocity profile. These

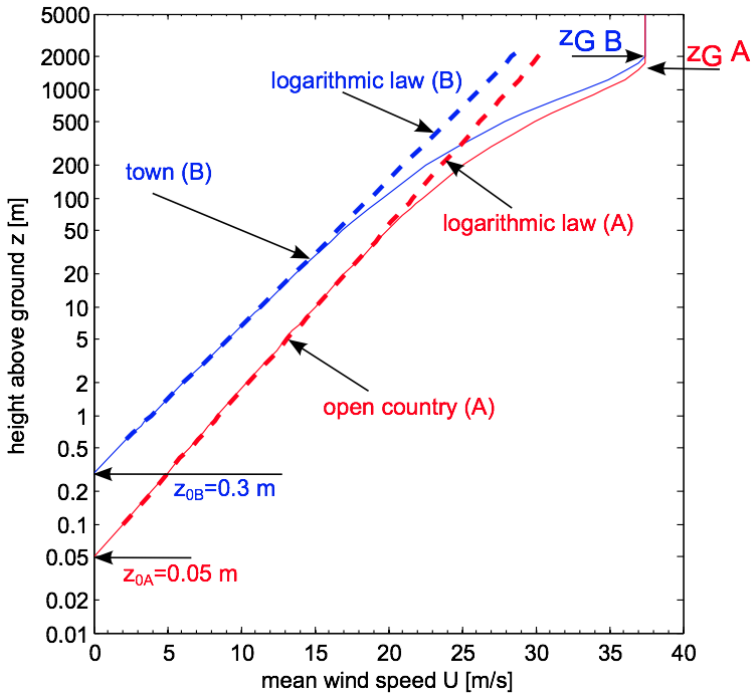

Figure 2.9: Mean velocity profile (double logarithmic scale)

can be obtained by considering four quantities:

- the wind mean speed U
- the height from the ground z
- the *frictional velocity* defined as $u_* = \sqrt{\tau_0/\rho}$ (where τ_0 is the surface stress and ρ is the air density
- and the roughness length z_0)

These can be combined in two dimensionless groups:

$$\pi_1 = \frac{U}{u_*} \qquad \pi_2 = \frac{z}{z_0} \tag{2.6}$$

Based on data plotted in Figure 2.9 we might expect a logarithmic relationship between these two groups:

$$U(z) = \frac{u_*}{k} \ln\left(\frac{z}{z_0}\right) \tag{2.7}$$

where $1/k$ is a constant of proportionality. k is named the von Karman constant and is supposed to be a universal constant that is not a function of the flow nor of the surface. The value of the constant is about $k = 0.4$. The logarithmic relationship has also a physical justification and it is based on the Prandtl flat plate boundary layer theory.

More sophisticated analytical models are available to extends the equations through all the ABL up to the gradient height z_g. The one proposed by Deaves and Harris can be found in Cook (1990).

The power law

Another empirical formulation that is used to describe the wind profile is the *power law*:

$$U(z) = U_{ref} \left(\frac{z}{z_{ref}} \right)^{\alpha} \tag{2.8}$$

Where U_{ref} is the wind velocity at the reference height z_{ref} and α is the power law exponent and is related to the terrain type. Typical values of α ranges from 0.12 to 0.3. The exponent α can be related to the roughness length z_0 by the relationship:

$$\alpha = \left(\ln(z_{ref}/z_0) \right)^{-1} \tag{2.9}$$

The advantage of this formulation is that it does not require the calculation of u^* which can be not immediate. It is also very easy to apply in those cases where one has a time history recorded at an arbitrary height (usually 10m) and knows the type of terrain.

The Eurocode profile

Eurocode 1 (Part 1-4) contains a formulation based on the logarithmic law to describe the velocity profile:

$$\begin{cases} U(z) = U_{ref} k_r \ln\left(\frac{z}{z_0}\right) & z_{min} < z < 200m \\ U(z) = U(z_{min}) & z < z_{min} \end{cases} \tag{2.10}$$

Table 4.1 — Terrain categories and terrain parameters

Terrain category		z_0 m	z_{min} m
0	Sea or coastal area exposed to the open sea	0,003	1
I	Lakes or flat and horizontal area with negligible vegetation and without obstacles	0,01	1
II	Area with low vegetation such as grass and isolated obstacles (trees, buildings) with separations of at least 20 obstacle heights	0,05	2
III	Area with regular cover of vegetation or buildings or with isolated obstacles with separations of maximum 20 obstacle heights (such as villages, suburban terrain, permanent forest)	0,3	5
IV	Area in which at least 15 % of the surface is covered with buildings and their average height exceeds 15 m	1,0	10
NOTE: The terrain categories are illustrated in A.1.			

Figure 2.10: z_0 values proposed by Eurocodice part 1-4

where a reference wind velocity U_{ref} (also named basic wind velocity) and a terrain factor k_r are introduced. The reference wind velocity depends on the wind climate and is evaluated at $10m$ above the ground of terrain category II, for a given return period. The terrain factor is related to the roughness length by the expression:

$$k_r = 0.19\,(20z_0)^{0.07} \tag{2.11}$$

Below the minimum height $z_m in$ the wind velocity is assumed constant.

The value of z_0 and z_{min} recommended by the Eurocode can be seen in Figure 2.10.

2.3.3 Turbulence intensity

The second more important parameter in a random process is the *standard deviation*. To characterize it, it is useful to define a non-dimensional parameter called *turbulence intensity*. For the streamwise component it is defined as:

$$I_u = \frac{\sigma_u(z)}{U(z)} \tag{2.12}$$

where $\sigma_u(z)$ is the standard deviation of the turbulence component u and $U(z)$ is the mean wind velocity, both at height z. In homogeneous terrain conditions, the standard deviation of wind velocity slowly decreases with height and is close to zero at the gradient height. In the same way it is possible to define the lateral and vertical turbulence intensities:

$$\begin{aligned} I_v &= \frac{\sigma_v(z)}{U(z)} \\ I_w &= \frac{\sigma_w(z)}{U(z)} \end{aligned} \tag{2.13}$$

It is interesting to notice that the vertical turbulence intensity approaches 0 close to the ground. This is due to the fact that near the ground there isn't the physical space for vertical structures to arise. This is only true for the vertical component, while streamwise and span-wise components don't approaches 0.

For flat terrain and homogeneous roughness the turbulence intensity is approximately given by:

$$I_u = \frac{1}{\ln(z/z_0)} \tag{2.14}$$

where z_0 is the roughness length. The other two profiles can be obtained as a fraction of the streamwise one as:

$$I_v(z) = 0.75 I_u(z) \qquad I_w(z) = 0.5 I_u(z) \tag{2.15}$$

The Eurocode uses this formulation also. It is possible to observe that the turbulence increases as the roughness increases; i.e. bigger obstacles generate more turbulent flows.This formulation doesn't take into account the reduction of the vertical turbulence close to the ground mentioned above.

2.3.4 Integral length scales

As said earlier and as will be seen in more detail in Chapter 3.2, turbulence is not a completely random process as it might appear at a first look: it is composed by *coherent structures*. The presence of these structures makes the

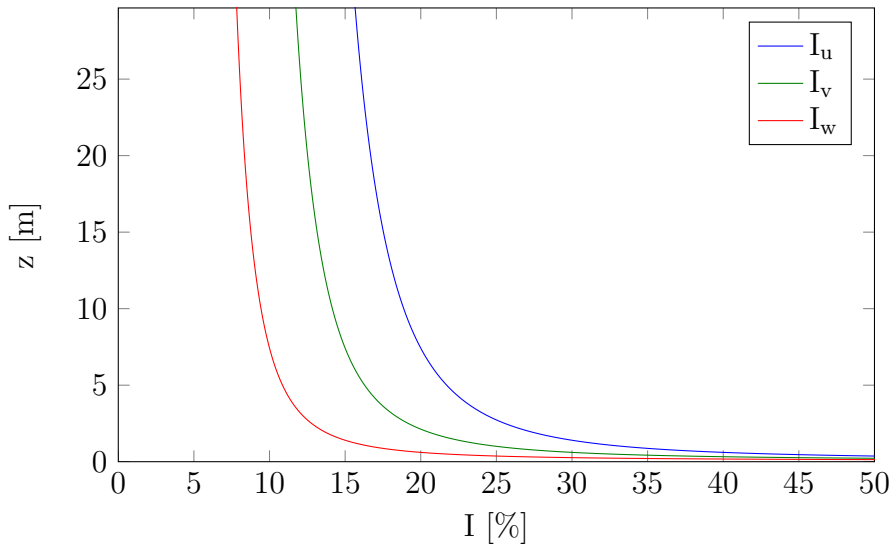

Figure 2.11: Eurocode turbulence intensity profiles

time-history of closely spaced points to be not completely uncorrelated, but to be somehow similar the more they are close to each other.

Average value and standard deviation measured in one point are not able to catch this feature. To do it, it is necessary to introduce a new parameter: the *integral length*. This parameter represents the mean size of the vortex in a give direction. There are 9 integral length scales; they are defined as:

$$L_{u_i}^{x_j} = \int_0^\infty R_{u_i}(x_j)\ \mathrm{d}x_j \qquad \text{with } u_i = u, v, w \text{ and } x_j = x, y, z \tag{2.16}$$

where $R_{u_i}(x_j)$ is the auto-correlation function of u_i measured along the direction x_j with origin in the considered point. The 9 scales are:

$$\begin{matrix} L_u^x & L_u^y & L_u^z \\ L_v^x & L_v^y & L_v^z \\ L_w^x & L_w^y & L_w^z \end{matrix} \tag{2.17}$$

E.g. the integral scale L_v^z represents the correlation of the velocity component

v measured along an axis parallel to z.

From this definition, it follows that to compute the integral scales in one point, one would need to now the three velocity components inside the entire domain *at the same time*. Experimentally this is impossible, since the experimental data is usually *spatially discrete*. To (partially) work around this limitation, it is useful to use the Taylor hypothesis: instead of integrate over space along x (the streamwise direction), it is possible to integrate over time. Since the *temporal resolution* is usually far higher than the spatial one, this allows to have a more precise value of $L^x_{x_j}$. The resulting equation is:

$$L^x_i = \int_0^\infty R_{u_i}(\tau) U \, \mathrm{d}\tau \qquad \text{with } u_i = u, v, w \tag{2.18}$$

This equation can only be used for the integral scale L^x_u, L^x_v e L^x_w since the Taylor hypothesis allow to switch only the streamwise direction with time (structures are not dragged in the y and z direction).

This equation can be used to compute the integral scales in a given point. Measuring the integral scales along a vertical axis one can obtain a profile of the average size of the eddies. Several empirical formulations exists for these profiles. The Eurocode suggests:

$$\begin{aligned} L^x_u(z) &= 300 \left(\frac{z}{200}\right)^\alpha \\ \alpha &= 0.67 + 0.05 \ln(z_0) \end{aligned} \tag{2.19}$$

It has also been proved that the auto-correlation function has an exponential decay:

$$R_u(y) = \exp\left(-y/L^x_u\right) \tag{2.20}$$

The remaining integral scales are usually computed as a fraction of the longitudinal one:

$$\begin{aligned} L^x_v &\approx 0.25 L^x_u \quad L^x_w \approx 0.10 L^x_u \\ L^y_u &\approx 0.30 L^x_u \quad L^z_u \approx 0.20 L^x_u \end{aligned} \tag{2.21}$$

During post-processing the function $R_{u_i}(\tau)$ can happens to be too "noisy". Theoretically this function should approach 0 as τ grows. What really hap-

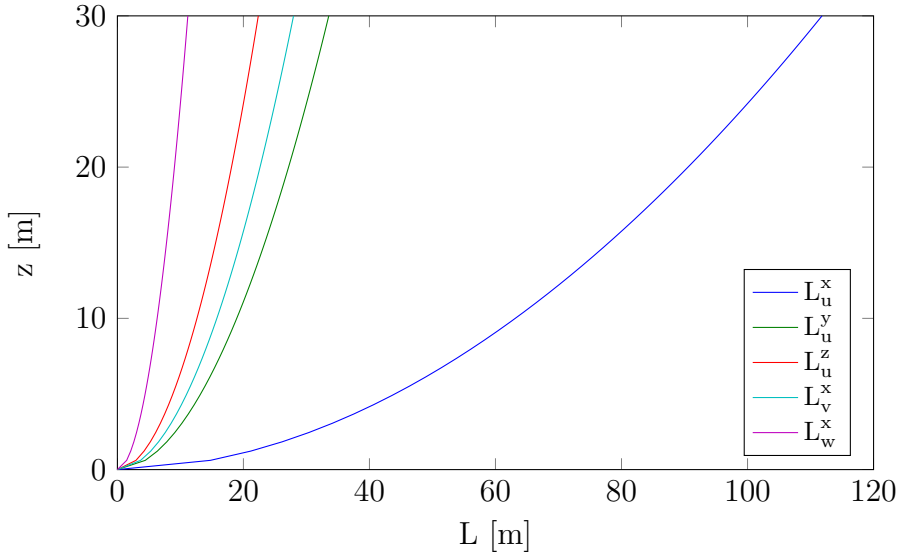

Figure 2.12: Eurocode integral length profiles

pens is that this function keeps oscillating around 0 (figure 2.13). Since the integral cannot be extended up to infinity, the choice of the upper limit can significantly alter the value. To overcome this problem, the solution we decided to use is to interpolate the experimental function with the function 2.20 through a best-fitting operation. Doing this the obtained function can be easily integrated; moreover one can evaluate the integral scale directly looking at the denominator of the exponent of the interpolating function without any further calculation.

2.3.5 Power spectrum

We already discussed the fact that the turbulence can be seen as an overlap of turbulent structures with different size and duration. A good way to visualize this is using the wind velocity power spectrum. A more detailed discussion about the turbulence spectrum will be done in section 3.2.

Many equations have been proposed in literature to describe quantitatively the wind spectrum. They are usually function of the wind mean speed U, the turbulence intensity or the variance σ_u and the integral length scale L_u^x.

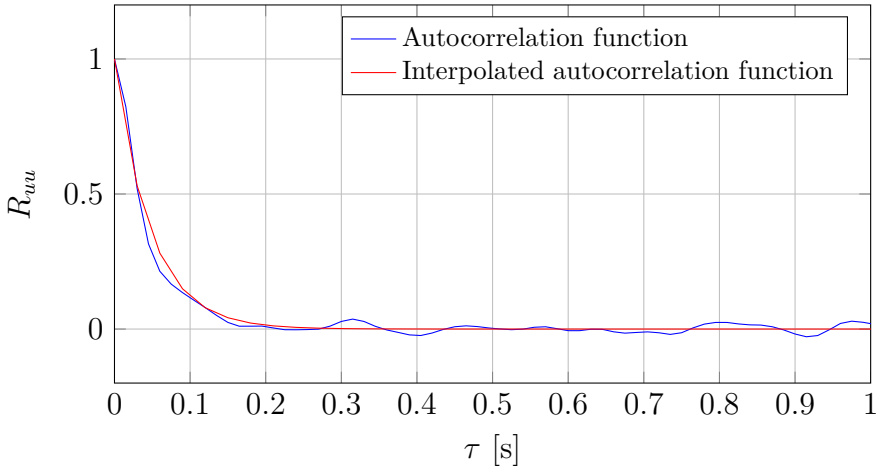

Figure 2.13: Autocorrelation function

Von Karman proposed:

$$\frac{f \cdot S_u(f)}{\sigma_u^2} = \frac{4\left(\frac{fL_u^x}{U}\right)}{\left[1 + 70.8\left(\frac{fL_u^x}{U}\right)^2\right]^{5/6}} \tag{2.22}$$

where the left hand term is the non-dimensional spectral density. At the right hand term appears the non-dimensional frequency:

$$f^* = \frac{fL_u^x}{U} \tag{2.23}$$

A similar expression is proposed in Eurocode 1 Part 1-4:

$$\frac{f \cdot S_u(f)}{\sigma_u^2} = \frac{6.8\left(\frac{fL_u^x}{U}\right)}{\left[1 + 10\left(\frac{fL_u^x}{U}\right)\right]^{5/3}} \tag{2.24}$$

The two different spectra are compared in Figure 2.14. It is to note that in the high frequency range both spectra has an almost linear trend with a fixed slope equal to $-5/3$. This value is absolutely not random, but originates from the theory of turbulence and the "energy cascade" that we will see in section 3.2. Another interesting fact is that for both spectra it's valid

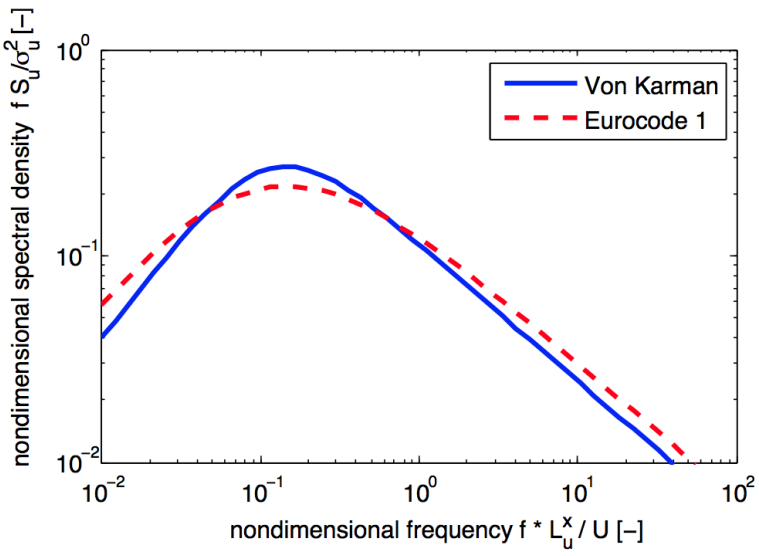

Figure 2.14: Power spectral density for the streamwise component u

$$f^*_{peak} = \frac{1}{2\pi} \tag{2.25}$$

from which can be evaluated:

$$L^x_u = \frac{1}{2\pi}\frac{U}{f_{peak}} \tag{2.26}$$

2.3.6 Conclusions

In this section we presented the main analytical tools that will be used to study the incoming flow for both the CFD simulation and the wind tunnel tests. We saw as the turbulent flow is characterised by several parameters that usually depend by the height above the ground. The plots representing these values over the height are called *profiles* and will be compared to understand if the incoming flow is correctly simulated.

The assumption that the turbulent flow is correctly identified by these parameters alone is a debated topic. This problem will be resumed in section 5.1 where the inflow condition to correctly reproduce the wind tunnel ABL will be studied.

Chapter 3

Computational Fluid Dynamics

Computational Fluid Dynamics (CFD) is the analysis of a system that includes a fluid flow, heat transfers, chemical reactions and other physical phenomena related to them through a simulation with numerical methods. This science has several applications in industry and research, such as the calculation of drag and lift forces of a plane, the fluid-dynamic of the water around a boat, the mixing of the fuel inside a combustion chamber, etcetera.

In the civil engineering field, CFD can be used for the simulation of the interaction of air or water flow with a structure. This it is the case of wind induced instability of a bridge (flutter, buffeting, vortex shedding...), of the interaction of the wave motion with an off-shore platform's pile or, as it is in this thesis, the study of external pressure on the cladding of a building.

The main problem with CFD is the extremely high computational power that is required. Especially in civil engineering applications, what is relevant about the fluid-structure interaction is its *unsteady component*. This lead to the necessity to run time-depending simulation with very large domains. Since an analytical solution is infeasible, the domain is discretised both in time and space. It isn't uncommon for this kind of problems to have millions or even billions variables governed by non-linear partial differential equations that have to be solve millions of times in time domain. It's therefore clear as the number of floating point operations to solve the problem can reach order of magnitude as $10^{20} \div 10^{22}$. Such number of operation with existing

computational resources can take weeks or even months to be executed. Just to give an example: the most powerful super-computer in the world existing at the moment can execute $33.86 \cdot 10^{15}$ floating points operations per second. The main focus of CFD research in the past years has been to find a way to reduce the number of operations needed to solve a problem without reduce (too much) the solution quality. Thanks to this research and the simultaneous increase of the power of super-computers, such applications have seen for about a decade now a gradually increasing interest in industrial applications so that the AIJ, the entity in charge of the drafting of the Japanese regulatory codes for the building, is drafting legislation dedicated to CFD simulations.

In the next chapter we will see a brief introduction to the Navier-Stokes equations and to the main techniques used to solve them. This introduction doesn't pretend to be exhaustive because of the vastness and complexity of the topic. For more information, refer to Anderson (1995) ans Versteeg (2007)

3.1 The governing equations

The governing equations of fluid flow represent mathematical statement of the conservation laws of physics.

- The mass of a fluid is conserved.
- The rate of change of momentum equals the sum of the forces on a fluid particle (Newton's second law $\mathbf{F} = m\mathbf{a}$).
- The rate of change of energy is equal to the sum of the rate of heat addition to and the rate of work done on a fluid particle (first law of thermodynamics $\Delta U = Q - W$).

The fluid will be regarded as a continuum. For the analysis of fluid flows at macroscopic length the molecular structure of matter and molecular motions may be ignored. Starting from the three statements above, one can obtain the Navier-Stokes equation (for a detailed derivation seeAnderson (1995)).

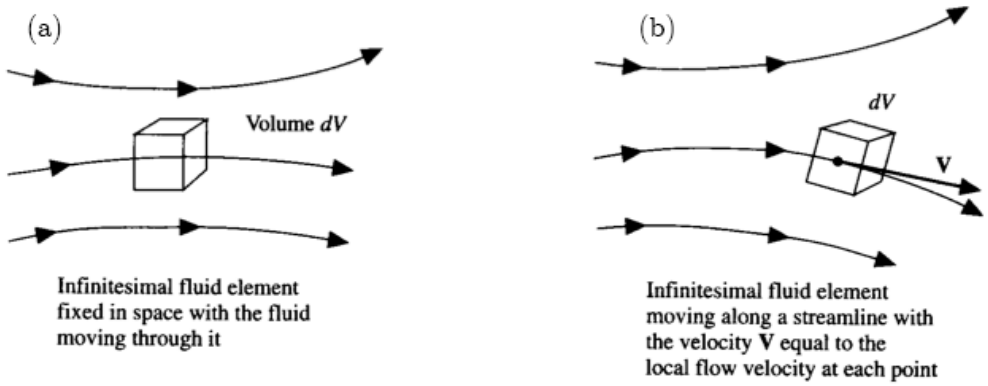

Figure 3.1: Eulerian and Lagrangian reference systems

3.1.1 The reference system and the substantial derivative

Before starting the derivation of the equations, it's important to decide which reference system will be used. There are two options, both valid, that lead to two different forms of the same equations:

- the *Eulerian specification of the flow field* is a way of looking at fluid motion that focuses on specific locations in the space through which the fluid flows as time passes. In other words, the control volume used to write down the equation of motions is still in place and the fluid flows through it (figure 3.1.a).

- the *Lagrangian specification* is a way of looking at fluid motion where the observer follows an individual fluid particle as it moves through space and time. In this case the control volume moves with the flow through the domain and can change both size and shape, however there is no flow through the control volume boundaries (figure 3.1.b).

Since the control volumes in the CFD applications, the *cells*, are still in place[1] the most obvious specification to use is the Eulerian one. However

[1] the cells of the mesh can move in the case of a moving geometry, such as a rotating wind turbine or an opening valve

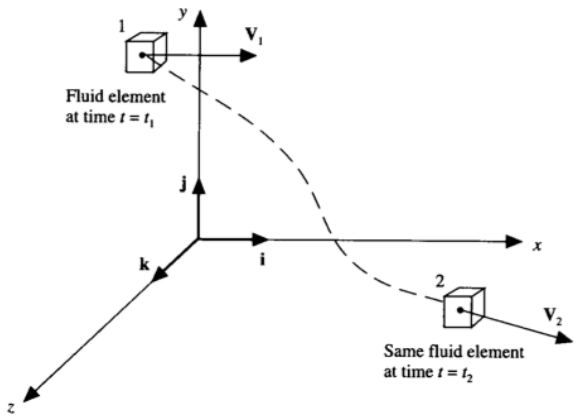

Figure 3.2: Fluid element moving in the fluid flow for the physical interpretation of the substantial derivative

an interesting physical observation can be done considering the relationship between these two reference frames.

Lets consider a fluid element moving with the flow (Lagrangian approach) that at time $t = t_1$ lies at coordinates x_1, y_1, z_1. In addition the scalar quantity field $\varphi(x, y, z)$ is given (e.g. temperature or density).(Figure 3.2).

Now lets consider the same fluid element at time $t = t_2 > t_1$. We can expand the function of φ in Taylor series about point 1, obtaining

$$\varphi_2 = \varphi_1 + \left(\frac{\partial\varphi}{\partial x}\right)_1 (x_2 - x_1) + \left(\frac{\partial\varphi}{\partial y}\right)_1 (y_2 - y_1) + \\ + \left(\frac{\partial\varphi}{\partial z}\right)_1 (z_2 - z_1) + \left(\frac{\partial\varphi}{\partial t}\right)_1 (t_2 - t_1) + \text{higher-order terms} \quad (3.1)$$

where $\varphi_i = \psi(x_i, y_i, z_i)$. Dividing by $t_2 - t_1$ and ignoring higher-order terms, we obtain

$$\frac{\varphi_2 - \varphi_1}{t_2 - t_1} = \left(\frac{\partial\varphi}{\partial x}\right)_1 \frac{x_2 - x_1}{t_2 - t_1} + \left(\frac{\partial\varphi}{\partial y}\right)_1 \frac{y_2 - y_1}{t_2 - t_1} + \left(\frac{\partial\varphi}{\partial z}\right)_1 \frac{z_2 - z_1}{t_2 - t_1} + \left(\frac{\partial\varphi}{\partial t}\right)_1 \quad (3.2)$$

Examine the left side of equation 3.2. This is physically the average time rate of change in the scalar quantity φ of the fluid element. In the limit, as

t_2 approaches t_1, this term becomes

$$\lim_{t_2 \to t_1} \frac{\varphi_2 - \varphi_1}{t_2 - t_1} = \frac{D\varphi}{Dt} \tag{3.3}$$

Here, $D\varphi/Dt$ is a symbol for the instantaneous time rate of change of quantity φ of the fluid element as it moves through point 1. By definition this symbol is called the *substantial derivative* D/Dt. Here, our eyes are locked on the fluid element as it is moving, and we are watching the quantity φ of the element change as it moves through point 1. This is different from $(\partial\varphi/\partial t)_1$ which is physically the time rate of change of density at the fixed point 1. Thus $D\varphi/Dt$ and $\partial\varphi/\partial t$ are physically and numerically different quantities.

Returning to equation 3.2 , we can replace

$$\lim_{t_2 \to t_1} \frac{x_2 - x_1}{t_2 - t_1} \equiv u$$

where u is the velocity component directed along x. Doing this with the other two components and remembering

$$\text{div} \equiv \mathbf{i}\frac{\partial}{\partial x} + \mathbf{j}\frac{\partial}{\partial y} + \mathbf{k}\frac{\partial}{\partial z}$$

equation 3.2 can be written as

$$\frac{D\varphi}{Dt} = \frac{\partial\varphi}{\partial t} + \mathbf{u}\,\text{div}\,\rho \tag{3.4}$$

Focusing on this equation we can see how the substantial derivative operator D/Dt, which is physically the time rate of change following a moving fluid element (Lagrangian approach), is equal to the time rate of change at a fixed point $\partial/partialt$, which is called *local derivative* (Eulerian approach) plus a *convective term* $\mathbf{U}\,\text{div}$ which is physically the time rate of change due to the movement of fluid element from one location to another where the flow properties are spatially different.

This derivation shows the meaning of the convective term that will be present in almost every Navier-Stokes equation.

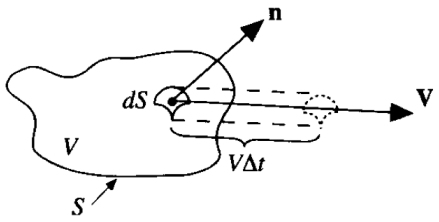

Figure 3.3: Control volume used for the physical interpretation of the divergence of velocity

3.1.2 The divergence of the velocity

In the last section we examined the physical meaning of the substantial derivative and the convective term. Now lets try to understand the physical meaning of the divergence of the velocity div $\mathbf{u}$.

Consider a finite control volume moving with the fluid (Lagrangian approach) as sketched in figure 3.3. This volume is always made of the same fluid particles as it moves with the flow; hence, its mass is fixed, invariant with time. However, its volume V and control surface S are changing with time as it moves to different regions of the flow where different values of density ρ exist. Consider an infinitesimal element of the surface dS moving at the local velocity $\mathbf{u}$, as shown in figure 3.3. The change in the volume of the control volume ΔV, due to just the movement of dS over a time increment Δt is, from figure 3.3, equal to the volume of the long, thin cylinder with base area dS and length $(\mathbf{u}\Delta t)\cdot\mathbf{n}$, where n is a unit vector perpendicular to the surface at dS. That is:

$$\Delta V = [(\mathbf{u}\Delta t)\cdot\mathbf{n}]\, dS = (\mathbf{u}\Delta t)\cdot\mathbf{dS} \tag{3.5}$$

where the vector dS is defined simply as $dS \equiv \mathbf{n}dS$. Over the time increment Δt, the total change in volume of the whole control volume is equal to the summation of ΔV over the total control surface. In the limit as $dS \to 0$, the sum becomes the surface integral

$$\Delta V = \iint_S (\mathbf{u}\Delta t)\cdot\mathbf{dS} \tag{3.6}$$

If this integral is divided by Δt, the result is physically the time rate of change of the control volume, denoted by DV/Dt; that is,

$$\frac{DV}{Dt} = \lim_{\Delta t \to 0} \frac{1}{\Delta t} \iint_S (\mathbf{u}\Delta t) \cdot \mathbf{dS} = \iint_S \mathbf{u} \cdot \mathbf{dS} \tag{3.7}$$

Note that at the left side there is the substantial derivative of the volume V. This is because we are dealing with the time rate of change of the control volume *as the volume moves with the flow* and this is physically what is meant by the substantial derivative. Now we can apply the divergence theorem from the vector calculus to the right side of equation 3.7; we obtain

$$\frac{DV}{Dt} = \iiint_V \operatorname{div} \mathbf{u} dV \tag{3.8}$$

We can now switch from the control volume V to the infinitesimal volume dV. We can then assume that $\operatorname{div} \mathbf{u}$ is constant throughout dV. Therefore

$$\frac{D(dV)}{Dt} = \iiint_{dV} \operatorname{div} \mathbf{u} dV = (\operatorname{div} \mathbf{u}) dV \tag{3.9}$$

or

$$\operatorname{div} \mathbf{u} = \frac{1}{dV} \frac{D(dV)}{Dt} \tag{3.10}$$

From this equation we can understand the physical meaning of the divergence of the velocity.

$\operatorname{div} \mathbf{u}$ *is physically the time rate of change of the volume of a moving fluid element per unit volume*

3.1.3 The continuity equation

The first equation to be presented is the continuity equation that represents the conservation of the mass in the flow. How this equation is derived can be seen in Anderson (1995). We will propose its Lagrangian form and discuss its physical meaning.

The continuity equation in the Lagrangian form is:

$$\frac{D\rho}{Dt} + \rho \operatorname{div}(\mathbf{u}) = 0 \tag{3.11}$$

here ρ is the fluid density and $\mathbf{u}$ the velocity vector.

In this equation appear both the substantial derivative and the divergence of the velocity we've seen above. The first term of equation 3.11 is the substantial derivative of the density. As we've seen before in section 3.1.1, this represent the rate of change in the density inside the infinitesimal element moving with the fluid, hence we don't care if this happens because the element moved to a different location or because something evolved in time. The second term contains the divergence of the velocity. As said in section 3.1.2, this is physically the percentage increase of the local volume of the element; multiplied by the density this is the increase of density due to volumetric dilatation. This equation is therefore saying us that if the density is increasing inside an element over time, the volume must decrease and vice-versa.

We decided to use the Lagrangian version of the equation because it's easier to understand the physical meaning. Now with very little manipulation we can obtain the Eulerian form that is:

$$\frac{\partial\rho}{\partial t} + \operatorname{div}(\rho\mathbf{u}) \tag{3.12}$$

In subsonic aerodynamic the air is usually considered as an incompressible fluid. This lead to the equation:

$$\operatorname{div}\mathbf{u} = 0 \tag{3.13}$$

3.1.4 The momentum equation

The second equation to be presented is the one that represent the conservation of the momentum i.e. the Newton's second law. $\mathbf{F} = m\mathbf{a}$.

The complete derivation is long and tedious. Again we present just the Lagrangian form and we comment it. Since the momentum is a vector quan-

tity there are three scalar equations, one for each component. The equation for the u component is:

$$\frac{D(\rho u)}{Dt} = -\frac{\partial p}{\partial x} + \frac{\partial \tau_{xx}}{\partial x} + \frac{\partial \tau_{yx}}{\partial y} + \frac{\partial \tau_{zx}}{\partial z} + \rho f_x \tag{3.14}$$

In this equation some new unknowns appear. The left side of equation 3.14 is the change of x component of momentum in time. On the right side there is the net force along x. We can recognise: the contribution of pressure p, the contribution of viscous stresses τ_{ij} and volumetric force f_x defined as the force per unit of mass directed along x.

The viscous forces can be related to the speed with an equation that depends on the nature of the fluid. For Newtonian fluids can be assumed:

$$\tau_{ij} = \delta_{ij} - \frac{2}{3}(\operatorname{div} \mathbf{u}) + \mu \left(\frac{\partial u_i}{\partial x_j} + \frac{\partial u_j}{\partial x_i} \right) \tag{3.15}$$

where δ_{ij} is the kronecker delta that's equal to 1 for $i = j$ and 0 for $i \neq j$.

Considering the case $\rho = \text{const.}$ and switching to the Eulerian approach we obtain:

$$\frac{\partial u}{\partial t} = -\frac{1}{\rho}\frac{\partial p}{\partial x} + \frac{1}{\rho}\left[\frac{\partial \tau_{xx}}{\partial x} + \frac{\partial \tau_{yx}}{\partial y} + \frac{\partial \tau_{zx}}{\partial z} \right] + f_x \tag{3.16}$$

3.1.5 Final remarks about the governing equations

Lets look at the four equations that we just derived. The first equation is the continuity equation where only density and velocity appear. The subsequent three are the momentum equation for the three velocity component. They are strongly non linear because of the convective term and in each equation all the variables p, u, v, w and ρ appears.

In the case where ρ is a constant, such as the incompressible case, these equation are a set of four equations with four unknowns. Therefore this can be solved without any other equation. As we said before a fifth Navier-Stokes equation exists that represent the conservation of energy. This is however needed only in the case of a compressible flow where the density depends on the pressure and other energy variables such as the internal energy e or the

Figure 3.4: Sketch from Leonardo da Vinci's notebooks. Atlantic Code

temperature T. Since in this thesis this equation won't be used, we won't present it here. It can be however found in Anderson (1995).

This set of equations are the basis of any fluid-dynamic problem, hence also the CFD ones. As we have just said, these equations are strongly non-linear. To solve them numerically, it is therefore needed to choose a correct solving procedure. This problem will be analysed in section 5.2.

3.2 The turbulence

All flows encountered in engineering practice, from simple ones, such as two- dimensional jets, wakes, pipe flows and flat plate boundary layers, to more complicated three-dimensional ones, become unsteady above a certain Reynolds number. At low Reynolds numbers flows are laminar. At higher Reynolds numbers flows are observed to become turbulent. A chaotic and random state of motion develops in which the velocity and pressure change continuously with time within substantial regions of flow.

Fluid engineers need access to viable tools capable of representing the effects of turbulence. This chapter gives a brief introduction to the physics of turbulence.

As said earlier turbulence is a random state of motion. However it is not completely chaotic: turbulent flows are highly organized in spatial coherent

structures called *eddies*. These structures presents a wide range of time and length scales, which vary from the same size of the problem up to the order of micrometres. The turbulence is characterised by a strong mixing: particles of fluid which are initially separated by a long distance can be brought close together by the eddying motions in turbulent flows.

The largest turbulent eddies interact with and extract energy from the mean flow by a process called *vortex stretching*. The presence of mean velocity gradients in sheared flows distorts the rotational turbulent eddies. Suitably aligned eddies are stretched because one end is forced to move faster than the other.

The characteristic velocity θ and characteristic length l of the larger eddies are of the same order as the velocity scale U and length scale L of the mean flow. Hence a "large eddy" Reynolds number $Re_l = \theta l/\nu$ formed by combining these eddy scales with the kinematic viscosity will be large in all turbulent flows, since it is not very different in magnitude from UL/ν, which itself is large. This suggests that these large eddies are dominated by inertia effects and viscous effects are negligible.

Smaller eddies are themselves stretched strongly by somewhat larger eddies and more weakly with the mean flow. In this way the kinetic energy is transferred down from large eddies to progressively smaller and smaller eddies in what is called the *energy cascade*. This is shown in figure 3.5, which represents the turbulent energy spectrum. On the x-axis the wavenumber $\kappa = 2\pi/\lambda = 2\pi f/u$, where λ is the wavelength of the eddies and f is the frequency and on the y-axis the spectral energy $E(\kappa)$.

The diagram shows that the energy content peaks at the low wavenumbers, so the larger eddies are the most energetic. They acquire their energy through strong interactions with the mean flow. The value of $E(\kappa)$ rapidly decreases as the wavenumber increases, so the smallest eddies have the lowest energy content.

The smallest scales of motion in a turbulent flow (lengths of the order of 0.1 to 0.01 mm and frequencies around 10 kHz in typical turbulent engineering flows) are dominated by viscous effects. The Reynolds number Re_η of the smallest eddies based on their characteristic velocity υ and characteristic

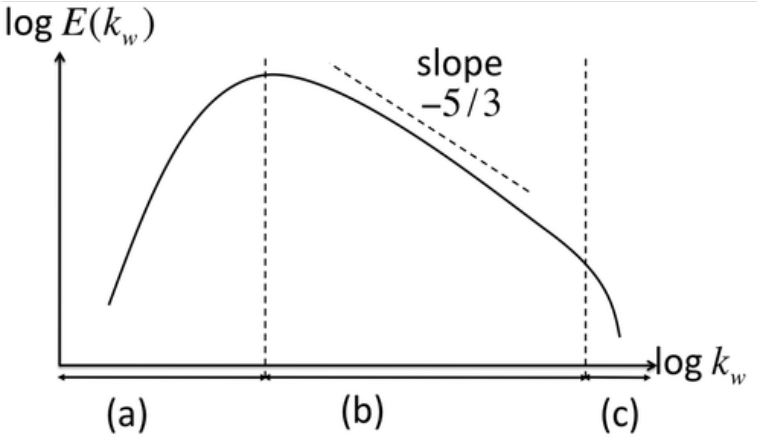

Figure 3.5: Turbulence power density spectrum

length η is equal to 1, $Re_\eta = v\eta/\nu = 1$, so the smallest scales present in a turbulent flow are those for which the inertia and viscous effects are of equal strength. These scales are named the Kolmogorov microscales after the Russian scientist who carried out ground-breaking work on the structure of turbulence in the 1940s. At these scales work is performed against the action of viscous stresses, so that the energy associated with small-scale eddy motions is dissipated and converted into thermal internal energy. This dissipation results in increased energy losses associated with turbulent flows.

The Kolmogorov length, time and velocity scales can be estimated through the equations derived by Kolmogorov himself using the dimensional analysis that are:

$$\begin{array}{ll} \text{Length scale} & \eta \approx Re_l^{-3/4}\, l \\ \text{Time scale} & \tau \approx Re_l^{-1/2}\, T \\ \text{Velocity scale} & v \approx Re_l^{-1/4}\, \theta \end{array} \tag{3.17}$$

Typical values of Re_l might be $10^3 \div 10^6$, so the length, time and velocity scales associated with small dissipating eddies are much smaller than those of large, energetic eddies, and the difference (the so-called *scale separation*) increases as Re_l increases.

Kolmogorov made the following three assumptions:

1. **Hypothesis of local isotropy**: At sufficiently high Re, the small-scale eddies ($l << L$) are statistically isotropic.

As energy is transferred to smaller and smaller scales, memory of the boundary conditions (which are responsible for the anisotropy) is eventually lost. For some $l << L$, then the eddies become isotropic.

2. **First similarity hypothesis**: In every turbulent flow at sufficient high Re, the statistic of the smallest scales of motion are uniquely determined by the kinematic viscosity ν and the dissipation rate ε.

   At the smallest scales, dissipation takes place. Thus both the viscosity and the dissipation rate must be important parameters, and the time, length and velocity scale can be built from them. These are known as the *Kolmogorov scales*.

3. **Second similarity hypothesis**: In every turbulent flow at sufficiently high Re, there is a range of scales $L >> l >> \eta$ in which the statistics have a universal form determined only by ε.

   This is the range in which the eddies only transfer energy from larger to smaller scales (which is the reason why the dissipation rate ε must be an important parameter). In this region, the *inertial range*, dimensional analysis allows us to derive an analytical form for the spectrum $E(\kappa)$:

$$E(\kappa) = C_K \varepsilon^{2/3} \kappa^{-5/3} \tag{3.18}$$

   where C_k is a universal constant, the *Kolmogorov constant*. Experimental and numerical data confirms the existence of the power-law spectrum postulated by Kolmogorov in a wide variety of flows. From this equation can be seen how the tangent of the power spectrum (in logarithmic scale) has always slope equal to $-5/3$.

3.3 The simulation of turbulence

As seen in the previous section, turbulent flows are characterised by a wide spectrum of temporal and length scales. Moreover the energy dissipation takes place at the so-called Kolmogorov scales, which are several orders of

magnitude smaller than the geometry of the problem. The contribution of these scales to the velocity, pressure and temperature variations of the problem is negligible because of their low energy content. However it's not possible to completely ignore them since their presence is fundamental for the correct computation of the dissipated energy. Since the computational cost required to directly simulate this scale is huge and their information content small, it is no surprise that a substantial amount of research effort is dedicated to the development of numerical methods to capture the important effects due to turbulence without directly simulate it. The methods can be grouped into the following three categories:

- **Reynolds-averaged Navier-Stokes (RANS) equations**: attention is focused on the mean flow and the effects of turbulence on mean flow properties. Prior to the application of numerical methods the Navier-Stokes equations are time averaged (or ensemble averaged in flows with time-dependent boundary conditions). Extra terms appear in the time-averaged (or Reynolds- averaged) flow equations due to the interactions between various turbulent fluctuations. These extra terms are modelled with several techniques that try to link them to know variable. Among them the best known ones are the $k-\varepsilon$ model, $k-\omega$ and he Reynolds stress model. The computing resources required for reasonably accurate flow computations are modest, so this approach has been the mainstay of engineering flow calculations over the last three decades.

  These methods however have the drawback that the solution is strongly dependent by the correct turbulence model used. Moreover there are several "tuning" constants that have to be benchmarked and validated for each kind of problem.

  In open field - and therefore in wind engineering - applications these technique showed disappointing results with errors in the order of 15-20%.

  Furthermore RANS models cannot be used to correctly evaluate peak values, since they only compute mean flow quantities.

- **Large eddy simulation**: this is an intermediate form of turbulence calculations which tracks the behaviour of the larger eddies. The method involves space filtering of the unsteady Navier-Stokes equations prior to the computations, which passes the larger eddies and rejects the smaller eddies. The effects on the resolved flow (mean flow plus large eddies) due to the smallest, unresolved eddies are included by means of a so-called sub-grid scale model. Unsteady flow equations must be solved, so the demands on computing resources in terms of storage and volume of calculations are large. However due to the increasing computational resources available and the several benefits that it has, this technique is starting to be applied to industrial applications.

- **Direct numerical simulation (DNS)**: these simulations compute the mean flow and all turbulent velocity fluctuations. The unsteady Navier-Stokes equations are solved on spatial grids that are sufficiently fine that they can resolve the Kolmogorov length scales at which energy dissipation takes place and with time steps sufficiently small to resolve the period of the fastest fluctuations. These calculations are highly costly in terms of computing resources, so the method is not used for industrial flow computations and even in research field only simple geometry has been simulated. An industrial application of this technique in the next decade is unlikely.

3.3.1 The large eddy simulation technique

In this thesis the LES technique has been chosen to simulate the problem. In this chapter will be presented the main "philosophy" behind the LES approach and how to derive the main equations.

As introduced earlier, large eddy simulations are based on the assumption that small-scale turbulent eddies are more isotropic than the large ones, and are responsible for energy dissipation in the mean. Modelling the small scales, while resolving the larger eddies, may be very beneficial: first, since most of the momentum transport is due to the large eddies, model inaccuracies are less critical; secondly, the modelling of the unresolved scales is easier since

they tend to be more homogeneous and isotropic than the large ones, which depend on the boundary condition.

Thus LES is based on the use of a *space filtering* operation: a filtered variable is denoted by an overbar and is defined as:

$$\overline{f}(x) = \int_D f(\mathbf{x}')G(\mathbf{x}, \mathbf{x}', \overline{\mathbf{\Delta}})\ \mathrm{d}\mathbf{x}' \tag{3.19}$$

where D is the entire domain and G is the filter function. It is easy to show that if G is function of $\mathbf{x} - \mathbf{x}'$ only, differentiation and filtering operation commute. Here $\overline{\Delta}$ represent the *filter width* that is the smallest solved length scale. The size of $\overline{\Delta}$ should be chosen so that the eddies of size $\overline{\Delta}$ can be represented with the chosen grid size. Usually $\overline{\Delta}$ is taken equal to:

$$\overline{\Delta} = nh$$

with

$$h = (h_x h_y h_z)^{1/3} \qquad \text{or} \qquad h = (h_x^2 + h_y^2 + h_z^2)^{1/2}$$

where h_x, h_y and h_z are the grid spacing in the three directions. The best value of n has been subject of debate. Several authors proposed values of n spacing from 1 to 8 depending on the differencing scheme order. Lund (2003) concluded that the use of a high value of n is not cost effective, in the sense that reducing both n and $\overline{\Delta}$ gives more accurate results that reducing h with a fixed $\overline{\Delta}$ at the same cost.

The most commonly used filter functions are:

- the sharp Fourier cutoff filter (defined in wave space):

$$\widehat{G}(\kappa) = \left\{ \begin{array}{ll} 1 & \text{if } \kappa \leq \pi/\overline{\Delta} \\ 0 & \text{otherwise} \end{array} \right\} \tag{3.20}$$

- the Gaussian filter:

$$G(x) = \sqrt{\frac{6}{\pi \overline{\Delta}^2}} \exp\left(-\frac{6x^2}{\overline{\Delta}^2}\right) \tag{3.21}$$

- the tophat filter in real space:

$$G(x) = \left\{ \begin{array}{cc} 1/\overline{\Delta} & \text{if } |x| \leq \overline{\Delta}/2 \\ 0 & \text{otherwise} \end{array} \right\} \tag{3.22}$$

Keeping this in mind we can now go back to the Navier-Stokes equation and derive from that their LES form. For incompressible flows, the Navier-Stokes equations are:

$$\begin{gathered} \operatorname{div}(\mathbf{u}) = 0 \\ \frac{\partial u_i}{\partial t} + \operatorname{div}(u_i \mathbf{u}) = -\frac{1}{\rho}\frac{\partial p}{\partial x} + \frac{1}{\rho}\mu \operatorname{div}(\operatorname{grad} u_i) \end{gathered}$$

Exploiting the linearity of the filtering operation we can swap the filtering and the differentiation order. Filtering the first equation leads to the LES continuity equation:

$$\operatorname{div}(\overline{\mathbf{u}}) = 0 \tag{3.23}$$

Repeating the process for the momentum equation gives:

$$\frac{\partial \overline{u_i}}{\partial t} + \operatorname{div}(\overline{u_i}\overline{\mathbf{u}}) = -\frac{1}{\rho}\frac{\partial \overline{p}}{\partial x} + \frac{1}{\rho}\mu \operatorname{div}(\operatorname{grad} \overline{u_i}) \tag{3.24}$$

We now face the problem that we need to compute the convective terms of the form $\operatorname{div}(\overline{\phi\mathbf{u}})$ on the left hand side of the equation, but we only have available the filtered velocity field $\overline{u}$, $\overline{v}$, $\overline{w}$ and pressure field $\overline{p}$. We can "decompose" this contribution writing

$$\operatorname{div}(\overline{\phi\mathbf{u}}) = \operatorname{div}(\overline{\phi}\overline{\mathbf{u}}) + (\operatorname{div}(\overline{\phi\mathbf{u}}) - \operatorname{div}(\overline{\phi}\overline{\mathbf{u}})) \tag{3.25}$$

and substituting this in the filtered momentum equation

$$\frac{\partial \overline{u_i}}{\partial t} + \operatorname{div}(\overline{\phi}\overline{\mathbf{u}}) = -\frac{1}{\rho}\frac{\partial \overline{p}}{\partial x} + \frac{1}{\rho}\mu \operatorname{div}(\operatorname{grad} \overline{u_i}) - (\operatorname{div}(\overline{\phi\mathbf{u}}) - \operatorname{div}(\overline{\phi}\overline{\mathbf{u}})) \tag{3.26}$$

The last term in 3.26 is the contribute of the filtered scales. Since we want to solve only the filtered variables, the term $\operatorname{div}(\overline{\phi\mathbf{u}})$ cannot be directly

solved. We can however write

$$\operatorname{div}(\overline{\phi\mathbf{u}} - \overline{\phi}\overline{\mathbf{u}}) = \frac{1}{\rho}\operatorname{div}\tau_{ij} = \frac{1}{\rho}\frac{\partial\tau_{ij}}{\partial x_j} \tag{3.27}$$

where

$$\tau_{ij} = \rho(\overline{\phi\mathbf{u}} - \overline{\phi}\overline{\mathbf{u}}) = \rho(\overline{\phi u_j} - \overline{\phi}\overline{u_j}) \tag{3.28}$$

τ_{ij} is therefore a convective momentum transport due to the interaction between the unresolved eddies. These are usually called *sub-grid-scale stresses* or SGS. We can now separate each variable in his filtered and unfiltered component. So that

$$\phi(\mathbf{x}, t) = \overline{\phi}(\mathbf{x}, t) + \phi'(\mathbf{x}, t) \tag{3.29}$$

Substituting this in the equation of τ_{ij} we obtain (omitting some mathematical manipulation):

$$\tau_{ij} = \underbrace{(\rho\overline{\overline{u_i}\overline{u_j}} - \rho\overline{u_i}\overline{u_j})}_{\text{(I)}} + \underbrace{(\rho\overline{\overline{u_i}u_j'} + \rho\overline{u_i'}\overline{u_j})}_{\text{(II)}} + \underbrace{\rho\overline{u_i'u_j'}}_{\text{(III)}} \tag{3.30}$$

Here we can recognise three groups of contributions:

(I) **The Leonard Stresses** L_{ij} that are due to effects at resolved scale. They are caused by the fact that a second filtering operation makes a change to filtered flow variables, i.e. $\overline{\overline{\phi}} \neq \overline{\phi}$.

(II) **The cross - stresses** C_{ij} that are due to the interaction between the SGS eddies and the resolved flow.

(III) **The Reynolds LES stresses** R_{ij} that are caused by convective momentum transfer due to interactions of SGS eddies.

Both Leonard and Cross stresses are computed approximately. Reynolds stresses instead are modelled with a so-called SGS turbulence model. Several SGS models have been proposed with several degrees of complexity. Here we'll present the Smagorinsky-Lilly SGS model. This model is one of the first models proposed and have been widely validate.

The idea behind the Smagorinsky model is that local SGS stresses R_{ij} are taken to be proportional to the local rate of strain of the resolved flow $\overline{S}_{ij} = \frac{1}{2}(\partial\overline{u}_i/\partial x_j + \partial\overline{u}_j/\partial x_i)$.

$$R_{ij} = -2\mu_{SGS}\overline{S}_{ij} + \frac{1}{3}R_{ij}\delta_{ij} \tag{3.31}$$

where ν_{SGS} is a proportionality constant. The last term ensure that the sum of the modelled normal SGS stresses is equal to the kinetic energy of the SGS eddies. In the current literature this equation is used to describe the whole stress τ_{ij} including in it also the Leonard and the cross stresses.

$$\tau_{ij} = -2\mu_{SGS}\overline{S}_{ij} + \frac{1}{3}\tau_{ij}\delta_{ij} \tag{3.32}$$

To define the sub-grid viscosity μ_{SGS} the Smagorinsky-Lilly model relies on the Prantl mixing length model for RANS and and assumes that we can define a kinematic SGS viscosity ν_{SGS} (dimensions m^2/s), which can be described in terms of one length scale and one velocity scale and is related to the dynamic SGS viscosity by $\nu_{SGS} = \mu_{SGS}/\rho$. Since the size of the SGS eddies is determined by the details of the filtering function, the obvious choice for the length scale is the filter cutoff width Δ. As in the mixing length model, the velocity scale is expressed as the product of the length scale Δ and the average strain rate of the resolved flow $\Delta \times |S|$, where$|S| = \sqrt{2\overline{S}_{ij}\overline{S}_{ij}}$. Thus, the SGS viscosity is evaluated as follows:

$$\mu_{SGS} = \rho(C_{SGS}\Delta)^2\sqrt{2\overline{S}_{ij}\overline{S}_{ij}} \tag{3.33}$$

where C_{SGS} is a constant of the model.

Based on the second Kolmogorov hypothesis, the behaviour of SGS eddies should be universal; the C_{SGS} constant should therefore be universal too. However different studies showed that the correct value of C_{SGS} vary from 0.1 to 0.25. These differences in C_{SGS} values are attributable to the effect of the mean flow strain or shear. This gave an early indication that the behaviour of the small eddies is not as universal as was assumed at first and that successful

LES turbulence modelling might require case-by-case adjustment of C_{SGS} or a more sophisticated approach. This case-by-case adjustment is anyway less difficult and critic than the RANS one, where the involved constants and arbitrary variables are much more numerous and relevant.

Chapter 4

Wind tunnel tests

In the next chapter we will present the tests performed in the wind tunnel of the Politecnico di Milano (hereafter PoliMi). We will briefly introduce the wind tunnel testing technique, focusing then on the preparation of this test and on the obtained result. Particular attention will be given to the inbound flow simulation, both on the technique used and on the results.

The experiments were conducted for a study carried out by the University of Reggio Calabria regarding the internal pressure on hangar-like buildings. In this context we will use the pressure data acquired on the external surface. The simple geometry of the model allows to compare a basic case without focusing on *ad hoc* solutions. Future works could include the simulation of the internal cavity and it's pressure.

4.1 The wind tunnel of Politecnico di Milano

The tests have been carried out in the wind tunnel of PoliMi. This facility is a closed circuit wind tunnel that developed on two floors as can be seen in figure 4.1. The lower chamber has a cross-section equal to $4m \times 4m$ and is used for test that require high-speed ($V_{max} = 55m/s$) and low-turbulence ($I_u < 0.1\%$) such as the aero-spatial ones. The upper chamber instead has a bigger cross-section equal to $14m \times 4m$ and a length equal to $35m$. Here the maximum speed reachable is equal to $16m/s$ with a minimum turbulence

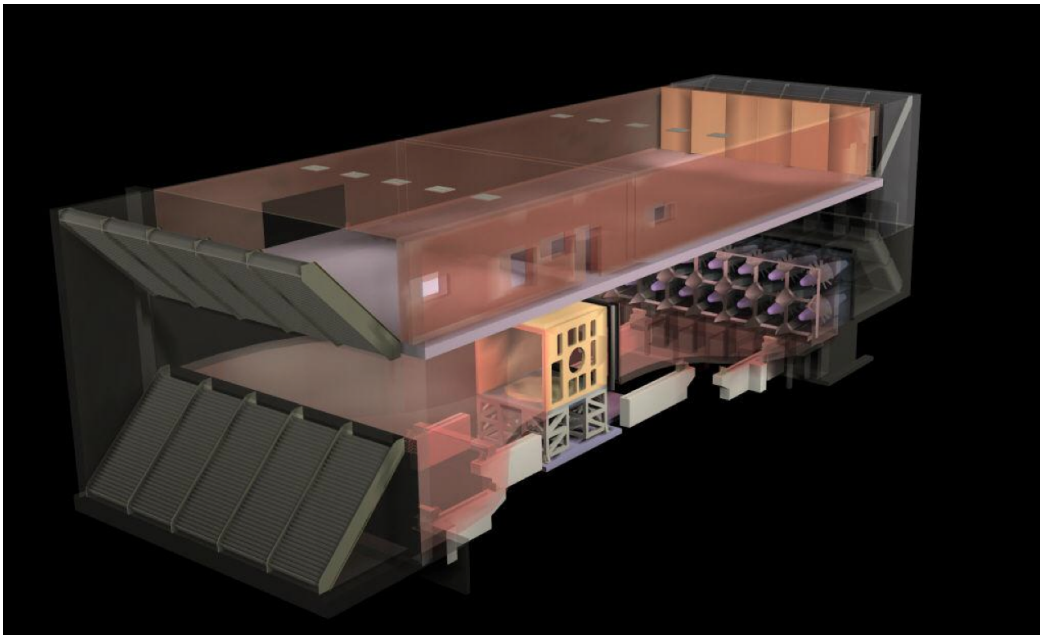

Figure 4.1: The Wind Tunnel of PoliMi

intensity of 2%. The wind flow is generated by 14 turbines, each one with a maximum power of 1.5MW placed after the high-speed chamber. To dissipate the heat generated by the turbines, before the low-speed chamber is placed a heat-exchanger.

The length of the upper chamber allows to develop a proper and stable boundary layer. The model get placed at the centre of a rotating table located at the end of the low-speed chamber with a radius of $6.5m$ that allow to rotate the model to simulate different wind-directions.

4.2 Wind Tunnel scaling technique

As said earlier, the scaling is one of the biggest problem in the wind tunnel testing technique. The correct scaling of the model is based on the assumption that the phenomenon is governed by a certain number of non-dimensional parameter. To identify these parameters, the first step is to identify the dimensional quantities that affects the problem. The force acting on the body F is therefore function of:

- the fluid density ρ
- the fluid viscosity μ
- the flow free-stream velocity U
- a characteristic length L
- a frequency f
- the gravitational acceleration g

The correct way to extract the non-dimensional parameter from these quantities can be found studying the equation of motion of a body subject to wind forces. Using the dimensional analysis can be found four non-dimensional groups can be found:

- the pressure coefficient $C_p = \frac{F}{\frac{1}{2}\rho U^2 L^2} = \frac{p}{\frac{1}{2}\rho U^2}$
- the Reynolds number $Re = \frac{\rho U L}{\mu}$
- the Strouhal number $St = \frac{fL}{U}$
- the Froude number $Fr = \frac{U}{\sqrt{gL}}$

Using these quantities can be written:

$$C_p = f\left(Re, St, Fr\right) = f\left(\frac{\rho U L}{\mu}, \frac{fL}{U}, \frac{U}{\sqrt{gL}}\right) \tag{4.1}$$

A correct scaling should therefore keep these groups equal. Lets see what this would mean. Indicating with subscript r the quantities related to the real-scale and with subscript m those related to the model scale:

$$\left(\frac{\rho U L}{\mu}\right)_r = \left(\frac{\rho U L}{\mu}\right)_m \qquad \left(\frac{fL}{U}\right)_r = \left(\frac{fL}{U}\right)_m \qquad \left(\frac{U}{\sqrt{gL}}\right)_r = \left(\frac{U}{\sqrt{gL}}\right)_m \tag{4.2}$$

Lets call λ the ratio of each quantity between full-scale and model scale:

$$\lambda_L = \frac{L_r}{L_m} \qquad \lambda_U = \frac{U_r}{U_m} \qquad \lambda_f = \frac{f_r}{f_m} \tag{4.3}$$

We can now insert equations 4.3 in 4.2. Assuming $\rho_r = \rho_f$ and $\mu_r = \mu_f$ (that are both true if the wind tunnel uses air):

$$\lambda_L = \frac{1}{\lambda_U} \qquad \lambda_f = \frac{\lambda_U}{\lambda_L} \qquad \lambda_L = \lambda_U^2 \tag{4.4}$$

It is immediate to see that Reynolds and Froude correct scaling cannot be both achieved at the same time (excluding the extreme case $\lambda_L = \lambda_U = 1$ that represent *non-scaling*).

The Froude condition expresses the importance of the gravitational and buoyancy effects of the flow. Assuming these to be negligible when thermal effects are, one could choose to ignore this condition and to scale using the Reynolds condition $\lambda_L = \lambda_U^{-1}$. This however would lead to huge practical problems. E.g. assuming a model 50 times smaller than the real version, λ_L would be equal to 1/50. To have the same Reynolds in the wind tunnel simulation, a wind speed 50 times faster would then be required. This means that if the full-scale reference wind speed is equal to $25m/s$, in the wind tunnel would be required a wind speed equal to $1250m/s$! This is of course completely undoable.

This problem is the main problem with wind tunnel tests. The experiments are carried out assuming the phenomena to not be Reynolds dependent. This statement is not completely wrong (otherwise wind tunnel results would be completely useless), but it's not even completely true. The difference in the Reynolds number is more severe when the geometry is smooth, without sharp edges, such as circular tower or spheres, because it affects the behaviour of the detachment of the boundary layer In the case of sharp edges - such as the one presented in this thesis - the boundary layer detachment is governed by the geometry and the Reynolds number is less critical.

Another problem related to the scaling of the rounded objects is that the flow behaviour strongly depends by the surface roughness. Since this roughness in case of concrete or glass is usually measured in micrometres, it's easy to see how a correct scaling of it is extremely hard.

Going back to the three scaling condition, the Strouhal condition is therefore the only one respected assuming frequency scale equal to the ratio of the

velocity scale and the length scale.

In the experiment presented in this thesis the length-scale has been chosen for geometrical and practical reasons. The second scale chosen instead was the velocity-scale. This has been chosen as the ratio between the maximum wind speed achievable inside the wind tunnel at the roof-heigh - equal to $10m/s$ - and the maximum wind speed expected by the Eurocode at the same heigh with a return period of 50 years - equal to $27m/s$. The other scales are than obtained through dimensional analysis.

The scales used in this experiment are:

Quantity	Scale
Length	1/50
Speed	1/2.7
Time	1/18.51

Table 4.1: Scales used in the experiment

4.3 Blockage effect on the flow

From what have been said in section 4.2 one could think to use the smallest λ_L that allow the scaled model to fit in the wind tunnel. The presence of the model however alters the flow in the tunnel, reducing the section and accelerating the flow on the side of the model. This is called *blockage effect*.

This effect alters the pressure on the building modifying the results. The strength of it depends by the *blockage ratio* defined as the percentage of the wind tunnel cross-section occupied by the model, i.e. it is equal to S/C where S is a nominal cross-section area of the model and C is the cross-section area of the wind tunnel. The effect of the blockage effect of the pressure can be evaluated with the equation

$$C_{D_c} = C_D \frac{1}{1 + KS/C} \tag{4.5}$$

To use this formula one should evaluate the coefficient K that is usually

tricky to compute.

To workaround this problem, the blockage ratio should be kept smaller than 5%. This implies the model to not be too big depending on the wind tunnel size.

It is clear as the two conditions, Reynolds and blockage, has opposite requirements. The optimal condition is therefore to have the biggest model possible with a blockage ratio lower than 5%. The cross-section of the wind tunnel of PoliMi is equal to $4m \times 14m = 56m^2$, while the maximum model section is about $2.2m \times 0.3m = 0.66m^2$. The ratio between these surfaces is equal to $\sim 1.2\%$ that is below the blockage limit.

4.4 Atmospheric Boundary Layer reproduction

The reproduction of a correct inbound flow strongly affects the pressure distribution on the building. This aspect is therefore critical for a good simulation.

Inside the wind tunnel the ABL is reproduced using mechanical device that can alter the structure of the flow. In particular two kinds of devices have been used: a group of 9 spires $2.5m$ tall located at the beginning of the wind tunnel and a set of roughness pyramids placed on the ground with an height ranging from $9cm$ to $18cm$ (figure 4.2).

The spires are used to generate the bigger structures and to fasten the creation of the boundary layer. The ground roughness instead slows down the wind near the ground with an effect similar to the buildings and the trees in the real scale scenarios. There are several papers relating the size and the distance of the roughness blocks to the boundary layer generated. They, however, often refers to cubic or cylindrical blocks. The approach used for the set-up is based on the experience of the operator and on a *try-and-error* approach.

The target profile z_0 is chosen scaling the real-scale profile (that could be ether measured or taken from a code) by the same λ_L used for the geometric

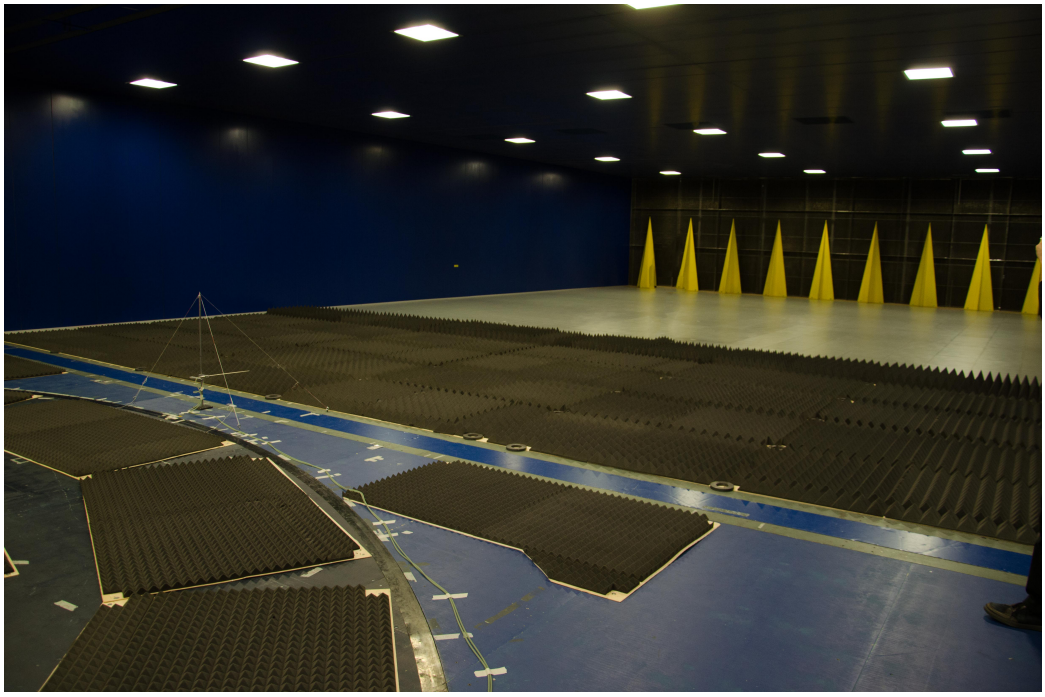

Figure 4.2: Wind tunnel turbulence generators

scaling of the structure.

4.4.1 Profile measurement

To verify that the generated profile coincides with the target one, it has to be measured and classified. This is done using a *cobra probe* (figure 4.3 that is a multi-hole probe that, through direct calibration, can measure the three components of the inbound flow in a point.

This is moved along a vertical track through an engine. Acquiring time histories ad different height is possible to compute al the quantities presented in 2.3. It worth to be noted that the time histories acquired at different height are not acquired simultaneously. At each height the probe acquire a 5 minutes time history to minimize the statistical error.

Hence the integral length scale L_u^z, L_v^z and L_w^z cannot be computed. Even more so the integral scale L_u^y, L_v^y and L_w^y cannot be computed as well since the probe doesn't moves in the y direction at all. The only integral scales

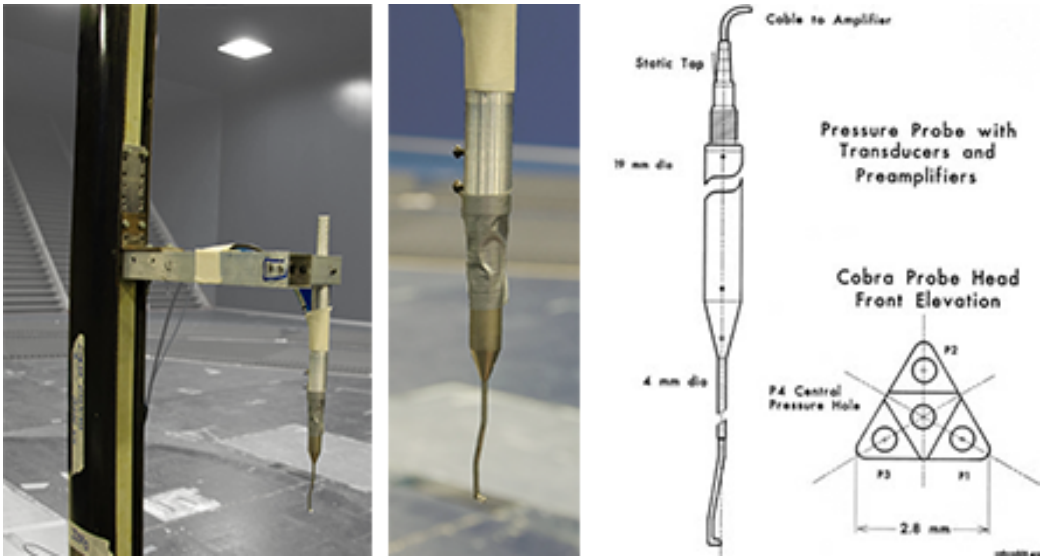

Figure 4.3: Cobra probe

that can be computed are the ones along x, which can be evaluated using the Taylor hypothesis (ref. 2.3.1).

4.4.2 Results

Below we present the acquired data and we briefly discuss it.

In figure 4.4 we compare the mean velocity profile obtained in the wind tunnel to the Eurocode profile (Equation 2.10) corresponding to a Cat. II terrain (open field, $z_0 = 5cm$) with same U_{ref}. The profile shows a good agreement with the theoretical one. In the figure only the portion up to $1.5m$ is represented, since during this testing campaign the profiles data has been acquired only up to that height.

In figure 4.5 the same comparison with the Eurocode standard profile has been carried out for the turbulence intensity. This plot deserves a bit more comments. The blue lines represent the streamwise turbulence component. The portion between $10cm$ and $60cm$ shows good agreement. The same thing can't be said for the rest of the profile; below $10cm$ the flow is less turbulent that how it should be, this is probably due to the fact that in the wind tunnel configuration there are a couple of meters upwind to the model

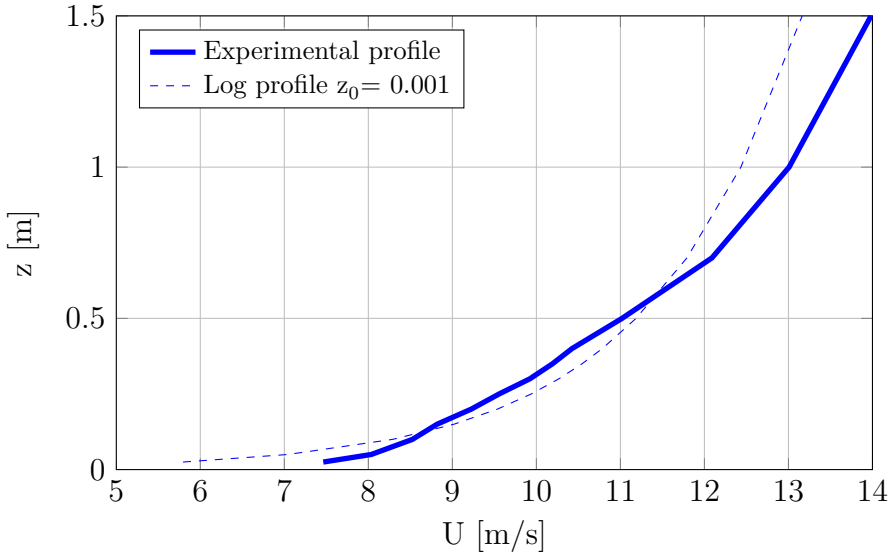

Figure 4.4: Mean velocity profile

lacking roughness. The flow in the lowest part of the floor is the one expected to change sooner as soon the ground roughness changes. Since the flow is moving from a very rough area to an area almost perfectly flat, the profile is expected to become faster and less turbulent starting from the bottom and gradually proceeding upward. Paying attention, this can be seen also in the mean velocity profile analysed a moment ago.

Another consideration that can be done is that the Eurocode law expect the turbulence to tend to plus infinity with decreasing z. This is of course non-physical and such behaviour cannot be expected.

The reason for the disagreement above $z = 0.6m$ is somehow similar: as just said, when the flow moves to a different roughness it starts to evolve beginning from the bottom. The roughness is positioned starting "only" from $15m$ upwind to the model. The rough area is therefore not long enough to generate a completely stable profile. In this testing campaign the model was only $30cm$ tall, so the flow above $60cm$ wasn't really important. If there were a higher model (such as an high-rise building) more roughness could have been placed in the first part of the tunnel to give the flow a longer time

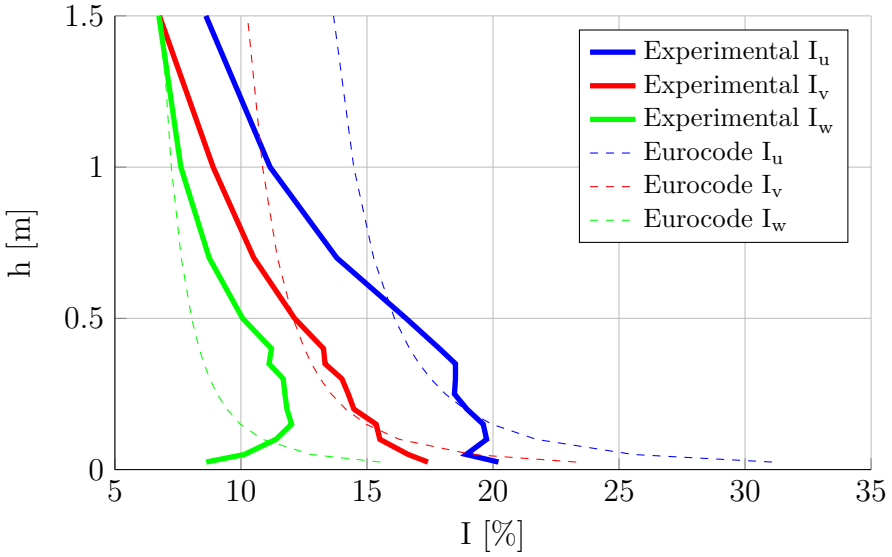

Figure 4.5: Turbulence intensity profile

to develop.

Similar comment to those that we just did for the streamwise turbulence can be done for the span-wise - red - one. The comments on the vertical one are a little different. As one can see from figure 4.5, the vertical components show a different shape from the one expected from the Eurocode equation. This time is the Eurocode equation to be approximated. Full scale measurements indeed show the same kneel that can be seen in the vertical turbulence profile. This has already been explained in section 2.3.3 and it's due to the limitation that the ground imposes to the vertical movements near it.

In figure 4.6 we can see the Integral scales profiles. In this plot is very evident how the integral length scales generated in the wind tunnel are not big enough. Observing the streamwise - blue - one we can see how at z equal to $1m$ the Eurocode expect L_u^x to be about $3m$. So large eddies are really hard to reproduce inside the wind tunnel because of the physical dimensions of it. We need to remember from figure 2.3 that the time scale of the structures is somehow proportional to their length scale. These large eddies therefore have a very long duration compared to the time that the flow takes from the

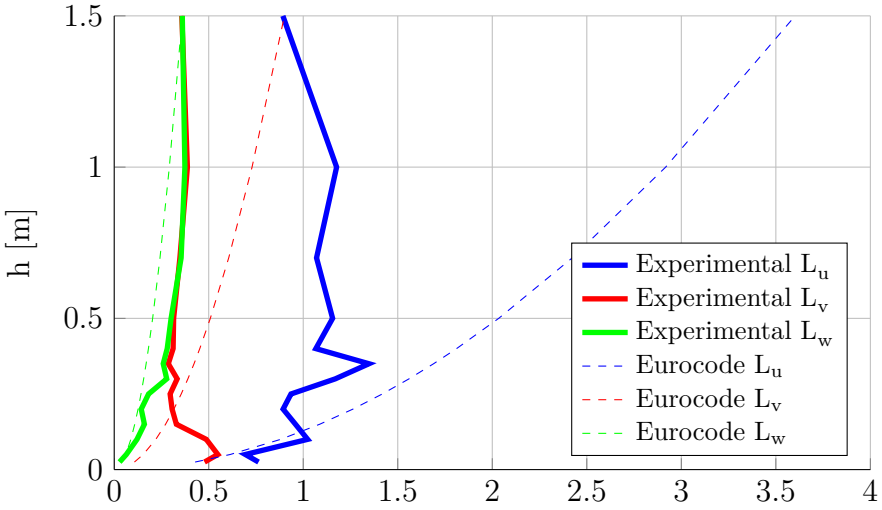

Figure 4.6: Integral scales profile

inlet to the measure point (a *wash time* is approximately $3s$). They don't have therefore the time to form. The spires located at the beginning of the wind tunnel should have the task to generate big eddies and increase the length scales, but how can be seen they are not enough to fit the Eurocode profile.

The problem is present also in span-wise and vertical length scales, even if less severe.

Lastly in figure 4.7 we can see the power spectrum of the streamwise velocity component $30cm$ above the ground. It has been non-dimensionalised as the Von Karman spectrum (equation 2.22). The spectrum completely agrees with the theoretical one, both for the peak and, more important, for the slope of the inertial range.

4.4.3 Final remarks on the ABL simulation in the wind tunnel

From the results presented appears a good degree of agreement between the wind tunnel simulated ABL and the code expected one. Few remarkable

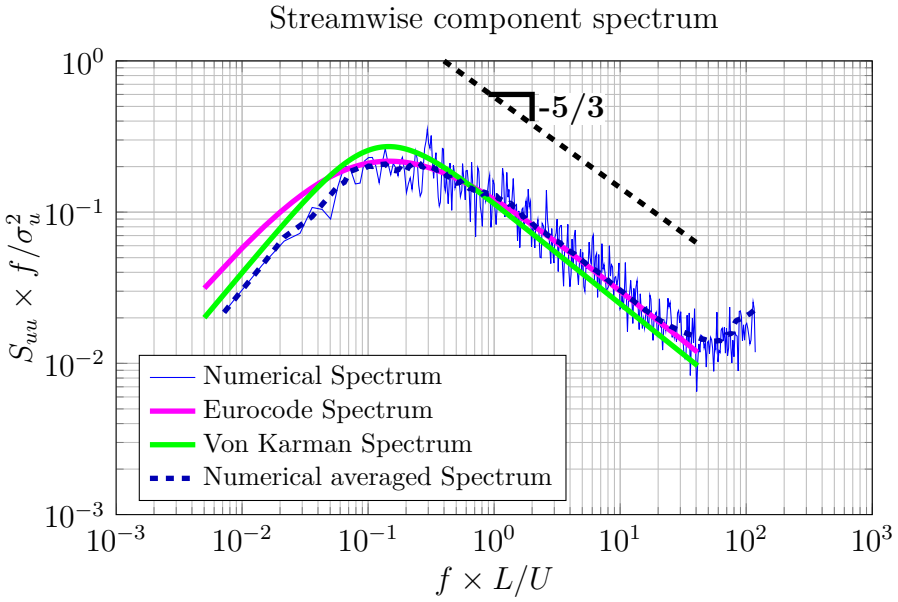

Figure 4.7: Spectrum at $z = 0.3m$

differences however exist and are mainly attributed to the fact that the ABL doesn't have enough space to develop completely. It is important to remark that the aim of this campaign was to have a good incoming flow for z below $30cm$ and this has been achieved. It is anyway clear that the wind tunnel simulations don't allow to have a completely arbitrary incoming flow, but that a certain degree of compromise has to be accepted.

A final remark that has to be done is that, although wind tunnel testing is an established technique used extensively in wind engineering, it is still a simulation prone to error and must therefore be benchmarked. Comparisons between full scale tests on existing buildings and wind tunnel tests have shown good correlation although discrepancies do exist (Hoxey et al., 2002). Comparisons among different wind tunnel tests for the same scenario have been used for sensitivity analyses and to quantify the reliability of the modelling process. Such reliability comparisons have shown small but systematic errors indicating modelling discrepancies as opposed to random variation Cook (1990).

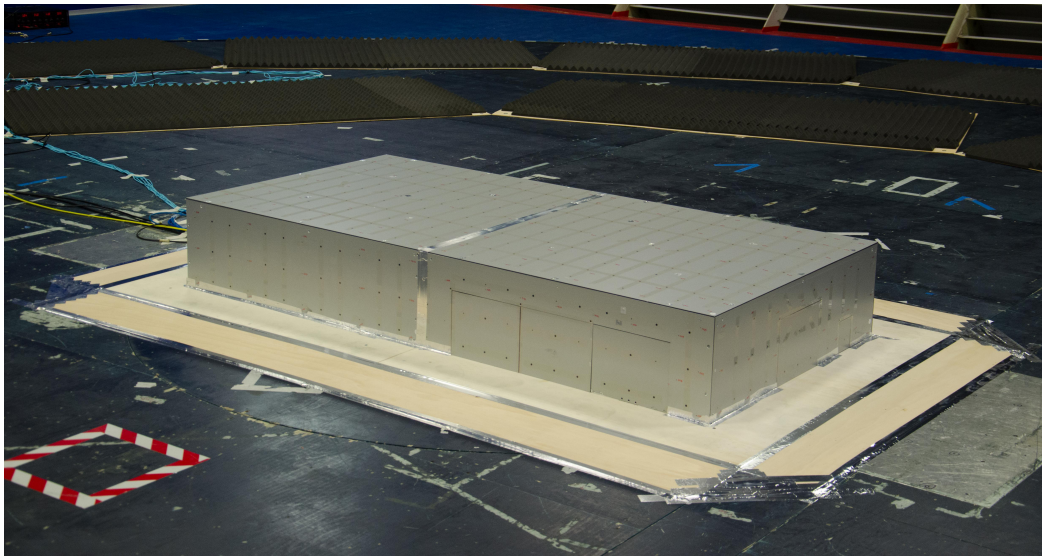

Figure 4.8: The hangar model used in the wind tunnel tests

4.5 Wind tunnel test on the building

Following the reproduction of a correct inbound flow, the next step is to prepare the test model and then run the test acquiring the pressure data. In the next section we present the main characteristic of the model and then the set-up used for the tests; finally we show and discuss the results of the simulations.

The experimental data were made possible thanks to joint research with Professor F. Ricciardelli, University of Reggio Calabria, on the internal pressures of large span buildings with large openings for the PhD thesis of Eng. Giuseppe Vazzana (being submitted in next future). Some results of this research are already published in Vazzana, Ricciardelli, Zasso, and Giappino (2013).

4.5.1 Hangar model

The model used in this thesis had purpose of represent a hangar-like building and not a particular building. For this reason, it had a very simple shape with sharp edges and flat surfaces. It didn't show any particular feature or detail.

The model was a parallelepiped with sides of $1m$ x $2m$ and $30cm$ tall. On the sides there were several openings that reproduced the doors on the hangar. There were three doors side by side on the longer side and two separated doors on the short side. Each door was $25cm$ wide and $20cm$ tall, with the exception of a small door on the short side that was $8cm$ wide and $10cm$ tall. The rightmost door of the three on the front has been equipped with a spring-opening mechanism that has been used to simulate the sudden failure of one door during a storm.

The surface of the model consisted of $5mm$ thick Alubond panels. Each panel had been punctured with three different size sets of hole. Two sets simulated a distributed porosity of the wall: a low-porosity equal to 0.1% of the total surface obtained using $6mm$ holes; and a high-porosity equal to 1% of the total surface obtained using $12mm$ holes. A third set of smaller holes was used to measure the surface pressure; we will better explain this in the following section.

The edges of the building have been covered with aluminium tape to try to make the edges as sharp as possible and avoid possible effects due to the sides of the Alubond panels. The aluminium tape has also the purpose to minimise unwanted air leakage inside the model. For the same reason the aluminium tape has been placed also on the edges against the ground and on the hole in the base panel where were the electric cables connecting the instrumentation inside the model with the control room.

4.5.2 Model instrumentation

The model has been instrumented with 6 PSI ESP-32HD high-speed pressure scanners, each with 32 pressure sensors. The scanners are connected to a Chell QUADdaq data acquisition system that has a sampling frequency equal to 500Hz. The data are therefore acquired with a MATLAB script and stored on file.

Each pressure scanner was connected with a hole on the hangar surface through a rubber tube. Few pressure *taps* were connected to a tube ending at the centre of the internal volume and one pressure tap has been left without tube as reference.

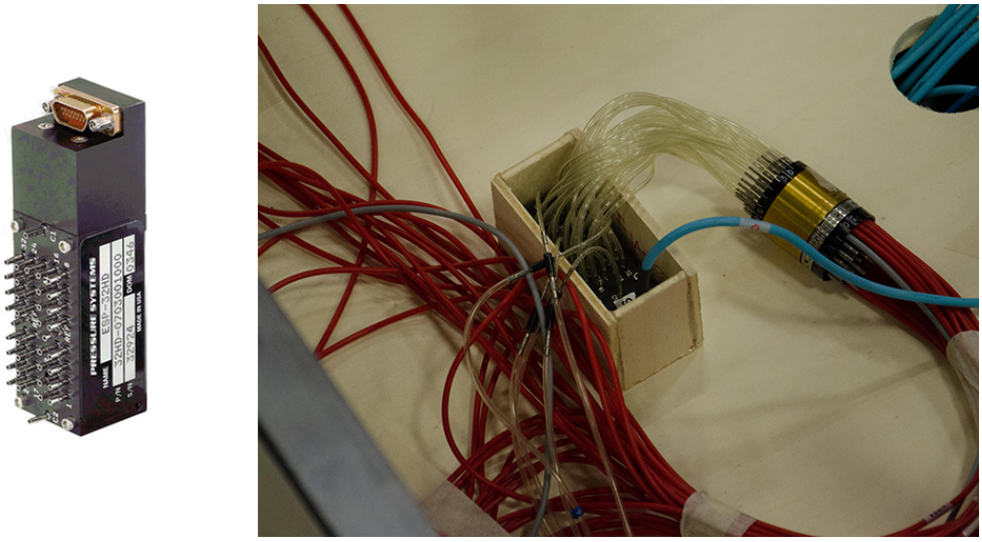

Figure 4.9: Left: the Chell ESP-32HD pressure scanner; Right: the pressure scanner and the tubing system inside the model

The tube length was exactly the same for all tubes and was equal to $0.6m$. This way all the pressure taps has the same *frequency response function* that has been "inverted" during the post-processing.

During the test a Pitot tube located about $7m$ upwind to the building recorded the mean velocity of the field (it can be seen on the left of figure 4.2). This data has been used to compute the reference velocity for the calculation of the pressure coefficient as will be explained in the next section.

4.5.3 Execution of the tests

The tests have been executed with different orientation of the building and in different configuration. As we've stated before the target of this test campaign was to study the behaviour of the internal pressure. To do so, many different combinations of open door and porosity has been tested with different wind directions.

Since the aim of this thesis is to reproduce the behaviour of the external pressure we will just focus on the - so-called - *zero test*, that is: no porosity and no open door. Future work could include the study of the internal pressure with different porosity and/or with open doors.

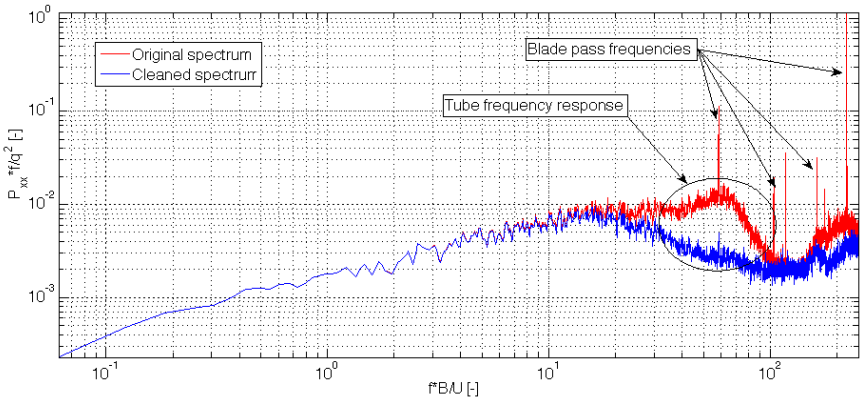

Figure 4.10: Original pressure spectrum and cleaned one

4.5.4 Results

Before doing any analysis of the pressure data acquired in the wind tunnel, it has been necessary to "clean" these data from unwanted frequency contributions. There were mainly two noise sources: the frequency response function of the tubes and the blade-pass frequency of the wind tunnel engines. The first resulted in a large peak at about $30Hz$. This has been removed inverting the frequency response function of the tubes that was been previously experimentally measured.

The obtained spectrum still shows clearly some very sharp peaks. There has been some doubt about what these peaks could be. To demonstrate that these peaks were due to the motor, the blade pass frequency of the motor has been calculated using the equation:

$$BPF_1 = P_{eng} \cdot RPM_{100\%} \cdot N_{blades}/60 \tag{4.6}$$

where P_{eng} was the engine percentage of power used for the test equal to 92%, $RPM_{100\%}$ is the full power round per minute of the engines, equal to $1200rpm$ and N_{blades} is the number of blades per rotor.

From this equation the first blade pass harmonic BPF_1 has been calculated. The following harmonics has been calculated just as a product of this one. So $BPF_n = n \cdot BPF_1$. The resulting frequency for the first 5 harmonics was: $220.8Hz$, $441.6Hz$, $662.4Hz$, $883.2Hz$ and $1104Hz$. These are far above

the acquisition frequency of $500Hz$. To correctly compute the resulting frequency on the acquired signal has been therefore necessary to compute the *aliased* frequency of them. Using the Nyquist theorem, the aliased frequency is

$$f_{alias} = |N * f_s - f| \,; \tag{4.7}$$

where f_s is the sampling frequency - in this case equal to $500Hz$ -, f is the non-aliased frequency and N is defined as

$$N = \text{round}(f/f_s); \tag{4.8}$$

Superimposing the aliased version of the first 10 harmonics to the spectrum, a very good agreement can be observed for the first 7 harmonics (figure 4.11).

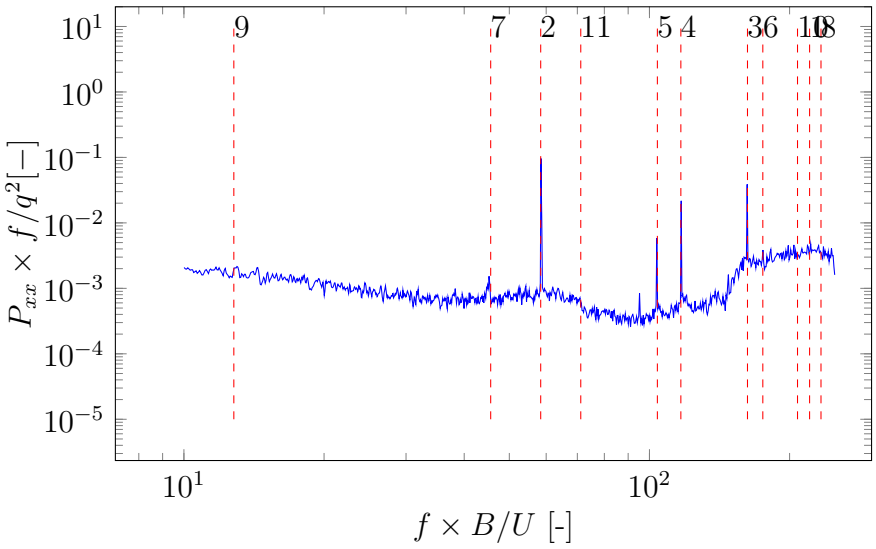

Figure 4.11: Blade pass frequency

To remove this frequency the signal has been filtered with a low-pass filter with cutout frequency equal to $50Hz$.

All the pressure data recorded during the test has been normalised with the equation:

$$C_p = \frac{p}{\frac{1}{2}\,\rho\, U_{ref}^2} \tag{4.9}$$

in this equation U_{ref} is the *expected* velocity at roof height at the centre of the table. This is not measurable since the presence of the model alters the flow. It is therefore computed as:

$$U_{ref} = k\, U_{ref,pitot} \tag{4.10}$$

where $U_{ref,pitot}$ is the reference velocity measured by the Pitot tube described in paragraph 4.5.2 and k is a proportionality constant calculated during the simulations without the building.

Mean value

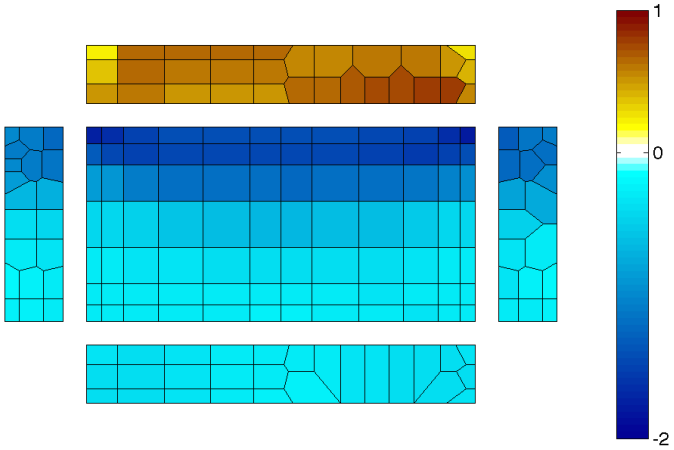

Figure 4.12: Mean value

The C_p mean value map shows a pattern typical of square buildings with sharp edges. The upwind face of the building is the only one with a positive C_p due to the stagnation point of the flow. The pressure coefficient on the rear face and the rear part of the roof is slightly negative, indicating the suction due to the increase of tangential velocity as expected from the Bernoulli equation.

The map shows clearly that the most critical values of C_p are located behind the leading edge of the building where the separation bubble forms. Near the corners where the phenomenon is stronger, the mean C_p reaches values equal to -2

Standard deviation and skewness

Lets analyse the second and third order statistical momentums. The standard deviation is a first index of how much the C_p value fluctuates around its mean. Looking at the map it's evident how the largest fluctuations occur at the corner where the C_p value was already strongly negative.

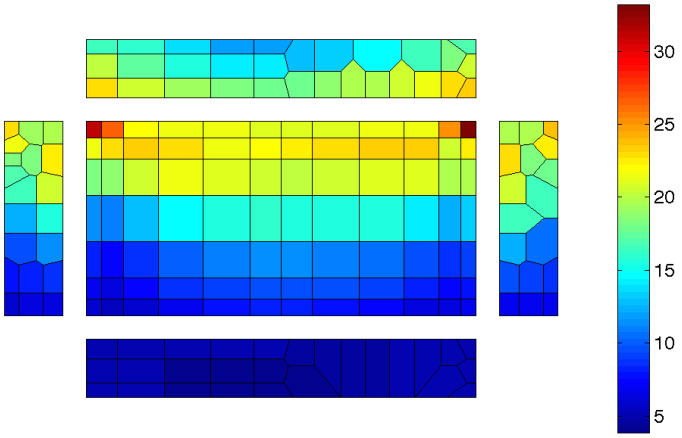

Figure 4.13: Standard deviation

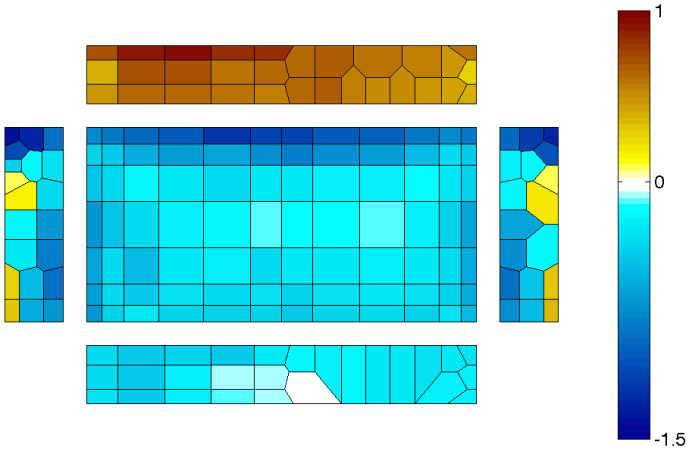

Figure 4.14: Skewness

In these areas the skewness is also strongly negative. The skewness indicates if the oscillations are larger below or above the mean value. In figure

4.15 is easily seen that the fluctuations on the corner of the building are far wider towards the negative values as indicated by the negative skewness.

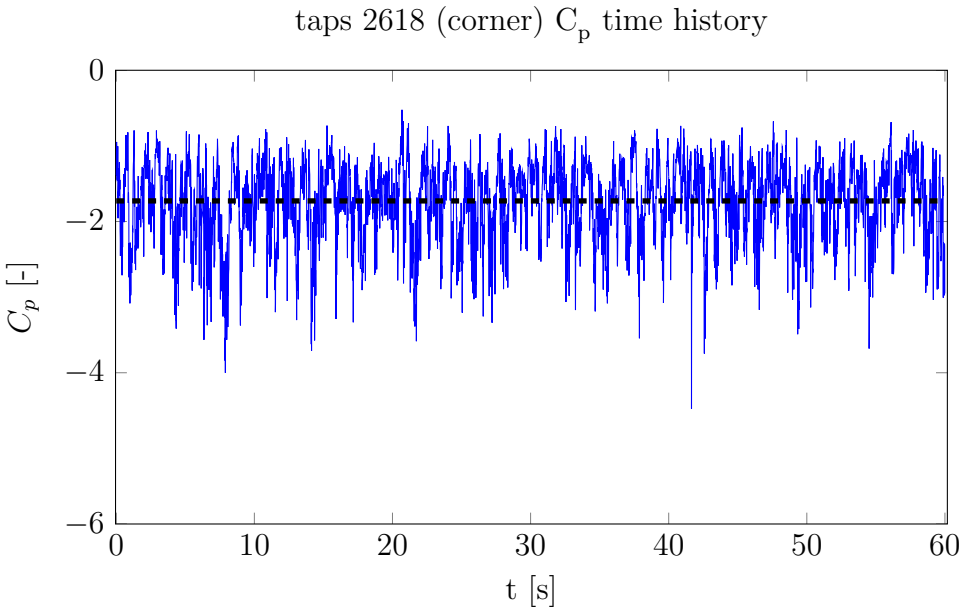

Figure 4.15: C_p time history on the building's corner

Minimum value

What has been said above can be summarized with figure 4.16. Here we can see that the large negative fluctuation of the C_p behind the leading edge cause the C_p to reach strongly negative value that are 2-3 times stronger than the mean value.

This behaviour is the most critical for the civil engineer that is interested in the analysis of the most extreme event that could lead to the failure of the cladding. In this map however we computed only the minimum value over an arbitrary time interval. This can give us a rough overview of the behaviour of the minima but cannot be used as an indicative information to compute the design value. As any random phenomenon, the larger is the number of samples, the larger is the maximum. To compute the design value from a give time history one will need to consider more factors. This we'll be

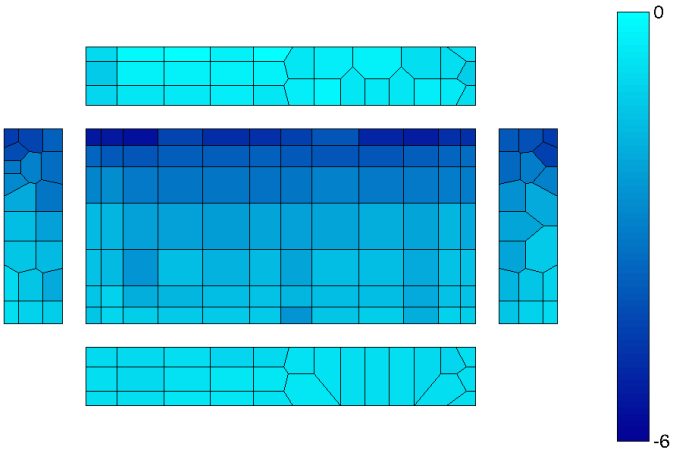

Figure 4.16: Minimum value during wind tunnel simulations

discussed in the last chapter of this thesis where we'll analyse the calculation of the design values for wind engineering applications.

4.5.5 Final remarks on the building simulation in the wind tunnel

In this section we have presented the external pressure obtained in the wind tunnel experiments. We have seen how the most stressed area is a small portion of the roof behind the leading edge and how the mean value by itself is not enough for a correct calculation of the design value. To correctly compute the pressure peak value, a correct standard deviation and skewness must be correctly reproduced.

Chapter 5

CFD reproduction of the experiment

The purpose of this work is to benchmark the CFD as tool for the reproduction of the wind tunnel experiment to evaluate the surface pressure on a building. The choice of reproducing the wind tunnel scaled geometry instead of the full-scale one could seems odd since we have described how the CFD is useful to workaround the limitation imposed by the wind tunnel and in particular the scaling problem. Reproducing the experiment with the same scale and a similar velocity to the wind tunnel ones reintroduce this problem.

The reasons for this choice are that, in a comparison between a full-scale CFD-reproduced phenomenon and a small-scale wind-tunnel-reproduced one, it would have been hard to understand which differences are imputable to the scaling error and which ones to the CFD turbulence model or numeric errors.

The research should therefore be made in two step: a reproduction of the experiment with the CFD using the same geometry and the same inbound flow to validate the chosen CFD technique; and a following reproduction of the full-scale problem analysing the difference with the previous simulation.

This chapter will be divided in eight sections: in the first section we present the current state of the art for the generation of the inflow's ABL, afterwords, we introduce the solver and the boundary conditions that will

be used in the current thesis. Then we present a preliminary benchmark of the CFD technique using the data provided by Y.Yoshikawa obtained at the Tokyo Institute of Technology wind tunnel. In the following section we will benchmark some different CFD set-ups - solvers, schemes, meshing technique, etc. - and we will try to simulate several components of the wind tunnel on their own. Subsequently, in the sixth section, a reproduction of the wind tunnel ABL will be executed; this part has proved to be the most difficult and a correct reproduction of all the characteristics of the ABL to be elusive. In the final part we will present a preliminary try to obtain the surface pressure on the building and we will compare this to the results obtained with different techniques.

5.1 The ABL reproduction in CFD simulations

Data post-processing of the wind tunnel tests results shows how the probabilistic distribution of the fluctuating pressure values around the mean value may be very different from point to point and in particular from region where positive peaks or negative peaks occur (Rocchi, Schito, and Zasso (2010, 2011); Zasso, Rocchi, and Schito (2009)). This experimental evidence is not explainable considering only the mean flow field modification, due to wind-structure interaction, but it may be related to the interaction of the larger turbulence structures, present in the atmospheric boundary layer flow, with those parts of the building that are effective in modifying and stretching the vortexes (edges driving flow separations). This phenomenon is present in the experimental results, since the wind tunnel common practice is to scale the real wind and structure interaction by reproducing a wind field that contains the turbulence structures and by simulating similar statistical properties of the real wind in the site where the structure will be built. The same approach is not usually followed by those CFD numerical simulations that model the incoming turbulence through URANS (Unsteady Reynolds Average Navier Stokes) approaches able to account only for averaged turbulence properties

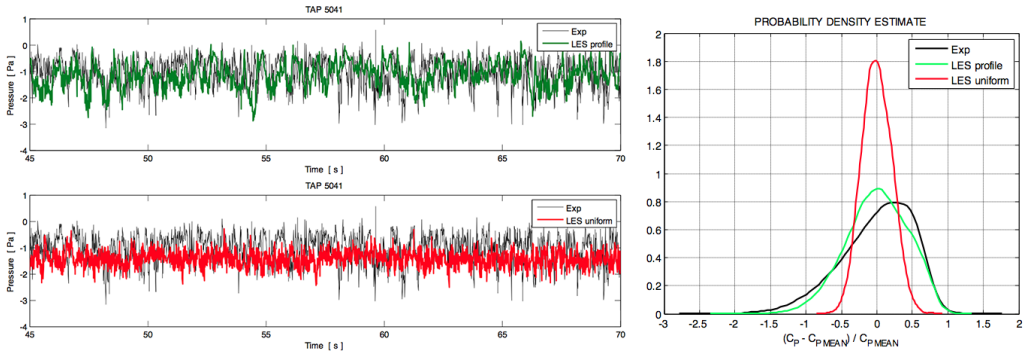

Figure 5.1: Left: C_p time history comparison. Right: probability distribution of $(C_p - C_{p,MEAN})/C_{p,MEAN}$ (image courtesy of Rocchi et al. (2011))

(k,ε,ω) or in those simulations where not realistic uniform turbulence conditions are used as boundary conditions for the incoming wind.

A comparison between Wind Tunnel test and two LES simulations - one reproducing the ABL, while the other with a uniform turbulence condition - performed by Rocchi et al. (2011) highlighted that the extreme values (located in the far tails of the probability distribution) are related to the turbulence structure of the flow. In particular the presence of large low-frequency structures is required to reproduce a real-like probability distribution of pressure fluctuation and to simulate the most demanding peak values in region of separated flow (figure 5.1).

It is therefore mandatory in CFD simulations to correctly reproduce the incoming wind turbulent characteristics in order to define the more appropriate dimensioning peak pressure values. The definition of the incoming wind characteristics becomes therefore a key feature for the modelling of the wind-structure phenomenon.

At the present day, several techniques exists to reproduce the turbulent flow. These can be divided into three main categories: the recycle techniques, the synthetic generation of the inflow turbulence and the driver region technique.

Recycle techniques are modifications of the periodic conditions. In the classic periodic conditions the cells of two separated surfaces get "linked"; the domain thus repeat itself an infinite number of times. When used as inlet-

outlet condition, periodic condition must take into account the *head loss* and the variable boundary layer thickness.

A versatile and flexible recycle technique was proposed by Lund et al. in 1998. This method, which was developed for flat-plate boundary layers, consists of taking a plane of data from a downstream location whose distance is a multiple of the boundary-layer thicknesses δ of the inflow, and rescaling the inner and outer layers of the velocity profiles separately, to account for the different similarity laws that are observed in these two regions. The rescaled velocity profiles are then re-introduced at the inlet. In particular, in the near-wall region inner-layer non-dimensional variables are matched; the velocity of an inlet cell is taken equal to the velocity of a cell at the recycle plane with the same $y+$ (non-dimensional wall distance) instead than one with the same y. In the outer layer, the same consideration is applied, but the rescaling is performed along lines of constant y/δ and a law-of-the-wake is used instead of the logarithmic distribution. To correctly reproduce the flow's integral lengths, the domain must be at least twice as long (or wide) as the wavelength of the longest structure present in the flow, i.e. the cross-correlation of two points separated by a distance equal to half the domain length must be equal to zero.

The main advantage of these methods is that they allow to reproduce a stable an developed flow using small domains. They indeed simulate and infinitely long geometry exploiting the periodic condition.

The main shortcoming is the fact that the inlet must be placed in a region in which the flow is in an equilibrium, well-known condition (flat-plate boundary layer, for instance) and a fairly long fetch must be appended to the region of interest for the recycling. This introduce two difficulties: the fact that, in some flows, an equilibrium region in which scaling arguments can be applied may not exist at all, and that recycling may introduce *spurious* periodicity intro the time-series (see for example, Spille-Kohof and Kaltenbach (2001)).

In wind engineering it is usually possible to apply the recycle technique to generate ABL-like inlet database that can be later used as inlet condition for wind engineering simulations. However, the ABL generated inside the

Wind Tunnel is proved to not be stable and completely developed due to the insufficient length of the test chamber. Moreover, the presence of the spires makes the domain non-periodic. This method is thus not suitable for the purpose of this thesis that is to reproduce a Wind Tunnel-like flow.

Methods that do not use some form of recycling are usually based on the generation of synthetic turbulence, with assigned moments and spectra, through random sequences. Le et al. in 1997 performed calculations of a backward-facing step in which at the inflow they assigned a mean velocity profile, to which random fluctuations with given moments and spectra where superposed. Le at al., however, found that because of the inflow information did not contain the phase information of the real turbulent eddies, the turbulence level decayed rapidly. Only some fairly significant distance downstream of the inflow the turbulent eddies regenerated and the flow field becam realistic again. This proved that without the phase information, inflow conditions cannot be expected to be accurate and the flow must undergo an adjustment, as the turbulent eddies are generated and evolve (i.e. the correct phase information is established) starting from a field in which such information is either absent or incorrect. While it is possible, in principle, to match this structural information using stochastic sequences, the specification of the phase information is more difficult, since it relates to the structure and shape of the turbulent eddies, which is strongly dependent on the type of the flow (e.g. mixing layer or boundary layer) and on the location in the flow (quasi-streamwise vortices are present near a wall, horseshoe vortices and arches farther away).

The inflow method based on synthetic turbulence generation that was described above and similar ones are based on the assumption that turbulence can be specified by using only low-order statistics (mean velocity, spectra, normal and - in some cases - shear Reynolds stresses). One factor that these methods neglect, however, is the initial development of the inflow perturbation. The higher-order statistics of the synthetic turbulence, in fact, do not match those of realistic turbulent flow with the same low-order statistics leading to rapid decay of the perturbations.

In the last decade, different methods to generate inflow conditions, that

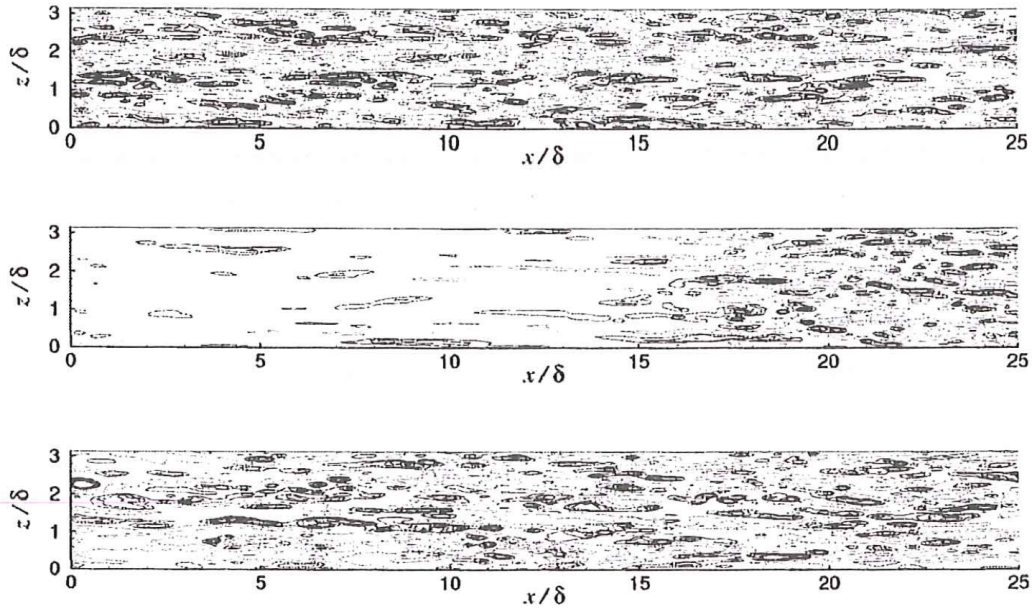

Figure 5.2: Contours of streamwise velocity fluctuations at $y/\delta = 0.01$. From top to bottom: precursor simulation, synthetic turbulence, synthetic turbulence with forcing planes

seeks to establish the correct Reynolds shear-stresses profiles, has been proposed. One, by Spille-Kohof and Kaltenbach, use a synthetic turbulent field at the inflow plane and a number of control planes placed a short distance downstream. At each of these planes a controller is introduced that amplifies the wall-normal velocty fluctuation to match the target Reynolds shear-stress. They found that the forcing superposed on the synthetic turbulence reduced the distance required to achieve realistic statistics in a spatially developing wall-bounded flow very significantly.

A method to generate a completely stable and physically correct flow has not yet been found. An attempt to use one of the latest synthetic turbulence inflow technique to generate a Wind Tunnel-like and a comparison of the pressure distribution obtained with this technique will be discussed in section 5.8.

A third method that has been used to generate inflow condition consists of running a separate - preliminary - calculation of *driver region*. This is usually a Wind Tunnel-like channel with periodic or symmetry lateral walls

and a rough floor. The driver region is usually a quite long domain in order to obtain a stable and developed boundary layer on a plane near the outlet. The "real" simulation can then be attached to the driver region and solved together, or the velocity and pressure field in one plane normal to the streamwise direction and close to the outlet can be stored at each time step; the sequence of planes is then read-in as inflow data for a separate calculation. This latter method allows to run two smaller simulation instead than a larger one and can be useful when the precursor database is used for several "following" simulations as it allow to solve the driver region only once. If this is not the case, however, the storing and reading operations can increase the cost of calculation, both in terms of CPU time and data-storage requirement.

The main advantage of this method is that the generation of a physical flow is achieved by the solver without any artificial model. It can be used to generate both stable or developing flow depending on the length and the geometry of the driver region. These simulations show usually a good agreement with experimental measurement, but the cost of the driver region simulation is usually extremely high.

This method was chosen for this thesis to obtain a incoming flow as similar as possible to the real Wind Tunnel tests. The consequences of this choice will be discussed in the present chapter, covering both advantages and disadvantages and the main problem arisen.

5.2 Solver and boundary conditions

The simulations has been carried out using a transient *incompressible solver* i.e. considering the air density constant. The first solver that has been tested is the PISO (Pressure Implicit with Splitting of Operators) scheme. The PISO scheme involves one predictor step and two corrector steps and may be seen as an extension of the SIMPLE scheme, with a further corrector step to enhance it.

While a detailed description of the PISO algorithm can be found on Versteeg (2007), it is interesting to point out a couple of facts.

The first important thing to keep in mind is how the continuity equation

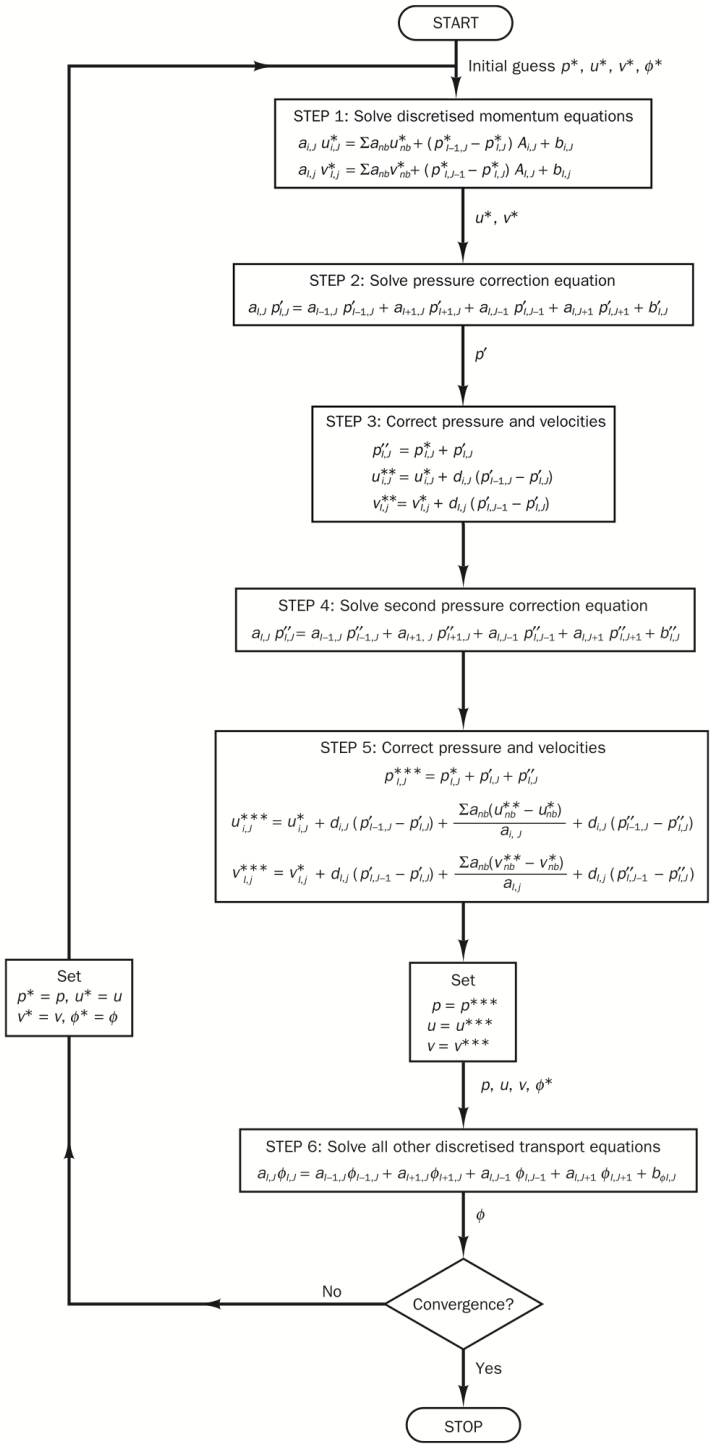

Figure 5.3: The PISO scheme flow-chart (Figure from Versteeg (2007) re-elaborated by the author)

is solved. How we have seen in chapter 3.1.3, the conservation of the mass in an incompressible fluid can be simply represented by the equation

$$\operatorname{div} \mathbf{u} = 0 \tag{5.1}$$

In the PISO (but also in the SIMPLE) algorithm however the velocity field is computed using an approximate version of the momentum equation where the pressure term used is the pressure at the previous iteration. The continuity equation is solved replacing in equation 5.1 the velocity with the pressure, using a relationship obtained from the estimation of the error introduced during the approximation of the momentum equation.

The continuity equation therefore is used to compute a correction to the pressure field to compensate the errors introduced during the calculation of the velocity one. This is the reason why in the solving algorithm doesn't appears any "continuity equation", but instead a *pressure correction equation* shows up. We'll refer to this way to compute the pressure field later when we speak about the digitally generated turbulence.

Another important fact that must kept in mind when using the PISO scheme is the so-called Courant-Friedrichs-Lewy (or CFL) condition. This is a necessary condition for the stability of the solver. Heuristically this condition imposes the time step to be smaller than the time that an hypothetical particle need to travel across a single cell. For one-dimensional case, the CFL has the following form:

$$C = \frac{u\,\Delta t}{\Delta x} \leq C_{max} \tag{5.2}$$

where the dimensionless number C is called *Courant number* and for explicit solvers C_{max} is usually assumed equal to 1. This condition must be true for every cell. For 3D cases the CFL condition is:

$$C = \frac{u\,\Delta t}{\Delta x} + \frac{v\,\Delta t}{\Delta y} + \frac{w\,\Delta t}{\Delta z} \leq C_{max} \tag{5.3}$$

As a corollary, when the grid point separation is reduced, the upper limit for the time step also decreases. Moreover if in a given portion of the domain the velocity is larger, the cells need to be larger or the time step has to be

reduced. This condition can become very strict in those areas where a large velocity gradient occurs. In these areas it's usually required a bigger spatial resolution and thus smaller cells. This leads the maximum Δt to decrease, increasing the number of iteration required and thus the computational time needed to solve the problem.

This condition can result in a serious increase in the computational cost of a simulation. It is possible to partially workaround these limitation using a more stable solver. In section 5.6.2 we will benchmark the PIMPLE solver. The PIMPLE (PI (SO) - (SI) MPLE) solver is an enhancement of the PISO solver that uses SIMPLE sub-iterations to stabilize the algorithm and allow Courant bigger than 1 without diverging. It's important to point out that the PIMPLE solver with one sub-iteration (in OpenFOAM these are called *outer correctors*) it's equal to the PISO solver.

Boundary conditions

The choice of correct boundary condition is crucial to obtain good results. We already discussed in section 5.1 about the inlet condition and the method that can be used to define it. Here we will briefly present the other boundary conditions used in this work.

The main boundary conditions that will be used are:

- fixed value
- zero gradient
- no slip
- free slip (or symmetry plane)

The *fixed value* BC is the simplest to be understood. It simply forces the value of a certain variable to be equal to a given one. Mathematically speaking, this is a Dirichlet boundary condition that is:

$$\phi = \alpha(\mathbf{x}) \tag{5.4}$$

where $\alpha(\mathbf{x})$ is a given value that does or does not vary on the boundary surface. This one is often used as BC for the inlet, where the velocity is given (constant or not), and for the outlet, where the pressure is set equal to zero.

A small remarks has to be given about the pressure value: while giving the inlet velocity is clearly a way to impose a certain inflow discharge, some doubt could arise about the fixed pressure value at the outlet. During experiments we don't care for the pressure value at the inlet nor at the outlet. When the wind tunnel is turned off the pressure inside the wind tunnel is everywhere equal to the atmospheric pressure (neglecting thermal or other small differences). When the wind tunnel is turned on, if we consider a closed circuit wind tunnel, the discharge in all the sections of the wind tunnel must be equal; what makes the air to flow is a positive pressure gradient that arises through the fans. This causes a negative pressure gradient to arise in the wind tunnel that makes the air to start flowing. In the CFD simulations we cannot simply impose a pressure gradient; indeed if we did it, the pressure would be free to shift up and down, keeping the gradient unchanged and therefore the solution consistent. These oscillations are however completely non-physical. To avoid this behaviour the pressure has to be fixed at least in one point. During the post-processing we will compute a *reference pressure* at the test section and we will analyse the *differential pressure*, just the same way the atmospheric constant pressure is neglected during the wind tunnel experiments.

The second BC is the *zero-gradient* BC. Physically this BC is equal to say that the flow is completely developed and that no more changes occur in the direction parallel to the flow. Mathematically this is a Neumann boundary condition, that is:

$$\frac{\partial \phi}{\partial \mathbf{n}} = 0 \tag{5.5}$$

where $\mathbf{n}$ is the normal vector to the boundary surface. In the case that ϕ is a vector quantity the condition is

$$\frac{\partial (\phi \times \mathbf{n})}{\partial \mathbf{n}} = \frac{\partial \phi_n}{\partial \mathbf{n}} = 0 \tag{5.6}$$

that is to ask for the normal component of the quantity to be completely developed.

This BC is true when it refers to the mean value of a completely developed flow. Since the turbulence component of the flow quantities keeps changing inside the eddies, this is not physically correct. Moreover if the flow is not completely stable and developed, this BC is not even true for the mean value. However this is the weakest BC that we can impose to the problem and is a forced choice. To avoid errors in the upwind flow, the outlet is usually placed few meters after the sampled area. We will see this solution in the PoliMi Wind Tunnel simulation where the simulated wind tunnel is much longer than the real version exactly for this reason.

The next BC used is the *no slip* boundary condition. This BC is not a mathematical BC, but more a "set" of boundary conditions that represent a physical behaviour. The no slip BC represents the behaviour of fluids to adhere to surfaces by creating a thin layer of fluid that is not moving relative to the surface. Mathematically this BC is equal to:

$$\begin{cases} \mathbf{u} = \mathbf{0} \\ \partial p / \partial \mathbf{n} = 0 \end{cases} \tag{5.7}$$

In other worlds it's equal to a constant zero value for the velocity field and a zero gradient for the pressure.

The last BC is the *free slip* boundary condition. As the no slip condition, also this BC doesn't not represent a mathematical behaviour, but more a physical one. Physically this BC represent a plane where the flow is free to slip. This never happens in nature since a material that offers zero resistance to the flow doesn't exists, but can be used for some "ideal" surfaces, such as the symmetry planes (for this reason, this BC is also called *symmetry plane*). Mathematically this BC is equal to:

$$\begin{cases} \mathbf{u} \times \mathbf{n} = 0 \\ \partial(\mathbf{u} \times \mathbf{t}) / \partial \mathbf{n} = 0 \\ \partial p / \partial \mathbf{n} = 0 \end{cases} \tag{5.8}$$

where n is the vector normal to the boundary surface and t a vector tangent to it. This is to say that the normal component of the velocity must be equal to zero, while the tangent velocity and the pressure have zero gradient. This is exactly what happens on the symmetry planes. This is also used to bound the domain without a difficult to solve BC in the areas where the exact flow is not important, such as the roof of the wind tunnel or its sides.

5.3 Preliminary benchmark

The PISO solver has been benchmarked on the results obtained by professor Masaru Yoshikawa. Professor Yoshikawa successfully reproduced the flow inside the wind tunnel of the Tokyo Institute of Technology using a CFD commercial software with an LES turbulence model.

This case has been chosen as benchmark for several reasons. The first reason is that we already had the results of this geometry solved with a CFD software (as opposed to the Milan wind tunnel) and we could compare our results not only with an experimental output, but also with a numerical one. The second reason is that this wind tunnel is significantly smaller that the PoliMi one, with a total volume approximately equal to $150m^3$ (Milan Wind Tunnel has a total volume slightly larger than $2000m^3$). In addition to a smaller total volume, the roughness on the floor of the TITech Wind Tunnel had been simulated using cubes. This kind of roughness is much easier to mesh than the closely packed pyramids used in Milan.

The geometry of the benchmark case can be seen in figure 5.4. The wind tunnel consists of a $26m$ long room with a cross section equal to $2.4m$ by $2.4m$. Three spires, approximately $2m$ tall, are placed $1m$ after the inlet. The ground roughness is then generated using two sets of square-based boxes: a set of boxes $40cm$ wide and $15cm$ tall on most of the floor; and a set of smaller boxes, $20cm$ wide and $7.5cm$ tall, on the last $4m$ of the floor before the sampling point.

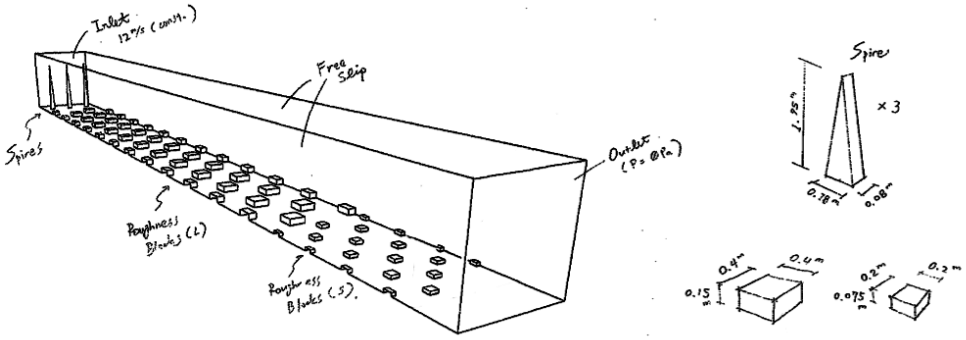

Figure 5.4: Tokyo Institute of Technology Wind Tunnel (image courtesy of M.Yoshikawa)

Mesh

The mesh has been done in agreement with the one used by Yoshikawa in his simulation. The main difference between the mesh used by Yoshikawa and the one used in this simulation lays in the shape of the cells: while Yoshikawa used an unstructured grid of tetrahedral cells, in this simulation a semi-structures grid made of hexahedral cells was adopted. The cells size used can be seen in figure 5.5. The background was formed by $10cm$ large elements. The size is reduced to $5cm$ in a portion of the domain close to the ground and to the spires. Then the elements has been refined one more time to $2.5cm$ on the roughness and the spires surface.

The mesh has been generated using the *snappyHexMesh* utility included in the OpenFOAM suite. A detail of the mesh is shown in figure 5.6. On each surface three layers of $3mm$ thick cells has been added to better resolve the boundary layer.

Boundary conditions

The following boundary conditions has been used to solve the case:

- fixed constant value velocity and zero-gradient pressure at the inlet;
- fixed zero value pressure and zero-gradient velocity at the outlet;
- no slip condition on the floor;
- free slip condition on the side and on the roof;

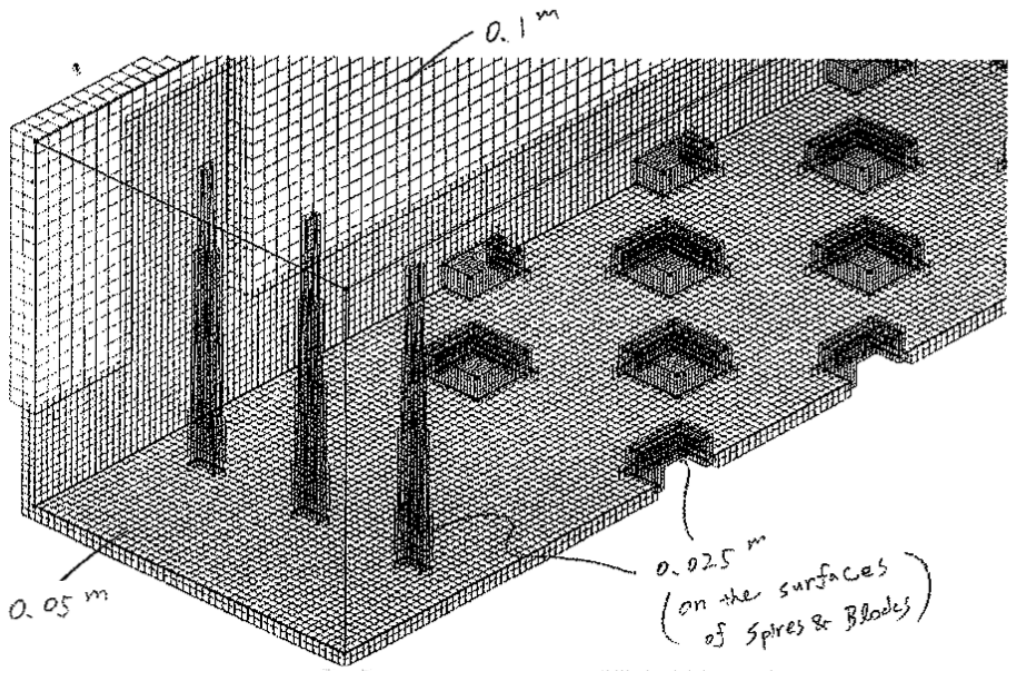

Figure 5.5: Cells size of the Yoshikawa's simulation

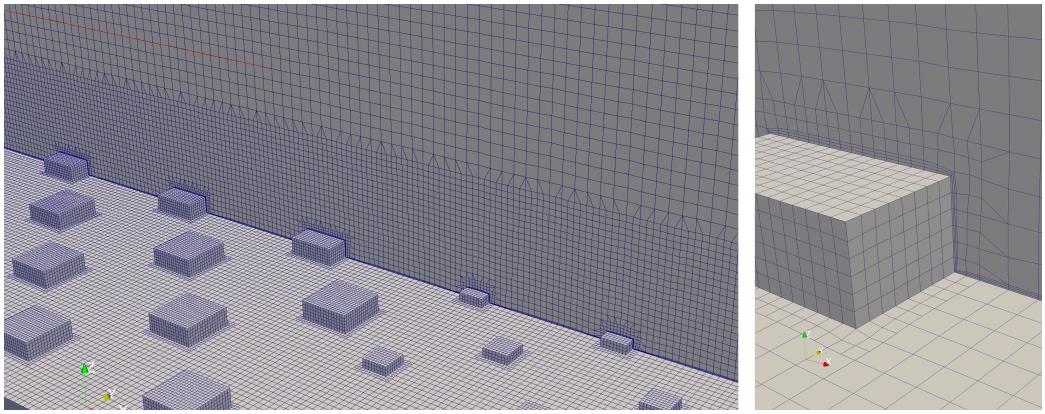

Figure 5.6: A detail of the mesh used

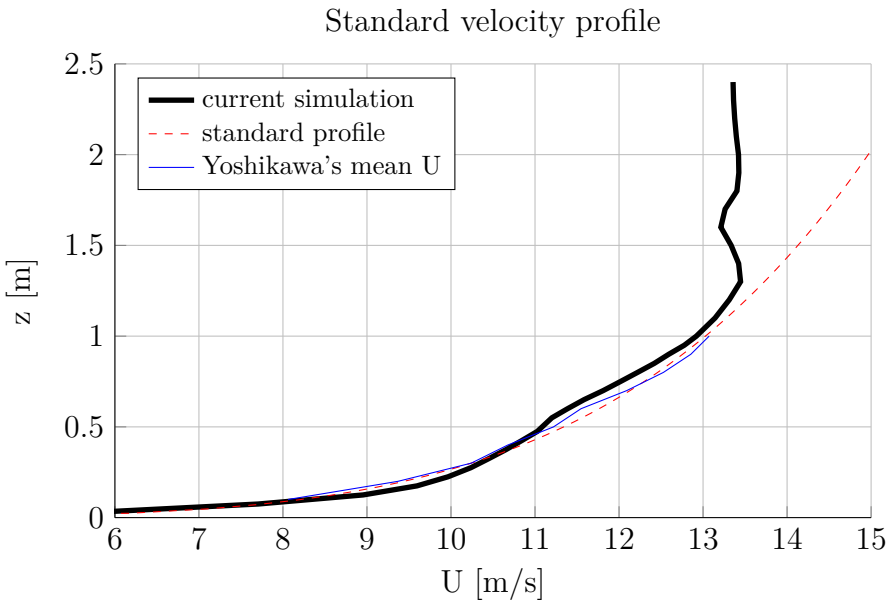

Figure 5.7: Mean velocity profile compared to Yoshikawa simulation and Eurocode profile

Results

The flow has been measured in 850 points divided in 25 vertical lines (from now on called *traversing*). The traversing has been organized both along the streamwise direction and the span-wise direction to analyse the flow evolution along both x and y.

In figure 5.7 we compare the simulated profile with the one simulated by Yoshikawa and with the Eurocode standard log-law profile. The figure is quite self-explanatory: the three profiles shows a very good agreement demonstrating the simulation to be correct.

Comparing the current simulation profile with the Eurocode one above $1m$, one can see that the simulated profile doesn't grows as the Eurocode hypothesizes. Unfortunately a comparison with Yoshikawa simulation and/or TITech wind tunnel cannot be done, as the data above $1m$ are not available. A possible explanation is that the wind tunnel is too short to create a stable profile and this affects the flow above that height.

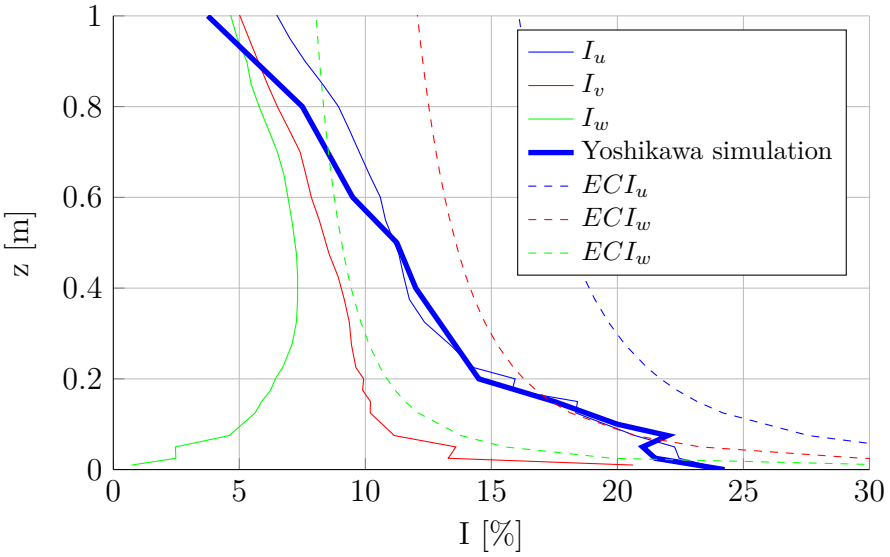

Figure 5.8: Turbulence intensity profile compared to Yoshikawa simulation and Eurocode profile

The last comparison we make with the Yoshikawa simulation regards the turbulence intensity. In figure 5.8 the three simulated turbulence intensity - thin solid lines - are compared with the Eurocode Turbulence intensity (equation 2.14) - dashed lines - and with the Yoshikawa simulation - thick solid line. It appears that the simulation's turbulence intensity agrees with the one simulated by Yoshikawa. These however are both $1.6 \div 2$ times lower than the one expected by the Eurocode. Since Yoshikawa simulation perfectly match the experimental data, the most obvious explanation is that this difference is due to a wind tunnel set-up that is able to reproduce the mean profile, but that cause a turbulence intensity profile different from the one proposed by the Eurocode.

Conclusions

From the comparison with the data obtained in the TITech wind tunnel and with a simulation done with a commercial software, it appears that **the solver chosen and the set-up used are suitable for the solution**

of this type of problems. The geometry provided does not correctly reproduce the wind profile prescribed by the Eurocode nor numerically, nor experimentally. Since Rocchi et al. (2011) demonstrated that the incoming turbulence strongly affect the peak distribution on the building surface, this geometric set-up is not suitable for our research, even if it provides good mean velocity profiles.

5.4 PIMPLE solver benchmark and time-step optimisation

Parallel to the PISO solver, we decided to check if the PIMPLE solver was a feasible solution to reduce the computational time required without affecting too much the solution. This solver indeed allow to use larger time step, reducing the total number of iterations required and thus overcoming the limitations imposed by the PIMPLE solver.

To see the impact of the number of sub-iterations and the Courant on the flow and study possible numerical-diffusion effects, we run a simple geometry benchmark using different Δt and `nOuterCorrector` (from hereafter N_{OC}). In table 5.1 and 5.2 the Courant number (maximum over the whole simulation and average time-step maximum) and the average time per time-step obtained with these simulations are summarised.

For $\Delta t \geq 0.002s$, however, severe numerical diffusion appeared. The best solutions with a good execution time reduction and an acceptable numerical diffusion are $\Delta t = 0.001s$ and N_{OC} equal to 2 and 5. To have a better knowledge of the impact of this choice on the flow, a more detailed benchmark has been then carried out using again the Yoshikawa's benchmark.

In figure 5.9 we compare the mean velocity profile obtained with the PISO solver (the same plotted in figure 5.7) to the two profiles obtained with 2 and 5 outer correctors. The profile is almost identical showing little or no difference at all.

Looking the turbulence intensity in figure 5.10 the result is still good and the profiles show a good degree of agreement. However few differences start

Table 5.1: PISO and PIMPLE execution time benchmark (part 1)

	nOuterCorrector			
	1 (PISO)	2	5	10
dt=0.0001				
maxCo	-			
mean maxCo	-			
mean iter time:	1.13609			
time for 60s	681654			
dt=0.0002				
maxCo		1.3975		
mean maxCo		1.0793		
mean iter time:		2.0085		
time gain		11.60%		
dt=0.0003				
maxCo		2.0835		
mean maxCo		1.6389		
mean iter time:		2.1045		
time gain		38.25%		
dt=0.0004				
maxCo		2.7411		
mean maxCo		2.1898		
mean iter time:		2.3071		
time gain		49.23%		
dt=0.0005				
maxCo		3.4688	3.5899	
mean maxCo		2.7181	2.7658	
mean iter time:		2.4599	3.6712	
time gain		56.70%	35.37%	
dt=0.001				
maxCo		6.6494	6.7977	
mean maxCo		5.3862	5.3531	
mean iter time:		3.1207	5.7762	
time gain		72.53%	49.16%	
dt=0.002				
maxCo		13.0819	12.7592	13.2431
mean maxCo		10.7296	10.4109	10.396
mean iter time:		3.5076	8.7334	14.5948
time gain		84.56%	61.56%	35.77%
dt=0.004				
maxCo		26.23	23.5578	27.9573
mean maxCo		21.46	20.6794	20.0538
mean iter time:		3.5	8.2765	13.7686
time gain		92.30%	81.79%	69.70%

Table 5.2: PISO and PIMPLE execution time benchmark (part 2)

	nOuterCorrector		
	1 (piso)	2	5	10
dt=0.005				
maxCo			31.1665	28.4032
mean maxCo			26.1783	25.1399
mean iter time:			8.4274	12.843
time gain			85.16%	77.39%
dt=0.01				
maxCo			67.1	61.6586
mean maxCo			53.43	49.7343
mean iter time:			7.76	16.9393
time gain			93.17%	85.09%

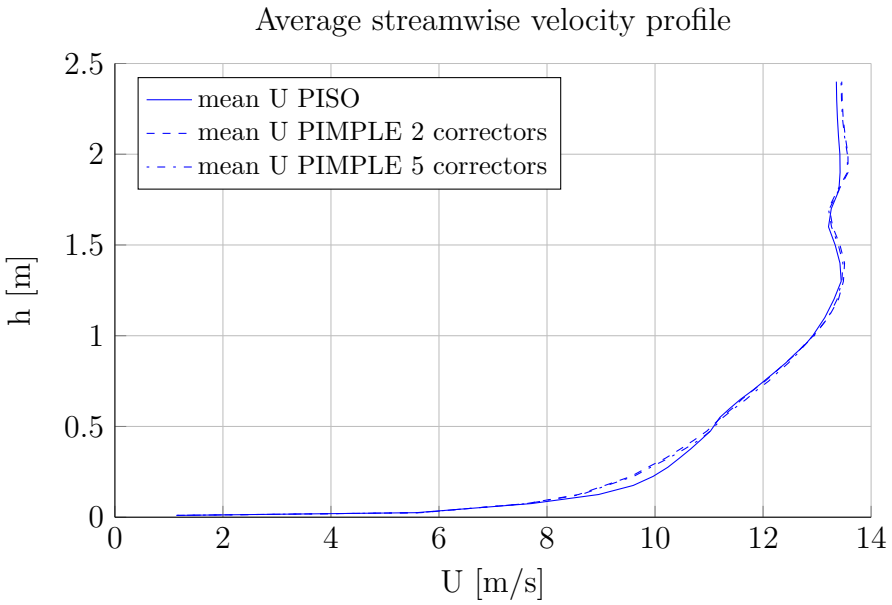

Figure 5.9: Turbulence mean velocity profile

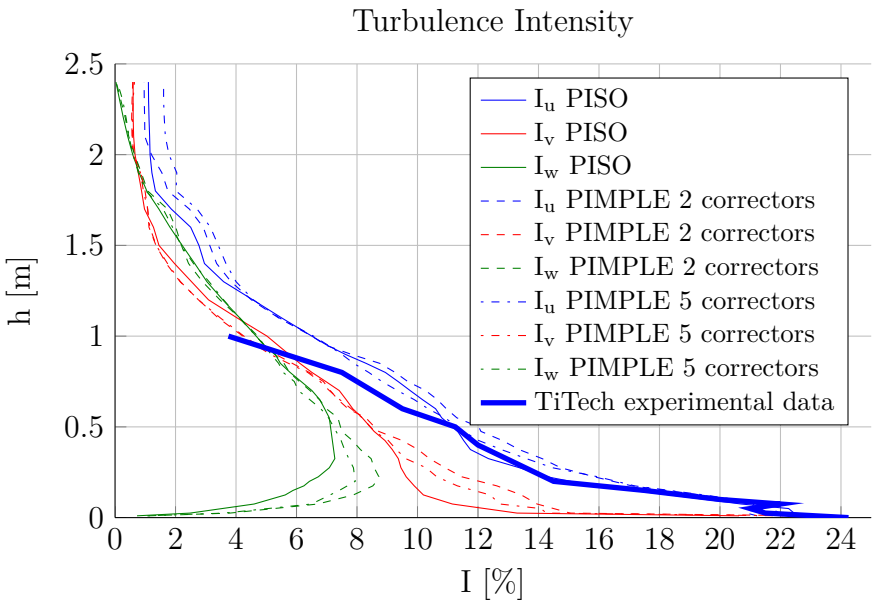

Figure 5.10: PISO - PIMPLE comparison: turbulence intensity profile

to arise. The streamwise turbulence intensity obtained with the PIMPLE solver matches quite well with the PISO one. Lateral and vertical turbulence intensity seams to be a little higher, with the simulation with 2 correctors giving a closer result to PISO than the one with 5 corrector.

Figure 5.11 shows how the two spectra obtained with the PIMPLE solver has an higher energy content in the range $f^* = 0.5 \div 2$.

From this comparison appears how the PIMPLE solver with 5 sub-iterations doesn't shows considerable advantages compared to the PIMPLE solver with 2 sub-iterations. At the same time the differences between PISO and PIMPLE solvers are acceptable, especially if we remember that the PIMPLE solver reduce the time required for the simulation of 72.5%.

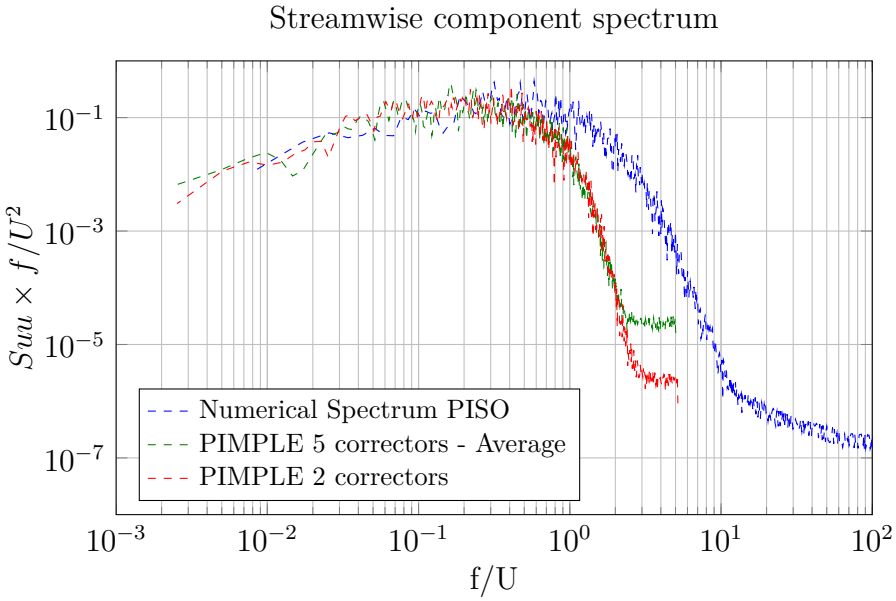

Figure 5.11: PISO - PIMPLE comparison: streamwise spectrum

5.5 Sensitivity of ABL to Wind Tunnel elements

The boundary layer obtained inside the wind tunnel is caused by the superposition and the interaction of the effects of the spires and of the ground roughness. There are also other factors affecting the flow that mainly influence the velocity distribution across the inlet plane. These are the distribution of the engines, the heat exchanger grid, the mast of the turning wings and other elements of the wind tunnel. In our simulation we considered the inbound flow constant in time and space. This hypothesis should be further analysed as it's impact on the resulting profile. This won't be done in this thesis, however.

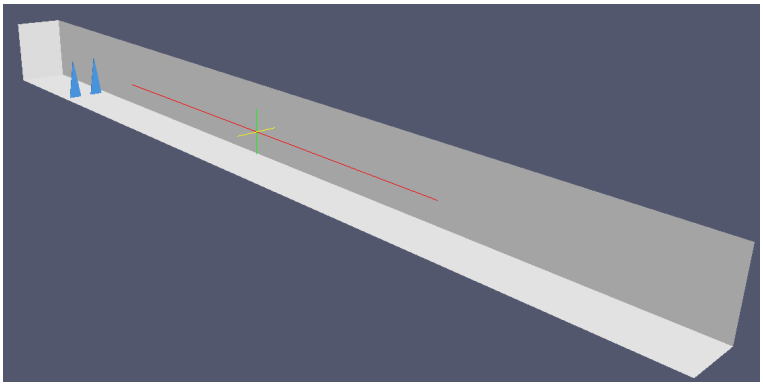

Figure 5.12: Simulation domain for the spires test

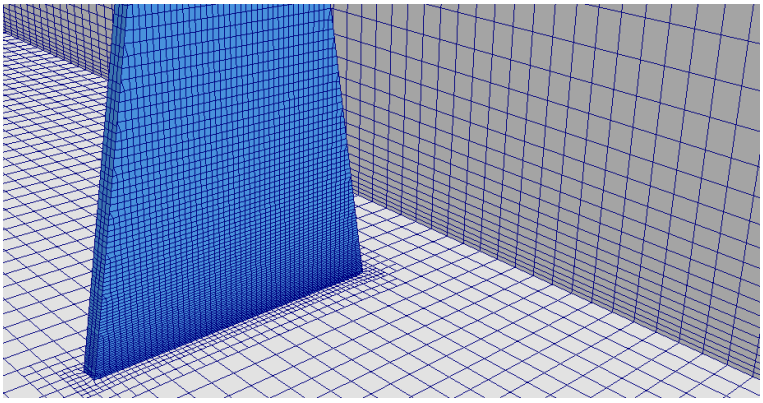

Figure 5.13: Detail of the simulation's mesh for the spires test

5.5.1 Spires

The first element that has been tested are the spires placed at the beginning of the wind tunnel. The simulation reproduces 2 spires inside a $50m$ long, $3m$ wide and $4m$ tall channel. Contrary to what has been done before, the wall boundary condition is used both on the floor and the ceiling. The length of the domain has been chosen in such a way that the distance between the spires and the measurement point is the same in the simulation and in the wind tunnel. The simulation domain has to be a little larger than the wind tunnel, however, to avoid inlet and outlet to be too close to the spires or the probes and possibly alter the flow.

The comparison with the wind tunnel data is given in figure 5.14 and 5.15. The normalised mean velocity profiles show a very good agreement with the

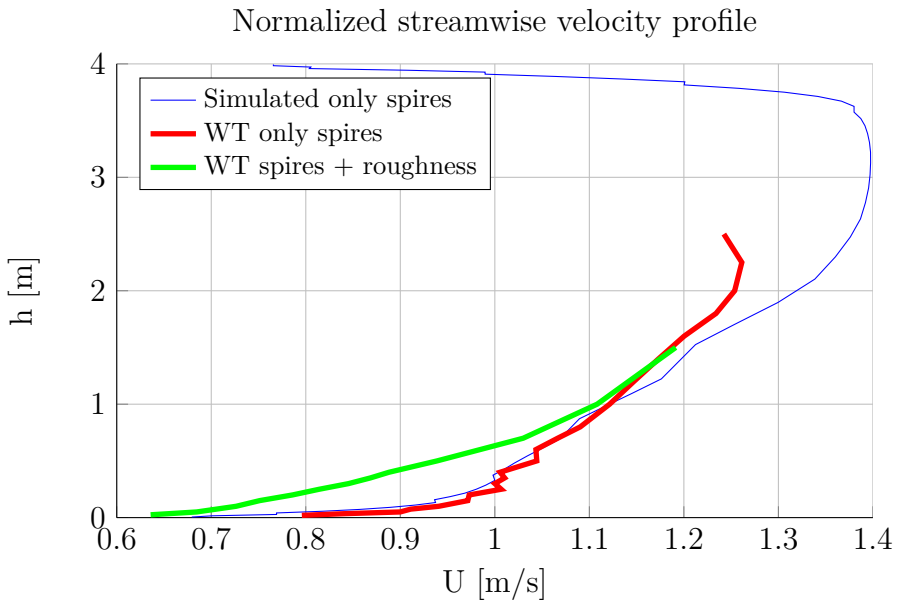

Figure 5.14: Mean velocity profile with spires only and spires+roughness for comparison

experimental data. The green line representing the profile obtained with both spires and ground roughness highlights how the spires are responsible for the upper part of the mean velocity profile, while the ground roughness is responsible for the lower.

The turbulence intensity in the simulation however is about 2% higher than the one measured inside the wind tunnel. This reason for this behaviour could be found in the solver used. This is indeed similar to what we observed in section 5.6.2 with the Yoshikawa's simulation where using the PIMPLE solver in place of the PISO solver cause the turbulence intensity to grow.

5.5.2 Ground roughness

The second element to be tested is the ground roughness. This is also the hardest to correctly simulate due to the complex geometry and the need to catch the flow on the narrow spaces *between* the pyramids.

The roughness in this wind tunnel is not simulated with blocks, as it

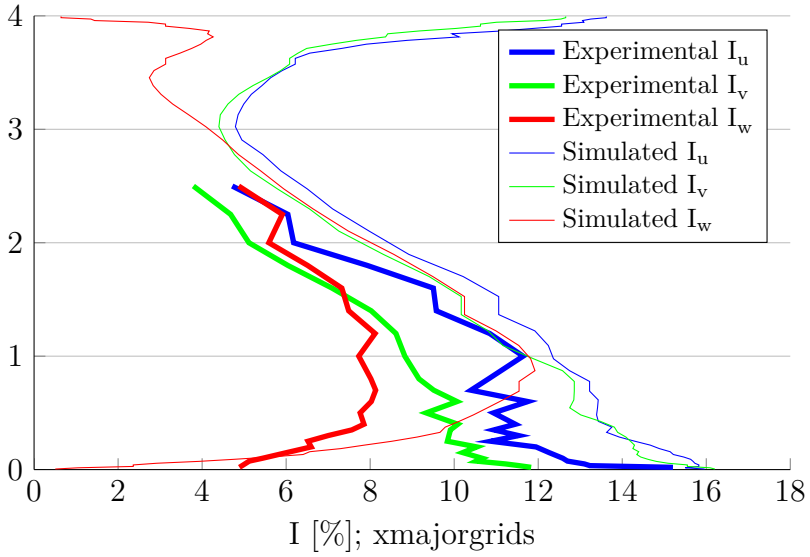

Figure 5.15: Turbulence intensity profile with spires only

was in the TITech wind tunnel, but with smaller and closer pyramids. The pyramids has been chosen for operational reasons: having them disposed on large panels allows a faster preparation of the Wind Tunnel compared with the blocks that have to be placed one by one.

This kind of roughness proved to be the most difficult element to reproduce: their non-vertical faces cause the cell's faces to be non-orthogonal causing severe numerical diffusion problems. Also, their closely packed distribution cause the meshing tool to create very skewed cells. A third problem is that to correctly catch the flow passing between them, a large number of cells need to be used.

To better understand the source of these problem, one need to remember the kind of meshing utility used: *Snappy Hex Mesh*. This meshing tool belongs to the *cut-cells* kind. This means that the mesh is generated starting from a volumetric mesh made of perfectly orthogonal cells. The utility then *whittled* inside the mesh the desired geometry through several passages (referring to figure 5.17): 1) background mesh 2) refinement 3) castellated mesh 4) snapping). An important observation is that the mesh, until the snapping

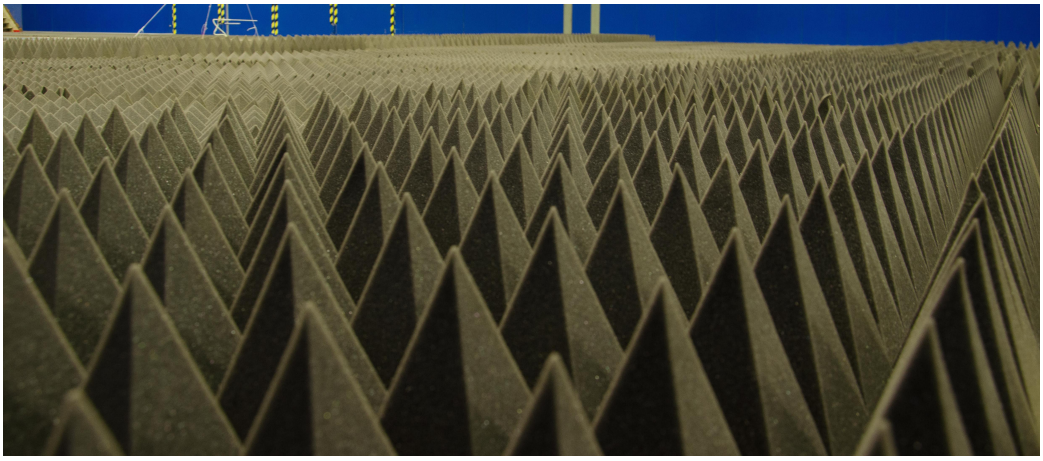

Figure 5.16: Floor roughness used inside the wind tunnel

passage, is still completely orthogonal. This property will be exploited in the creation of the mesh.

To find the better setup for the simulation of the roughness, we ran the simulation of a $100m$ long, $20cm$ wide and $2m$ tall channel. The boundary condition on the lateral and the upper walls have been set as *symmetry plane*, while on the floor has been used a *wall function* boundary condition. The pyramids were positioned on the floor of the domain. Several set-ups of the pyramids and snapping techniques have been tested in order to find the best solution. The set-up tested are:

- **dense snapped**: all the pyramids are reproduced and the cells are snapped to the pyramids surface
- **dense not snapped**: all the pyramids are reproduced, but the cells are not snapped. This leads to stepped pyramids instead of slanting sides. The advantage of this mesh is that it's almost completely orthogonal, minimizing the numerical diffusion effects.
- **coarse snapped**: half of the pyramids are removed obtaining a chess-board-like distribution. This helps reducing the crowdedness and reduce the meshing problems
- **coarse not snapped**: half of the pyramids are removed and the cells

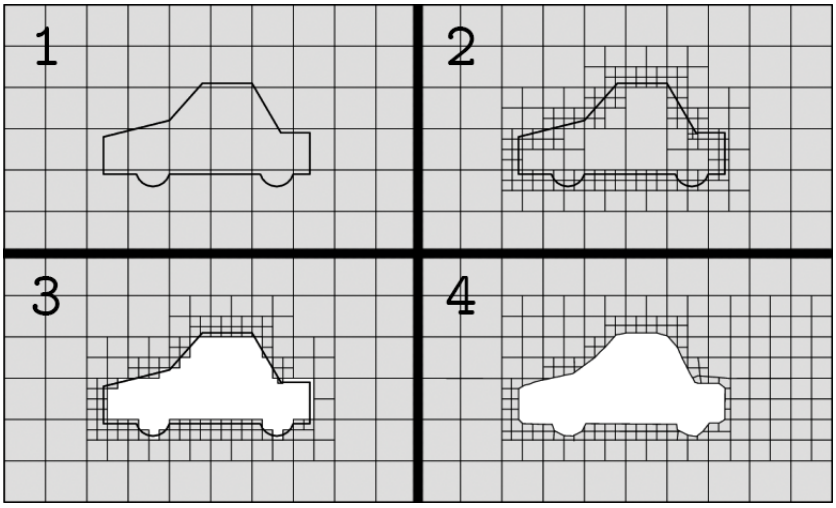

Figure 5.17: Some of the *Snappy Hex Mesh* steps

are not snapped. The same considerations of the "dense not snapped" mesh applies here too.

Despite several tries, snappyHexMesh could not converge in the *dense snapped* set-up. This is due to the problems said above. The other three set-ups, instead, successfully converged.

In figure 5.18 the normalised mean velocity profile obtained with the three meshes are compared to the one obtained inside the wind tunnel . Since a profile inside the wind tunnel obtained only with the roughness wasn't available, the profiles are compared with the profile in figure 4.4. The expectation was to catch the lower part of the profile that is most influenced by the roughness.

The results demonstrated that the stable boundary layer obtained with these simulation doesn't match with the experimental one. This is due to the fact that the boundary layer inside the wind tunnel is not stable and is affected by the alternating of different roughness heights.

Looking at the mean velocity profile in a logarithmic plot (figure 5.19, appears that the profile fits very well a logarithmic function. This agrees with the equations given by the Eurocode and demonstrate that the obtained ABL is completely developed.

The differences between the three meshes are negligible. For this reason in the following simulations the *dense not snapped* setup has been used being the closer the the real Wind Tunnel setup.

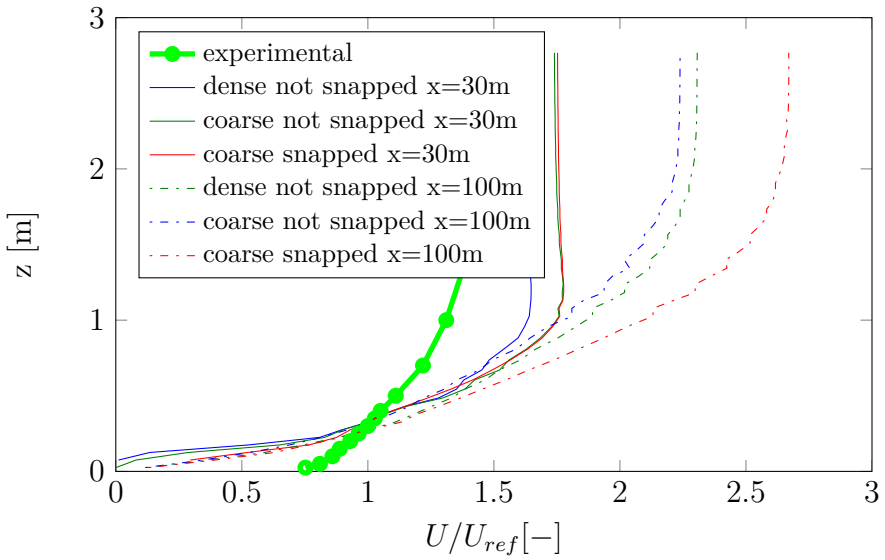

Figure 5.18: Normalised mean velocity profiles 30m and 100m after the inlet compared with the Wind Tunnel profile obtained with spires and roughness

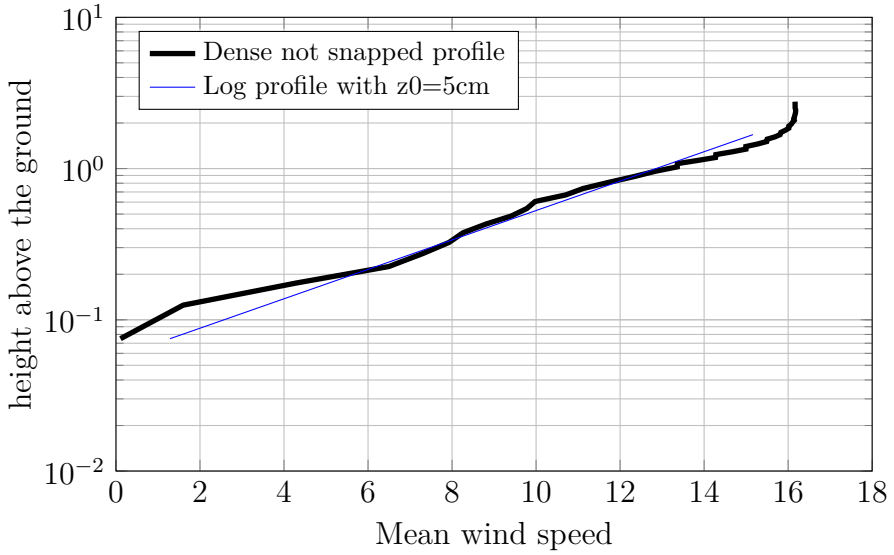

Figure 5.19: Normalised mean velocity profiles of case *dense not snapped* 100m after the inlet

5.6 Empty Wind Tunnel simulation

The following work focused on the reproduction of the Milan wind tunnel. However this simulation proved to be far more complex than the Yoshikawa one and several problems arose. The first one has been the creation of a correct mesh for the case.

5.6.1 Mesh

First of all we present the wind tunnel geometry and which feature we tried to reproduce. In figure 5.20 the map of the wind tunnel is represented. As said before, the size of this wind tunnel is far larger than the Japanese one causing more cells, and thus more computational power, to be required using the same cell size.

Different degrees of refinement have been used in different areas of the mesh (figure 5.21). A $10cm$ background mesh is used in the upper part of the domain. The mesh have been refined twice near the floor, i.e. each cell is divided in 8 sub-cells twice, for a total of 64 cells per original cell after the second refinement. The mesh has been refined one more time near the smallest roughness and close to the (future) position of the building.

In figure 5.22 is a detail of the meshed roughness. It can be clearly seen that the geometry is not correctly reproduced. A better agreement with the wind tunnel geometry could be achieved refining the mesh one more time near the roughness. This is however impossible since there are already 4 millions cells close to the ground roughness. Refining them one more time would split each cell in 8 sub-cells. This would create about 32 millions cells just to solve the roughness, exceeding the available computational power.

5.6.2 Time-step and solver

Once the mesh has been prepared, we ran the case using the same set-up used in the Yoshikawa's simulation. The first thing to point out is that while the previous simulation used 1.7 Millions cells, this simulation is made of more than 19 Millions cells. The computational power required to solve this

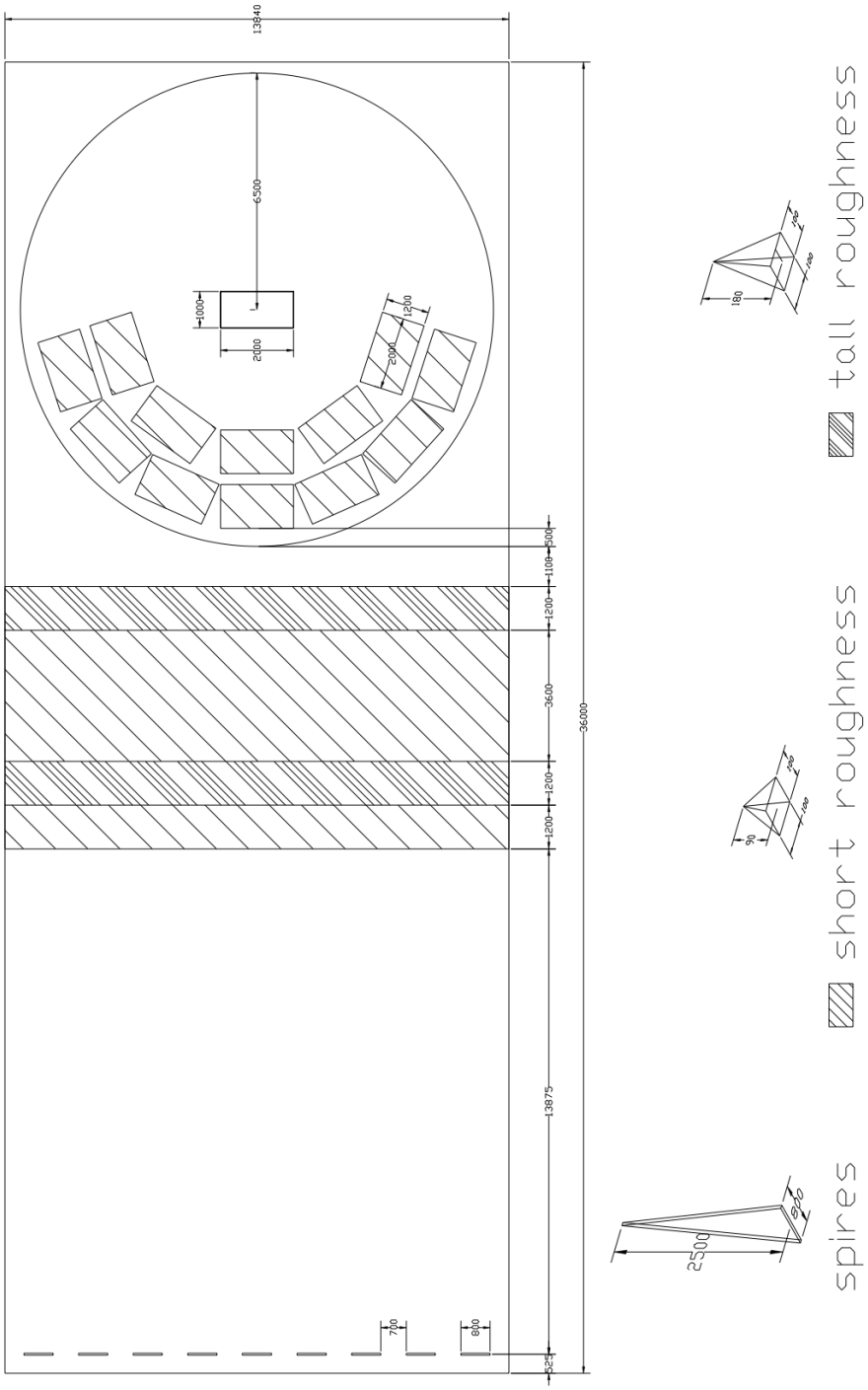

Figure 5.20: Wind tunnel map (Measurements in millimetres)

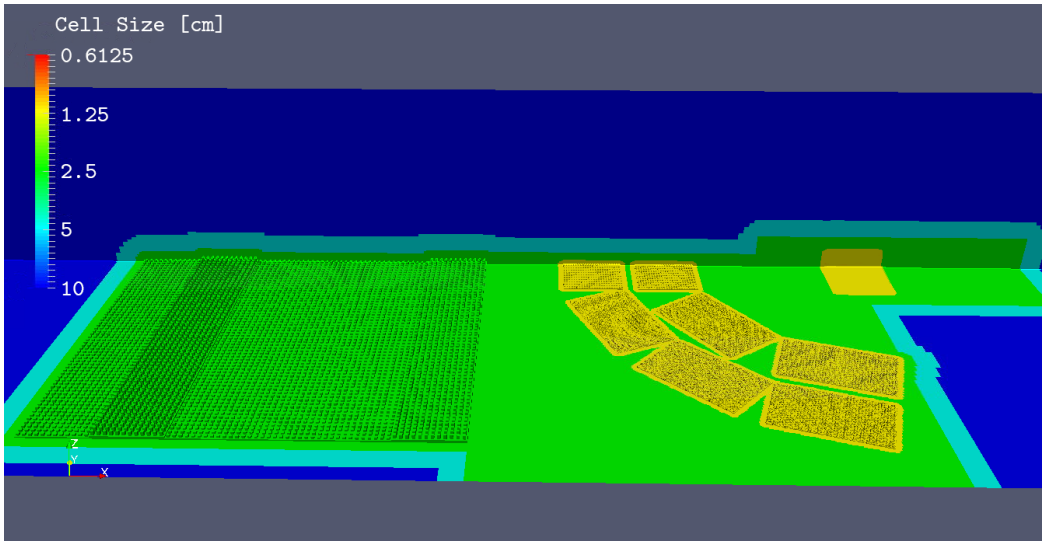

Figure 5.21: Wind tunnel mesh - overview

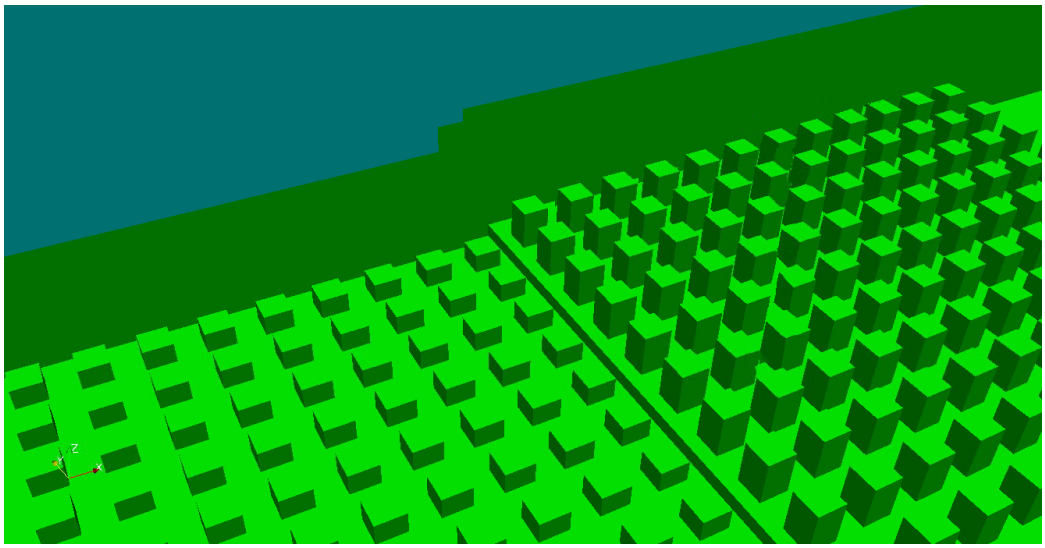

Figure 5.22: Wind tunnel mesh - detail of the roughness. Notice that the pyramids are represented as blocks; this happens because the cells hasn't been snapped to the geometry.

case is more than 10 times larger and is pushing our computational resource to their limit. This situation represented the main problem we faced during the simulations.

The first-try time step had been calculated to be $1/1000s$ using an approximated version of equation 5.2. As we said equation 5.2, has to be true in every cell, therefore for the exact estimation of Co_{max} should be used U and Δx of every single cell. Since this is impossible to know before running the case, a pre-dimensioning of the suitable Δt can be done using U equal to the free-stream velocity and $\Delta x = \Delta x_0/2^N$ where Δx_0 is the background mesh streamwise dimension and N is the maximum refinement level. This calculus doesn't predicts perfectly the Courant number. This happens because the maximum refinement is usually executed near the surface where the speed is lower than the free stream velocity; moreover, if the cells have been snapped their size could be different from $\Delta x_0/2^N$ or they could be not aligned with the flow. In unsteady simulations, like LES, fluctuating variations and guts are difficult to predict. Therefore this formula gives a first idea of the order of magnitude of the time-step, but the ideal value cannot be known before the simulation starts.

When the simulation started we noticed that the estimated time step of $1/1000s$ led to a Courant number equal to $5 \div 6$ with peaks (due to the guts) equal to 7. Since the PISO solver easily diverges when the Courant number is larger than 1, two solutions existed: lower the time step so that the average Courant number was equal to $\approx 0.5 \div 0.6$ or change the solver to a more robust one.

While the first option looks like the most obvious one, it must be noticed that in order to lower the Courant number from 7 to 0.5 the time step should have been reduced to one tenth. Since the time needed to compute each iteration was already close to the minimum obtainable from the CPU, this would have meant to multiply the computation time by 10. This could not be accepted as the estimated time was already about 10-15 days.

To solve this issue we decided to change the solver and use the PIMPLE solver that we benchmarked in section 5.4 with $\Delta t = 0.001s$ and N_{OC} equal to 2.

5.6.3 Results

Once all the Wind Tunnel elements has been benchmarked and that a numerical method has been chosen, the next step of the research was to use all these information to reproduce the flow inside the Wind Tunnel. Before trying to simulate the experiment measuring the pressure on the building, we needed to check that the flow generated by the combination of spires, ground roughness and wall-functions agrees with the ABL measured inside the PoliMi Wind Tunnel.

We have already pointed out in section 5.5.2 how the reproduction of the ground roughness is not yet fully satisfactory and that the profiles obtained does not correctly reproduce the Wind Tunnel profiles. At the time of writing a finer mesh simulation is running. Due to the long time required for this simulation to finish, in this chapter we will present a partial result obtained with the mesh presented in 5.6 that provides fairly satisfying results.

In figure 5.24 the normalised mean velocity profiles appear. The simulated flow is slightly faster than the experimental profile below $z = 0.5m$ and slower above. This behaviour indicate a lower value of z_0, thus a more stiff profile. When compared to the Eurocode profile for the Category II terrain, however, the result is a bit better and the agreement between the two profiles is acceptable.

In figure 5.25 the turbulence intensity profile obtained with the CFD simulation are compared to those obtained inside the Wind Tunnel. The simulated flow is slightly less turbulent in the streamwise above $10cm$, but shows the correct behaviour below that height tending to infinity, while the experimental data doesn't. The lateral and vertical turbulence intensity profiles below $0,5m$ agree very well with the experimental data. We need to remember that above that height the mesh becomes coarser and a lower agreement with the experimental data has to be expected.

Also the integral length profiles shown in figure 5.26 agree sufficiently with the experimental data. They don't present the exponential growth expected by the Eurocode equation 2.19, but we have seen in section 4.4.2 how this behaviour cannot be reproduced neither inside the Wind Tunnel.

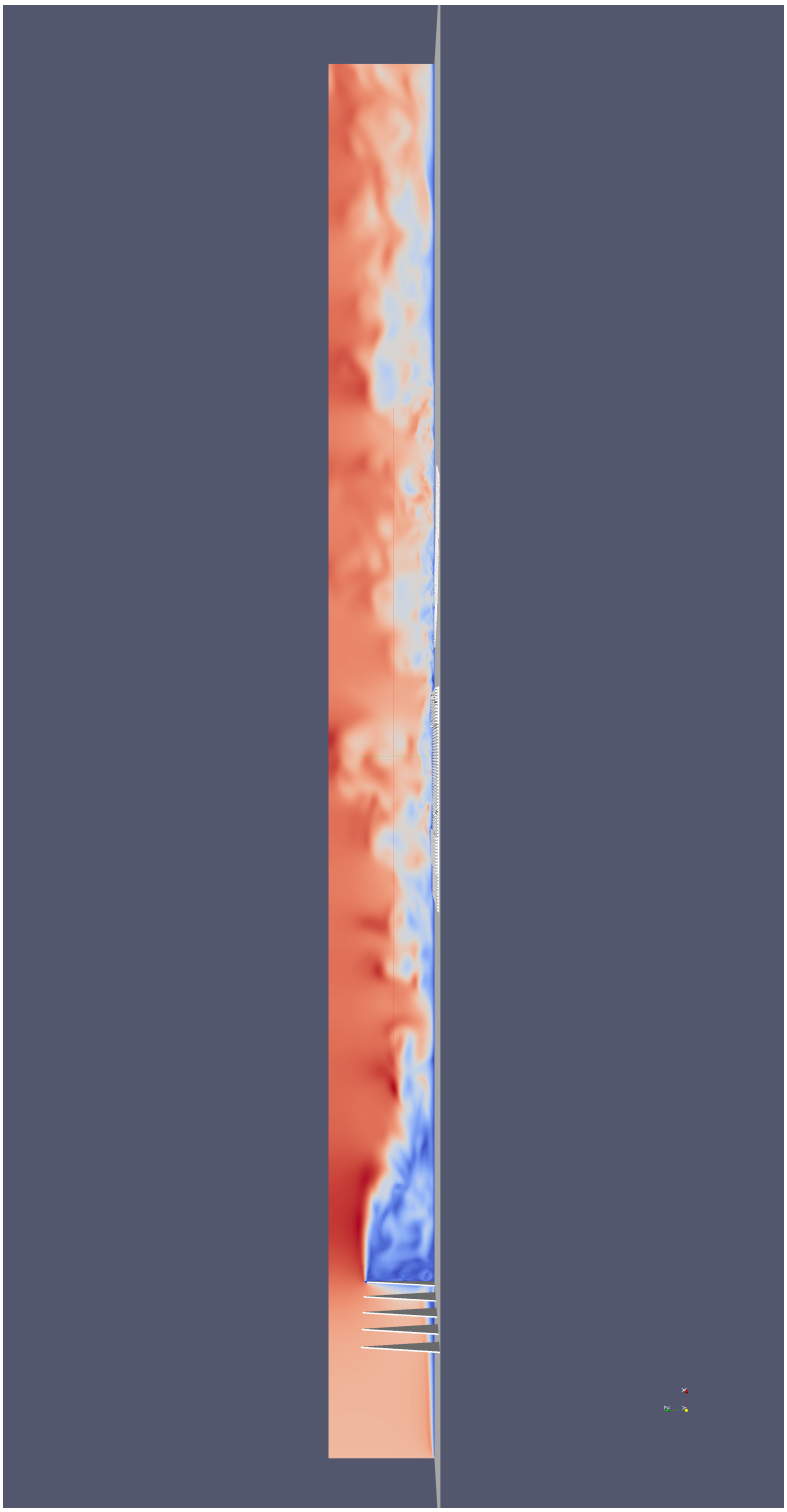

Figure 5.23: Empty wind tunnel simulation - Velocity magnitude

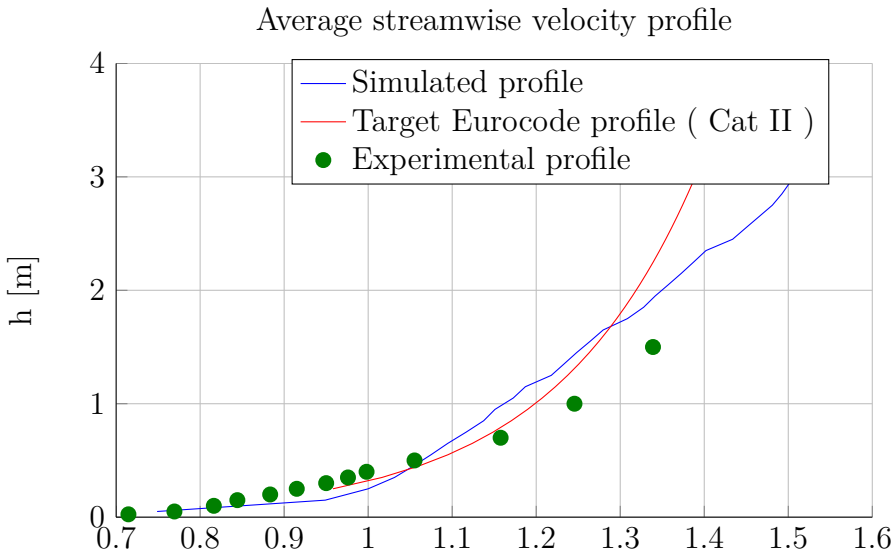

Figure 5.24: Normalised mean velocity profiles inside the empty Wind Tunnel

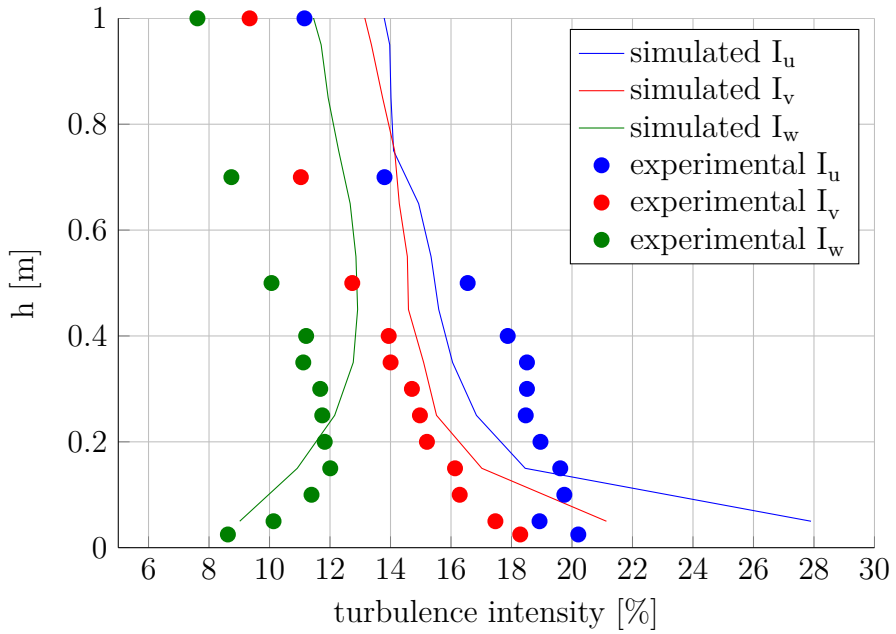

Figure 5.25: Turbulence intensity profiles inside the empty Wind Tunnel

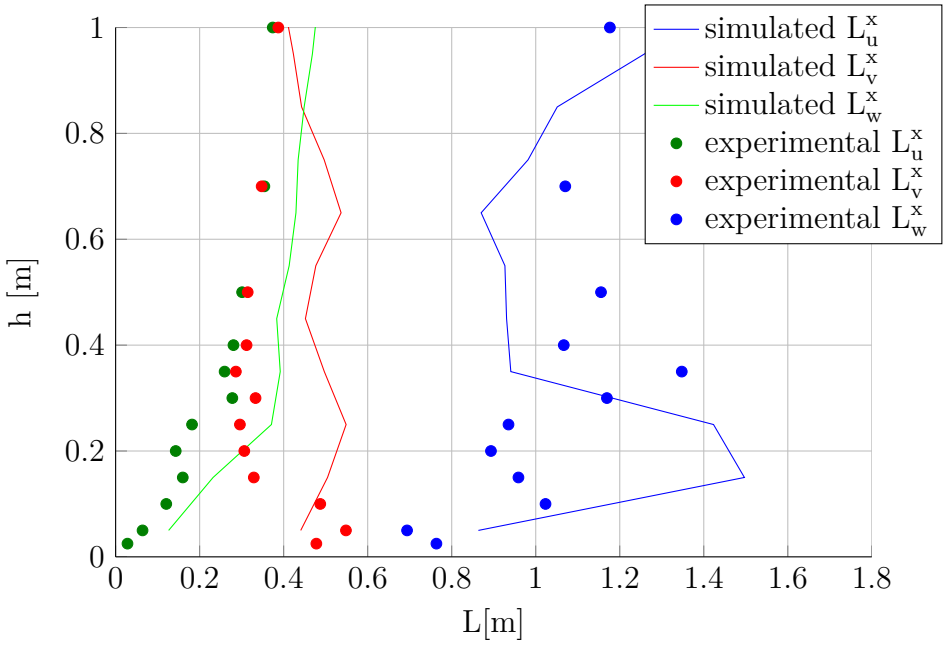

Figure 5.26: Integral length profiles inside the empty Wind Tunnel

Something more about the turbulent structures of the flow can be said observing the streamwise component spectrum acquired at $z = 0.3m$ in figure 5.27. The spectrum has been normalised using the same strategy used for equation 2.22. For $f^* < 2$, that is $f <\approx 20Hz$. The simulated flow spectrum agrees well with both the experimental spectrum and the ones proposed by the Eurocode. Above that frequency the simulated flow spectrum drop rapidly due to the LES cutout filter.

Transforming this frequency into a full-scale wave length we observe that:

$$L_{FS} = \frac{U_{FS}}{f_{FS}} = \frac{U_{FS}}{f_{MS} * \frac{1}{\lambda_t}} =\sim 20m \tag{5.9}$$

where the FS subscript indicate the full-scale values, while the MS indicate the model-scale ones and λ_t is the time-scale parameter indicated in table 4.1. It appears that we are simulating only flow structures larger than $20m$. This value could appear not sufficient to correctly catch the negative peak

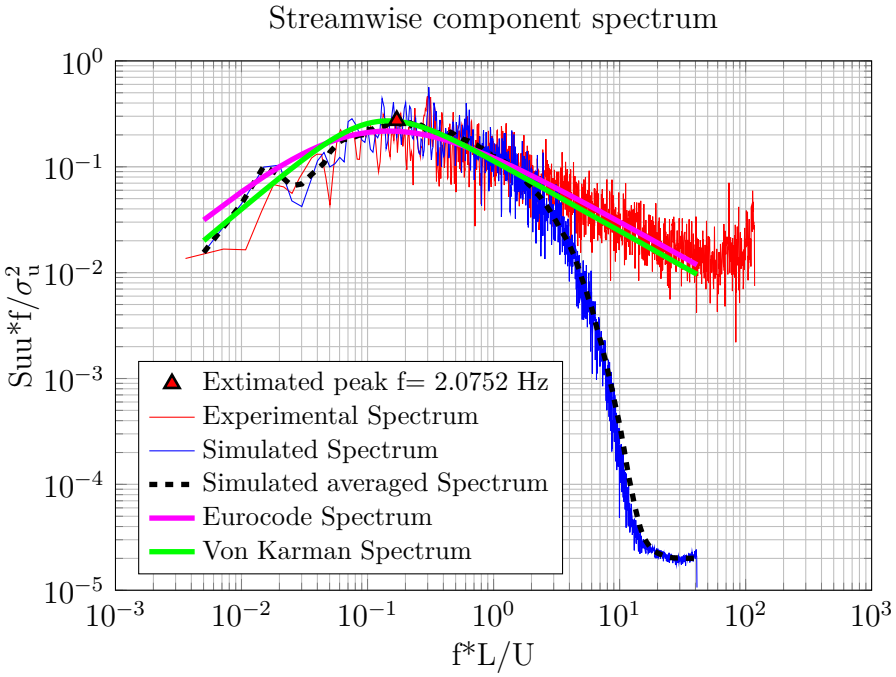

Figure 5.27: Normalised streamwise component spectrum 30cm above the ground

value that we are looking for in the simulation. However it's important to see that the cutout frequency falls inside the inertial sub-range of the spectrum. In this portion of the spectrum, smaller eddies are generated by the decay of larger ones and not by interaction with the boundary. This is important because the "lost" frequency can be recovered just refining the mesh in the area closer to the test section. This would shift the cutout frequency higher and reduce the SGS viscosity, allowing the previously smaller eddies to decay in smaller ones with lower time-scales.

The flow obtained with the CFD simulation represent a good approximation of the wind obtained in the PoliMi Wind Tunnel. The mean speed and the turbulence intensity show some minor problem below $0.2 \div 0.3m$ from the ground. This is most likely due to the poor reproduction of the ground roughness that is the main cause for the turbulence in that area. Even if this could seem a small portion of the domain, we need to remember that the

model we are going to simulate is $30cm$ tall, thus it's completely immersed in flawed portion of the flow. Despite this, the results appears to be satisfying enough to justify a simulation with the hangar using this setup.

5.7 Hangar simulation

The last simulation to be performed is the one of the PoliMi Wind Tunnel with the test building in it. The simulation setup is almost identical to the setup used for the empty Wind Tunnel simulation. The only and main difference between the two case is the presence of the building at the centre of the turning table. The simulation has been executed using 256 CPUs and 924GB of memory for 10 days i.e. more than 61.000 computing hours.

The pressures on the building has been acquired with two different techniques: using the *surface sample* utility the pressure has been measured at the centre of each boundary cell touching the hangar surface, this led to (almost) continuous data with a very high spatial distribution. Using the *probe* utility instead the pressure has been measured in the same points it has been measured during the experiment inside the wind tunnel. This led to a spatially discrete data with an average distance between the measuring points of approximately $5 \div 10cm$. To avoid differences between the experimental results and the CFD ones imputable to the different sampling spatial resolution, the comparison between the two techniques has been carried out using the latter data, even if this resulted in a loss of information.

Since the pressure is set equal to zero at the outlet, the pressure in the Wind Tunnel is almost everywhere larger than zero. The pressure are therefore "cleaned" exactly the same way they are in the Wind Tunnel: the pressure is acquired in six points at the test section on the wind tunnel side walls and ceiling. This pressure is then set as reference static pressure and is subtracted by all the acquired data. In the Wind Tunnel this operation is done pneumatically, while in our simulation is done during the post-processing.

In the following, the results of the simulation and the pressure map acquired are presented.

Comparing the C_p mean value map obtained with the CFD in figure 5.28

with those obtained with the Wind Tunnel simulation in figure 4.12, we can observe that the value obtained with the simulation is about 10-15 % lower on the lateral and rear walls of the building and on the leeward part of the roof. The portion of the roof behind the leading edge of the building instead shows larger error equal to 25-30%.

It's important to point out that the C_p appear to be lower in absolute value everywhere. This is explainable with the faster reference velocity at the roof-height that leads to a larger dynamic reference pressure.

Even if the percentage error of the numerical value is still a bit too high to consider it acceptable, the overall pressure distribution is the one expected for this case, with a higher negative value behind the leading edge, a smaller negative pressure everywhere else except the upwind face with a constant C_p value close to 1.

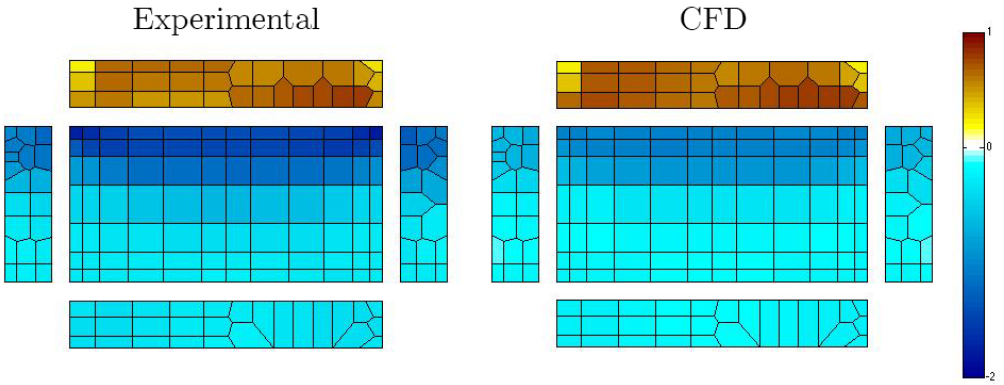

Figure 5.28: Mean C_p

In figure 5.29 we see the standard deviation map plotted using the same color scale used in figure 4.14. It's evident that the standard deviation is everywhere far below the experimental value with a mean error around 50-60%. We will explain this later when looking at the time-histories.

When plotting the standard deviation with a proper scale to highlight the differences (figure 5.30) we see that the distribution on the roof is similar to the one in experimental data.

We already said that the skewness is an important parameter when look-

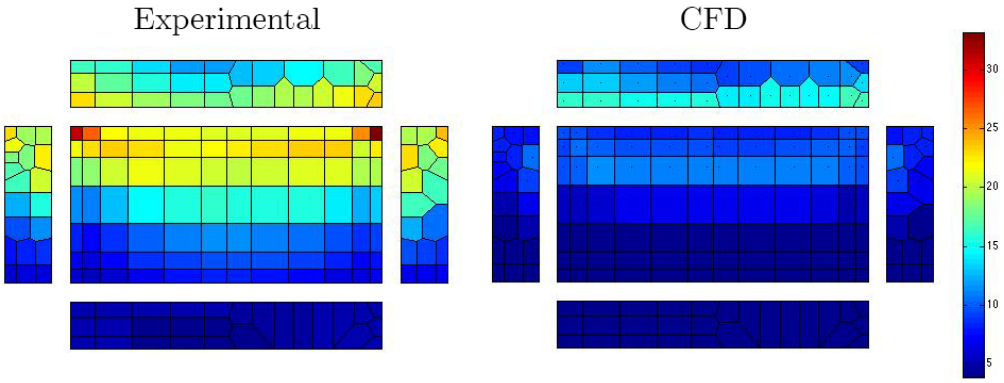

Figure 5.29: C_p Standard deviation

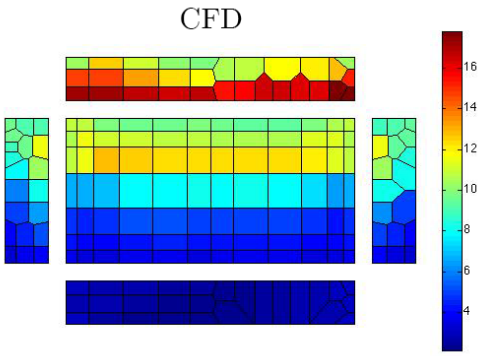

Figure 5.30: C_p Standard deviation (different color scale)

ing at the pressure on a building surface. This happens because the surface pressure where a separation of the boundary layer occurs are highly skewed toward the negative values. To correctly catch the peak pressures it's therefore extremely important for the correct estimation of the skewness too.

In figure 5.31 the skewness distribution on the building is presented . The distribution is everywhere satisfying, except for the same portion of the roof behind the leading edge where also the mean value was flawed.

Finally we can compare the time-histories of two pressure taps at the centre of the roof and behind the leading edge (to be precise, at the roof upwind corner) acquired in the wind tunnel and in the CFD simulation.

The time-history of the tap at centre of the roof shows a behaviour very

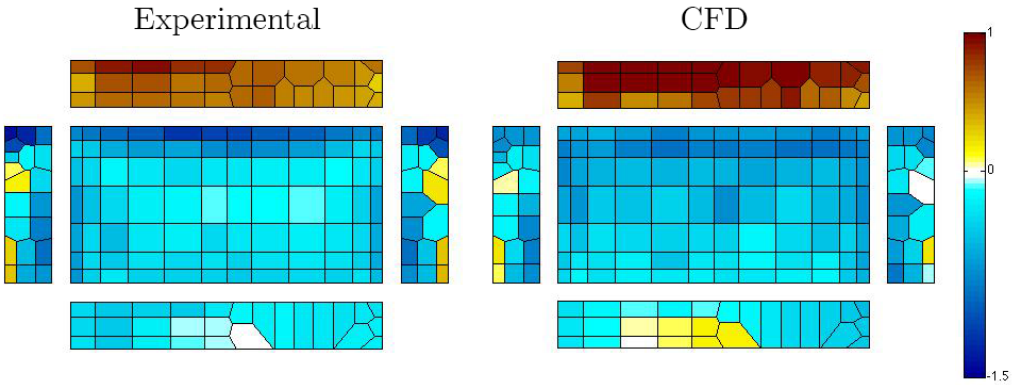

Figure 5.31: Hangar CFD simulation: C_p Skewness

similar to the experimental data both in term of peak amplitudes, peak symmetry (skewness) and mean value, as highlighted by the previous map.

The second time-history instead reflects all the problems that we previously said: while the positive peaks are similar between the two, the negative ones of the experimental time-history are far more marked, with experimental peaks that are $2 \div 2.5$ times stronger than the CFD ones.

All the results we have presented indicate that simulation doesn't correctly catch the separation bubble behind the leading edge of the building. We need to remember however that these results has been obtained with a fairly coarse mesh. Considering this, **the overall distribution of the pressure are pointing in the right direction**.

The y^+ value on the building is fairly high, with an average y^+ equal to 60 and peaks equal to 110. This is probably the main reason why the boundary layer separation isn't properly simulated. To better catch the separation of the boundary layer, the future work tries to add some layers of prisms cells on the hangar surface. This, however, involves severe problems with the Courant number and the stability of the solution near the edges, with the local Courant number that, using the same setup used in the empty Wind Tunnel simulation, reaches values equal to 10-15. The only solution to solve this would be to lower the time step by 5-10 times the time-step. This leads to a severe increase of the computational cost in terms of CPU time.

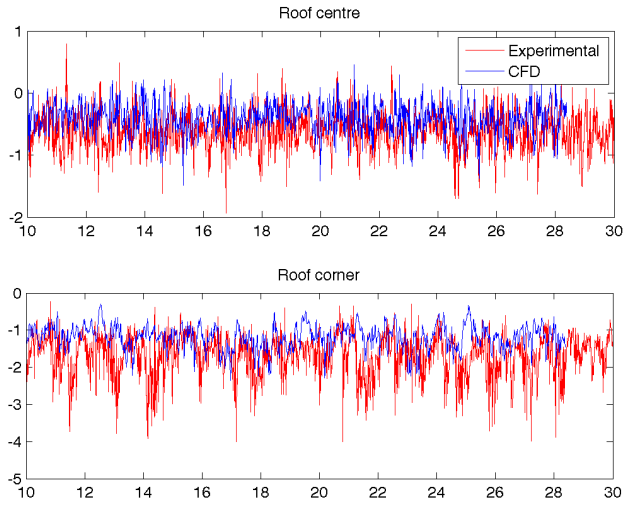

Figure 5.32: Hangar CFD simulation: time history of the C_p at the roof's centre (top) and at roof's corner (bottom)

5.8 Comparison with the synthetic turbulence method

As it has been explained in section 5.1, an alternative method for the simulation of a correct ABL to the direct simulation of a Wind Tunnel geometry, is the use of a synthetic turbulence inlet. This technique implies to use a complex code to generate a inlet plane velocity field $U(y, z, t)$ with assigned moments and spectra, through random sequences.

Parallel to the Wind Tunnel tests and the CFD simulation presented in this thesis, a synthetic turbulence simulation of the hangar has been carried out by Gorlé and Kóti (2014) at the Von Karmam Institute for Fluid Dynamics using the same building geometry.

Their simulation consisted of a $4m$ wide, $3m$ tall and $7m$ long domain shown in figure 5.33. The domain is significantly smaller than the PoliMi Wind Tunnel, with a volume 33 times smaller. This is the first and main evident advantage of the synthetic turbulence inlet method: since the simulation of the whole driver region is not required, the cost of the simulation is significantly lower.

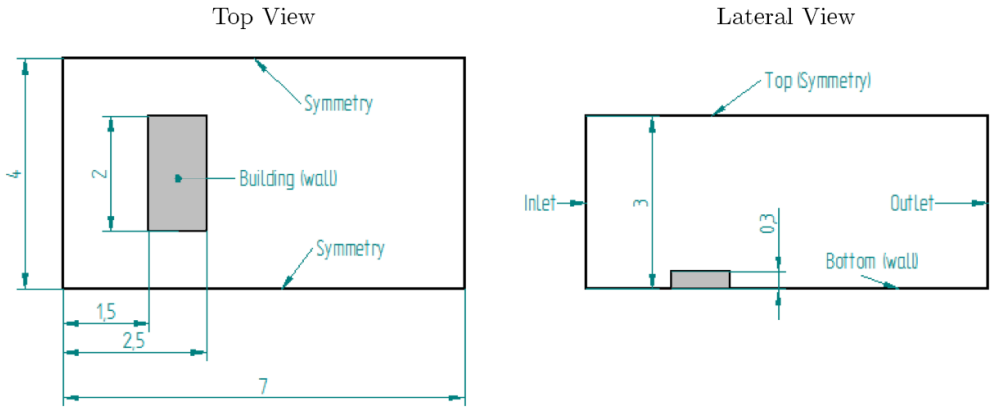

Figure 5.33: Domain used by David Koti for the synthetic turbulence simulation

The synthetic method used is based on the 2D digital filtering of a set of random data proposed by Xie and Castro (2008). This is base on the assumption that the cross-correlation function between two points is equal to:

$$R(r,0,0) = \exp\left(-\frac{\pi r}{2L}\right) \tag{5.10}$$

where L is the length scale. This correlation function is used for deriving a filter to process three two-dimensional sets of random data. The filter function can be written as follows,

$$u_m = \sum_{j=-N}^{N} b_j r_{m+j} \tag{5.11}$$

where r_m is a series of random data with zero mean and unity variance. The b_j is the filter coefficient and $N \geq 2n$, where n is the length scale L expressed in *grid units* and it's equal to $N = L/\Delta x$.

After some mathematical manipulation that can be found in Xie and Castro (2008), the b_j coefficient is defined as:

$$b_k = \exp\left(\frac{-\pi|k|}{n}\right)/\zeta \tag{5.12}$$

where k is the r coordinate expressed in *grid units* ($k = r/\Delta x$) and ζ is a normalisation factor used to ensure $\overline{u_m u_m} = 1$, equal to:

$$\zeta = \sum_{j=-N}^{N} b_j^2 \tag{5.13}$$

This method is used to calculate the $u_m(y, z)$ in a given time-step ensuring lateral and vertical correlation. The correlation in time, and thus in the streamwise direction, is obtained by defining the data on the next time step using:

$$\Psi_\beta(t+\Delta t, y, z) = \Psi_\beta(t, y, z) \exp\left(\frac{-\pi \Delta t}{2T_L}\right) + \psi_\beta(t, y, z)\left[1 - \exp\left(\frac{-\pi \Delta t}{T_L}\right)\right]^{0.5} \tag{5.14}$$

where $\psi(t, y, z)$ is obtained in the same way as $\Psi_\beta(t, y, z)$, but using a new slice of random data. T_L is the Lagrangian time scale and can be calculated from measurements or previous computations. In this case the T_L is assumed constant for the entire inlet plane. T_L is calculated using the Taylor's frozen turbulence hypothesis using the location at the height of the building from the measurements performed in the Wind Tunnel of Politecnico di Milano. The length scales L_y and L_z were assumed to be constant values. For further work, the inlet can be divided into zones each having their own constant length scales to improve the accuracy of the calculation.

The instantaneous velocity is then derived from the time-averaged velocity $\overline{u}_i$ and the Reynolds stress tensor using:

$$u_i = \overline{u}_i + a_{ij}\Psi_j \tag{5.15}$$

where

$$[a_{ij}] = \begin{bmatrix} R_{11}^{1/2} & 0 & 0 \\ R_{21}/a_{11} & (R_{22} - a_{21}^2)^{1/2} & 0 \\ R_{31}/a_{11} & (R_{32} - a_{21}a_{31})/a_{22} & (R_{33} - a_{31}^2 - a_{32}^2)^{1/2} \end{bmatrix} \tag{5.16}$$

and R_{ij} is the prescribed Reynolds-stress-tensor, estimated from experi-

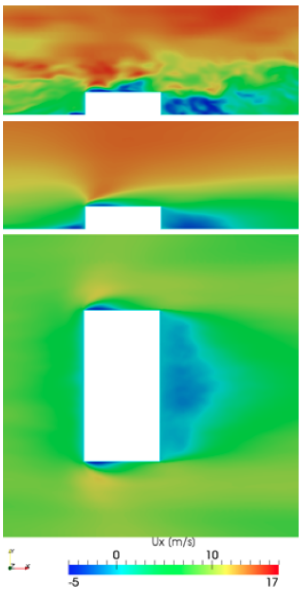

Figure 5.34: Flow around the building simulated by David Koti. From the top: instantaneous velocity field (lateral view), mean velocity field (lateral view) and mean velocity field (top view)

mental data measured in the wind tunnel of PoliMi. Note for a boundary layer flow which is homogeneous in the lateral direction, i.e. z in this notation, $R_{31} = R_{31} = 0$ and a_{31}, a_{32} vanish.

5.8.1 Results and comments

In this study the LES results for the flow around the building shows similar behaviour to those provided by the literature. Unsteady features and instantaneous realizations appear, the flow is highly disturbed in several respects. Tip vortices, developed relatively large vortex tube around the building downstream are shown. Separation zones are observed on the top, side, the front of and behind the building where the flow is always unsteady and this unsteadiness has important effects in the surface of the object such as providing a proper ventilation. However, the position of the separations varies greatly both in time and direction (spanwise or streamwise). The reattachment shows similarities, it is highly unsteady and the flow contains large scale turbulent structures.

A significant problem that occurred with the synthetic turbulence inlet is that the inlet condition does not respect the *divergence free* condition imposed by the continuity equation for an incompressible fluid. This error emerges during the solving of the *pressure correction equation*. Since this equation - obtained from a manipulation of the continuity one - is the one use to compute the pressure field, this inconsistency in the inlet BC led to significant *pressure waves* inside the domain that overcome any surface pressure on the building.

This error can be corrected forcing the inlet condition to be divergence-free through several methods discussed by Kim et al. (2013).

5.9 Conclusions and future work

The CFD reproduction of the Yoshikawa Wind Tunnel demonstrated the feasibility of the CFD as tool for the reproduction of the Wind Tunnel tests. After a proper benchmark with the Wind Tunnel results, the CFD could be use as further instrument to validate the scaling hypothesis or to measure flow fields that are experimentally difficult or even impossible to measure.

The current thesis however highlight that the direct simulation of a large Wind Tunnel requires still significant computational power. To solve the case presented in this thesis, 256 processors with about 1TB of memory has been used. Despite this, the optimal number of cell overcome these resources and pushed the hardware to his limit.

The results indicate that the approach used heads towards the right direction. The error committed on the mean value are close to be acceptable, while the errors on the peaks are still too large to consider the simulated pressures usable for structural design.

Future work should focus on a better reproduction of the ground roughness. Also a refined mesh near the hangar, such as a larger number of cells layers on its surface should help catching the correct flow behaviour behind the leading edge and allow a more accurate prediction of the peak pressures in that critical area. The synthetic turbulence method used by the Von Karman Institute allows to control the incoming flow more easily. This could allow to

use an arbitrary inlet flow without simulating the whole Wind Tunnel, reducing drastically the number of cells required and allowing an higher spatial resolution close to the building model using the same computational power. However only in the latest years the research - uneasily - is finally close to being able to correctly generate a synthetic the turbulence. As we have seen at the beginning of this chapter, a wrongly simulated turbulence decays rapidly and the obtained flow is not reliable for the estimation of the pressures acting on the building. The methods that will be developed have then to be benchmarked accurately before using them to replace the Wind Tunnel simulations as primary dimensioning tool. Simulations like the one proposed in this thesis, even if computationally expensive, should be used exactly for this purpose: estimate which degree of accuracy can be achieved with the CFD and find the best method for this purpose, and then see if the same accuracy can be achieved with the cheaper synthetic turbulence simulation.

Chapter 6

Peak estimation in wind engineering

In this chapter we will analyse the current state of the art for the prediction of the design pressure on a building façade. Both the Wind Tunnel and CFD outputs are indeed discrete stochastic time-histories. To correctly design a building façade element, the structural engineer need to compute a single load value; this however is not straightforward.

An important outcome from wind tunnel testing of low-rise buildings is a statistical assessment of peak pressure coefficients ($C_{p,peak}$), typically defined as a chosen fractile from a peak probability model whose parameters are determined from the observed data. The accuracy and precision (uncertainty) of this approach depend upon the form of the chosen peak probability model, the method used to identify its parameters, and the quantity of data available. In order to obtain an adequate space resolution, large model scales are desirable for low-rise buildings. This leads to a decreased time scale and long data records to achieve the desired full-scale equivalent time. Thus, there is a trade-off between the uncertainty of the estimated $C_{p,peak}$ and the desire to minimize data record lengths to limit the time and cost of wind tunnel experiments. Many techniques for estimating $C_{p,peak}$ have been proposed in the literature: Davenport (1964); Gioffrè et al. (2000); Huang et al. (2013); ISO (2009); Kwon and Kareem (2011); Peterka (1983); Sadek and Simiu (2002); Stathopoulos (1983); Tieleman et al. (2006).

6.1 Wind load peak estimation methods

Wind load peak estimation methods can be divided into three main categories: (1) determining $C_{p,peak}$ from observed peaks (observed peak methods); (2) mapping the peak distribution of a Gaussian process to a non-Gaussian peak cumulative distribution function (CDF) via the translation process (translation methods) and (3) compute a peak factor analysing the probability that one maxima from a sample of N maxima is higher than a threshold value (peak factor method).

Each of these methods has unique advantages and disadvantages. Below we present the most promising method of each category and then we apply one of them both to Wind Tunnel and CFD results to compare them.

6.1.1 Observed peak methods

Observed peak methods are based on the subdivision of the time-history in N subsets of duration t of each of which is then calculated the maximum value; this is then used to compute the expected peak value over an observation interval equal to t.

Observed peak methods include: a single observed peak value recorded during a sampling period (Stathopoulos and nationale du Canada, 1981), the mean of several observed maxima (Holmes et al., 1989), and a value corresponding to a chosen fractile from a probability distribution (commonly Gumbel) fitted to observed maxima (Cook and Mayne, 1980; Ho et al., 2005; Pierre et al., 2005). The last method (Gumbel method) is the most flexible among the three, offering a statistical quantification of the peak at a selected fractile rather than a single observed peak or simple average.

The Gumbel method is based on the assumption that the Gumbel distribution fits the distribution of peak wind pressure coefficient. The Gumbel distribution is:

$$F_{X_{pk}}(x,t) = \exp(-\exp(-\alpha_t(x - U_t))) \tag{6.1}$$

where x is the pressure data and t is the is the duration in which a single peak

is observed (reference duration). α_t and U_t are the distribution parameters that are determined based upon N observed peaks using one of a number of available methods: BLUE method, maximum likelihood method, probability weighted moments, method of moments or probability plot method.

While the plot method is the easiest to understand, this leads to uncertain results. The method of moments has proved to be easy to implement and robust. The other methods have not been tested in this thesis.

Gavanski et al. (2013) showed that the Gumbel method as defined above yields almost identical results to the observed peaks methodology proposed in the ISO (2009) standard. Kasperski (2003) and Holmes and Cochran (2003) applied the Type III Extreme Value Distribution and three-parameter Generalized Extreme Value Distribution to fit the peak wind pressure coefficients, respectively. Holmes and Cochran (2003) recommended the Gumbel model for its simplicity.

The main shortcoming of the Gumbel method is the amount of data it needs to be applied. This method indeed requires a total record duration of $t_{tot} = Nt$. For the determination of α_t and U_t to be robust, N should be greater than or equal to 10. The reference time t is usually assumed equal to $10min$ at full scale. This implies that the total record duration should be greater than or equal to $100min$ at full scale. Depending on the time scale, this requires long Wind Tunnel testing records that increase the Wind Tunnel cost e.g. using the scales presented in table 4.1, $100min$ full scale are equal to approximately $5min$ $20sec$. While the Wind Tunnel records were $6min$ long allowing the Gumbel method to be applied, the CFD simulations were only $60sec$ long.

Cook and Mayne (1980) presented a procedure to convert the Gumbel parameters between different reference durations. This allows the estimation of α_t and U_t using a sufficient N within a relatively short data record, followed by a conversion to the desired longer reference duration T. For the two time reference duration values ($t < T$), the conversion is (Cook and Mayne, 1980):

$$\begin{aligned} \alpha_T &= \alpha_t \\ U_T &= U_t + 1/\alpha_t \ln(T/t) \end{aligned} \tag{6.2}$$

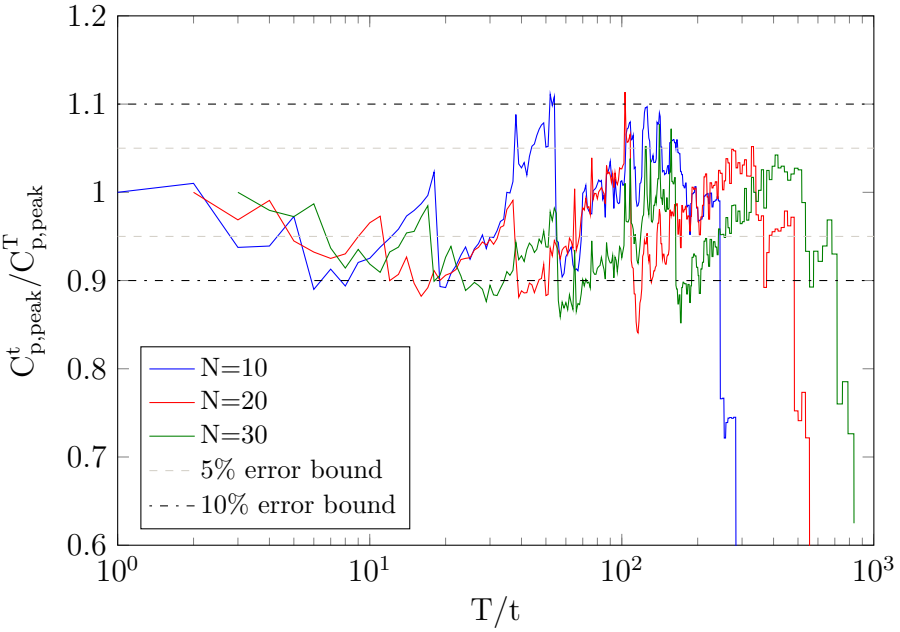

Figure 6.1: Errors of the formula by Cook and Maine with different N and T/t

In figure 6.1 the $C_{p,peak}$ computed with the Gumbel method and $t = T$ is compared with those computed applying equation 6.2 to subset shorter than T. The results indicates that this method returns error smaller than 10% for $T/t < 40$. Increasing the number of subset does not offer a significant improvement.

6.1.2 Translation methods

The perceived data length requirement of the Gumbel method has led to the development of alternative methods for the estimation of $C_{p,peak}$ from short records. The complete time series is used to estimate a peak CDF from an underlying Gaussian process; a coordinates transformation (hereafter *translation*) maps the experimental CDF to a Gaussian CDF, then the peak CDF of the assigned non-Gaussian time series is obtained using the inverse translation on the known Gaussian peak CDF.

The idea underlying the translation methods is to find a translation function $g(\bullet)$ that maps a standardised Gaussian process u to a given non-Gaussian process x.

$$x = g(u) \qquad u = g^{-1}(x) \tag{6.3}$$

The peak distribution of a Gaussian process has been calculated by Rice (1944).

$$F_{U_pk}(u,t) = \exp[-\nu_0\, t\, \exp(-u^2/2)] \tag{6.4}$$

in which t is the reference duration and ν_0 is the zero up-crossing rate that can be be determined by counting the up-crossing rate ν_y of x above its median or computing the spectral ratio (Sadek and Simiu, 2002).

The desired CDF of the peak of the non-Gaussian process x within the reference duration t, $F_{X_pk}(x,t)$, is obtained by substituting the inverse translation function, equation 6.3, into equation 6.4.

$$F_{X_pk}(x,t) = F_{U_pk}(u,t) = F_{U_pk}(g^{-1}(x),t) = \exp[-\nu_0\, t\, \exp(-(g^{-1}(x))^2/2)] \tag{6.5}$$

$C_{p,peak}$ is then identified as x_{pk} at a chosen fractile in F_{X_pk}.

Various methods have been proposed to determine the translation function $g(\bullet)$. Kareem and Zhao (1994) used the moment-based Hermite polynomial to define the translation between the Gaussian and non-Gaussian processes. Kwon and Kareem (2011) employed an updated and more robust Hermite polynomial model Winterstein and Kashef (2000). Sadek and Simiu (2002) modelled the non-Gaussian time series by using gamma and Gaussian distributions to fit the long and short tails, respectively. The parameters in the fitted distributions were re-evaluated by using the theoretical moment estimators in Tieleman et al. (2006). Ben Ayed et al. (2011) employed a translation model to full scale pressure data and compared results with values in ASCE 7. Huang et al. (2013) established the mapping relationship between the non-Gaussian CDF and its underlying Gaussian CDF based on a probabilistic model using the kernel smoothing technique. Yang et al. (2013) improved the method of Kwon and Kareem (2011) for strongly non-Gaussian data with an alternative approximate expression relating the skewness and kurtosis of the measured data and the Hermite polynomial parameters.

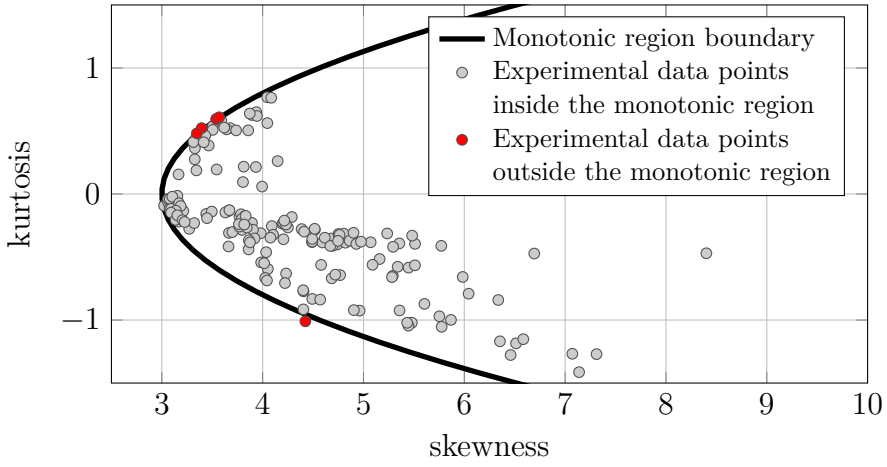

Figure 6.2: Skewness and kurtosis of all the taps on the hangar and the monotonic region for the Peng and Yang model

The Peng and Yang Hermite polynomial model

Yang et al. (2013) used the same third order Hermite model for a softening translation process presented by Winterstein and Kashef (2000)

$$x = g(u) \approx k[u + c_3(u^2 - 1) + c_4(u^3 - 3u)] \tag{6.6}$$

with $k = 1/\sqrt{1 + 2c_3^2 + 6c_4^2}$.

The coefficient c_3 and c_4 are function of the skewness and the kurtosis of the process x. The functions for their calculation proposed by Yang et al. (2013) are:

$$\begin{aligned} c_3 = \; & 0.1967\gamma_3 - 0.01646\gamma_3\gamma_4 + 0.01809\gamma_3^3 + 7.438 \cdot 10^{-4}\gamma_3\gamma_4^2 \\ & -9.209 \cdot 10^{-4}\gamma_3^3\gamma_4 - 1.366 \cdot 10^{-5}\gamma_3\gamma_4^3 + 1.527 \cdot 10^{-4}\gamma_3^5 \\ & +1.07 \cdot 10^{-5}\gamma_3^3\gamma_4^2 + 8.823 \cdot 10^{-8}\gamma_3\gamma_4^4 \\ c_4 = \; & -0.0721 + 0.03176\gamma_4 - 0.02942\gamma_3^2 - 0.00179\gamma_4^2 + 0.002348\gamma_3^2\gamma_4 \\ & +5.965 \cdot 10^{-5}\gamma_4^3 - 6.282 \cdot 10^{-4}\gamma_3^4 - 6.355 \cdot 10^{-5}\gamma_3^2\gamma_4^2 - 9.692 \cdot 10^{-7}\gamma_4^4 \\ & +1.497 \cdot 10^{-5}\gamma_3^4\gamma_4 + 5.457 \cdot 10^{-7}\gamma_3^2\gamma_4^3 + 6.049 \cdot 10^{-9}\gamma_4^5; \end{aligned} \tag{6.7}$$

where γ_3 and γ_4 are the skewness and the kurtosis of the process x.

In order to guarantee that $g^{-1}(\bullet)$ exists, $g(\bullet)$ must be strictly monotonic, which requires the following inequality be satisfied:

$$c_3^2 + 3c_4(3c_4 - 1) \leq 0 \tag{6.8}$$

An approximation of this curve is given by Winterstein and MacKenzie (2013):

$$3 - \gamma_4 + (1.25\gamma_3)^2 \leq 0 \tag{6.9}$$

According to Yang et al. (2013), if small deviations from the monotonic region occurs, the kurtosis and the skewness can be slightly modified to fall on the border of that region. The suggested method they propose is to retain the measured kurtosis and solve for skewness using equation 6.9.

This method appears to be more robust than the Gumbel one, needing a smaller time duration (**?**).

6.1.3 Peak factor method

The peak factor method aim to compute the maximum value of a random process using the formula:

$$x_{peak} = \mu_x + g(x,t)\sigma_x \tag{6.10}$$

where μ_x is the mean value of the process x and σ_x it's standard deviation. $g(x,t)$ is called *peak factor*.

This method is currently used to calculate peak values for wind loads and load effects in several national codes, such as ASCE 7-02 and AIJ. Although this codes use a very simple equation for the determination of g that is based on the assumption that the process is Gaussian. The equation proposed in ASCE and AIJ, moreover, does not take explicitly into account the bandwidth of the process. Below we present both this equation and two "improved" version, one by Kareem and Zhao (1994) and one by Pillai and Tamura (Pillai and Tamura).

For a Gaussian narrowband process the peak factor g has been derived by Davenport (1964). It is given by:

$$g = \sqrt{2 \ln N} + \frac{\gamma}{\sqrt{2 \ln N}} \tag{6.11}$$

where γ is the Euler-Mascheroni constant equal to 0.57721, and N is number of zero-crossing in the reference time t, that is equal to $N = \nu_0 T$ where ν_0 is the cyclic rate. ν_0 can be derived using the spectral moments method and it's equal to:

$$\nu_0 = \sqrt{\frac{m_2}{m_0}} \tag{6.12}$$

where

$$m_i = \int_0^\infty f^i S_y(f) \, \mathrm{d}f \tag{6.13}$$

and $S_y(f)$ is the power spectral density of the normalised process:

$$y = (x - \mu_x)/\sigma_x \tag{6.14}$$

The Davenport equation can be simplified defining the constant

$$\phi = \sqrt{2 \ln N} \tag{6.15}$$

obtaining:

$$g = \phi + \frac{\gamma}{\phi} \tag{6.16}$$

To account the non-Gaussianity of the experimental PDF, this is described using a Gram-Charlier PDF, that is given by:

$$P(x) = \varphi(x) \left[1 + \sum_{n=1}^{N} h_n H_n(x) \right] \tag{6.17}$$

where $\varphi(x)$ is a standard Gaussian probability density function

$$\varphi(x) = \sqrt{2\pi} \exp(-x^2/2) \tag{6.18}$$

and $H_n(x)$ are the Hermite polynomials.

After some mathematical manipulation, Kareem and Zhao (1994) obtained the equation for the peak factor accounting the non-Gaussianity of the data PDF. This is:

$$g = \alpha \left\{ \left(\phi_{max} + \frac{\gamma}{\phi_{max}} \right) + h_3 \left(\phi_{max}^2 + 2\gamma - 1 \right) + \right. \\ \left. + h_4 \left[\phi_{max}^3 + 3\phi_{max} \left(\gamma - 1 \right) + \frac{3}{\phi_{max}} \left(\frac{\pi^2}{12} - \gamma + \frac{\gamma^2}{2} \right) \right] \right\} \quad (6.19)$$

where h_3, h_4 and α are the coefficient that take into account the skewness and the kurtosis of the PDF and are defined by:

$$h_3 = \frac{\gamma_3}{4 + \sqrt{6\gamma_4 - 14}} \qquad h_4 = \frac{\sqrt{1.5\gamma_4 - 3.5} - 1}{18} \\ \alpha = 1/\sqrt{1 + 2h_3^2 + 6h_4^2} \quad (6.20)$$

ϕ_{max} is defined in the same way of ϕ, but in the place of the number of zero crossing N, uses the number of maxima N_{max} that is defined by:

$$N_{max} = \nu_{max} T \qquad \text{with} \qquad \nu_{max} = \sqrt{\frac{m_4}{m_2}} \quad (6.21)$$

Thus:

$$\phi_{max} = \sqrt{2 \ln N_{max}} \quad (6.22)$$

Pillai and Tamura (Pillai and Tamura) proposed a different equation for ϕ_{max} that takes explicitly into account also the bandwidth of the analysed process. Their definition for ϕ_{max} is:

$$\phi_{max} = \sqrt{2 \ln \left(\sqrt{1 - \varepsilon^2} N_{max} \right)} \quad (6.23)$$

where ε is the bandwidth parameter defined as:

$$\varepsilon = \sqrt{1 - \frac{m_2^2}{m_0 m_4}} \qquad 0 \leq \varepsilon \leq 1 \quad (6.24)$$

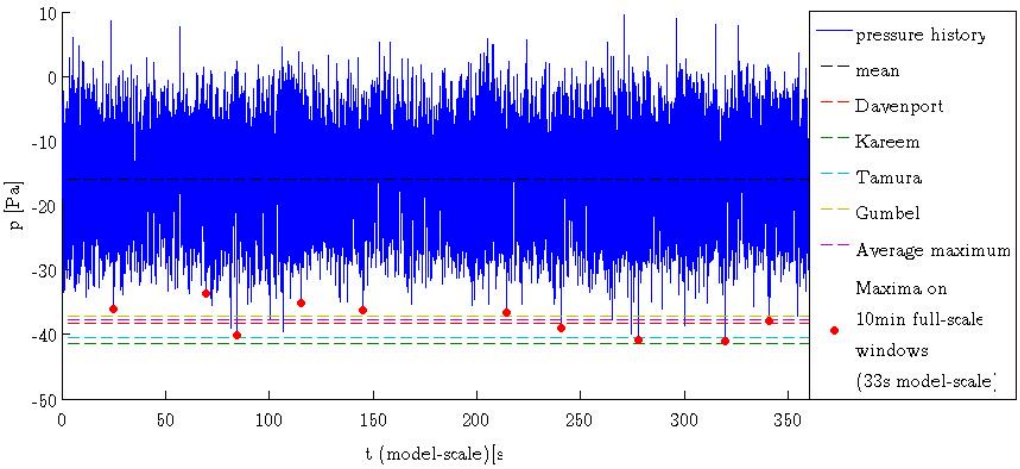

Figure 6.3: Comparison of estimated peak value using different methods - slightly non-Gaussian process

This parameter is close to 0 for narrow band process and it increases as the bandwidth increases, reaching 1 for the wide band process.

Once that the peak factor is know, the peak vale can be computed using equation 6.10. This method provides satisfying results, overestimating the peak factor by about $5 \div 10\%$.

6.2 Comparison between the proposed methods

To show the different behaviour of the methods presented in section 6.1, these have been applied to two process: firstly at a slightly non-Gaussian process, then to a strongly non-Gaussian one.

In the comparison below the Peng and Yang Hermite polynomial method will not be tested , because some problems occurred during the implementation of this method inside the code. The benchmark of this method will be executed in a future work.

In figure 6.3 the methods presented above are applied to a $6min$ record from the Wind Tunnel test. The skewness of the considered tap is equal to -0.014 and its kurtosis is equal to 3.154. The process is therefore really close to be Gaussian.

It appears that the Gumbel and the Davenport methods returns value only 1.5% respectively smaller and higher than the average on the observed peaks. The error is therefore completely acceptable.

The fact that the Davenport methods works so good is due to the almost perfect Gaussianity of the considered process.

The Kareem and the Tamura methods show slightly lower performance with an error equal to 11.9% for the Kareem method and to 9% for the Tamura methods. From an engineering point of view however these errors are always on the safe side, expecting higher pressure that observed ones (the Kareem peak pressure is even higher than the maximum pressure observed in the whole $100min$ full-scale process duration).

The expected peak value are summarised in table 6.1

Method	Peak pressure [Pa]	Error (compared with Gumbel method)
Gumbel	37.0893	-
Mean peak	37.6371	+1.48%
Davenport	38.2356	+3.0.9%
Kareem	41.3978	+11.62%
Tamura	40.4311	+9.01%

Table 6.1: Expected peak value for a Gaussian process with different methods

In figure 6.4 the methods are applied again to a strongly non-Gaussian time-history. In this case the skewness is equal to -1.4135 and the kurtosis is equal to 7.1384.

Again, the Gumbel method returns a peak value close to the mean peak value with an error lower than 2.5%. The performance of the peak factor methods instead have worsened. As it was expected, the Davenport method fails completely in the peak prediction, expecting a peak value 41% lower than the Gumbel method. This is due to the strongly negative skewness that shifts the negative peak values toward minus infinity. The Kareem method overestimate again the peak value, this time predicting a value 13% higher than the highest observed peak and 37% higher than the value predicted by the Gumbel method. The Tamura method performs slightly better, again

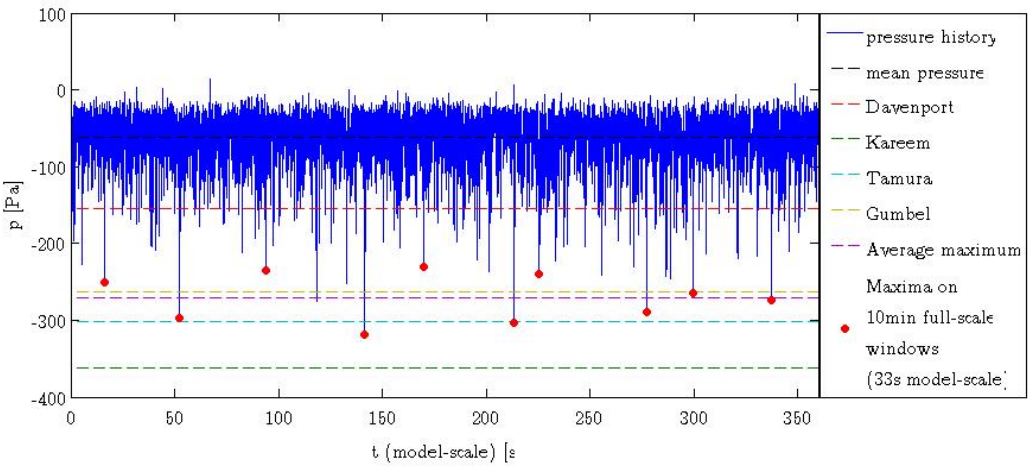

Figure 6.4: Comparison of estimated peak value using different methods - slightly non-Gaussian process

overestimating the peak value expected using the Gumbel method, but "only" by 15%.

The expected peak value are summarised in table 6.2

Method	Peak pressure [Pa]	Error (compared with Gumbel method)
Gumbel	263.68	-
Mean peak	270.41	+2.55%
Davenport	154.19	-41.52%
Kareem	362.20	+37.37%
Tamura	301.93	+14.51%

Table 6.2: Expected peak value for a strongly non-Gaussian process with different methods

A further analysis can be done to study the convergence of the expected peak pressure as the signal length becomes longer. In figure 6.5 appears that the differences in the value predicted by the Gumbel method with 10 subdivisions for a signal $50s$ long or longer are below 10%. This is a better estimation than the Tamura method with a signal $360s$ long. Also the mean peak value of the N higher peaks in the time history, where $N = \text{floor}(t/t_{ref})$ gives acceptable results for $t > 60s$.

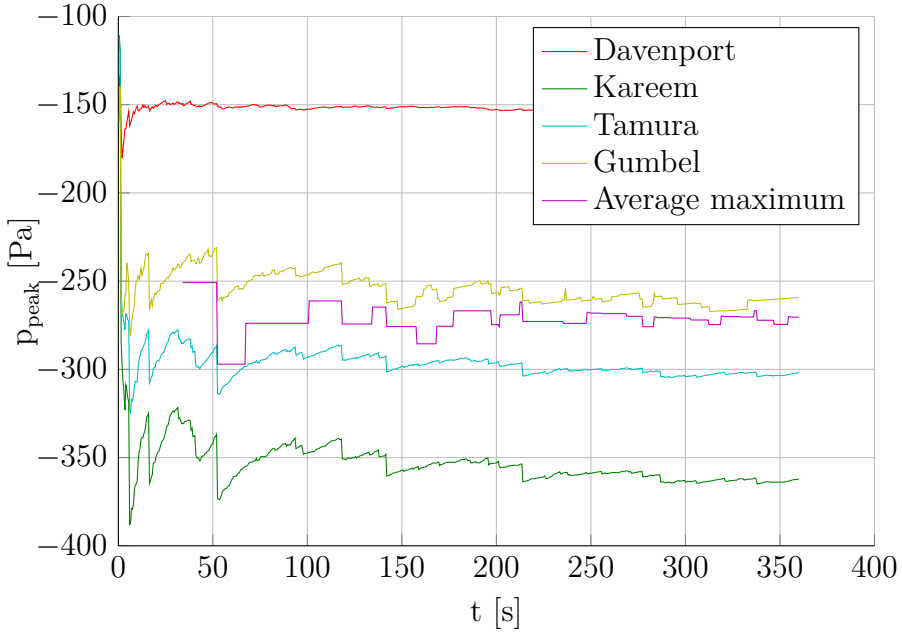

Figure 6.5: Comparison of estimated peak value using different methods with different signal length - slightly non-Gaussian process

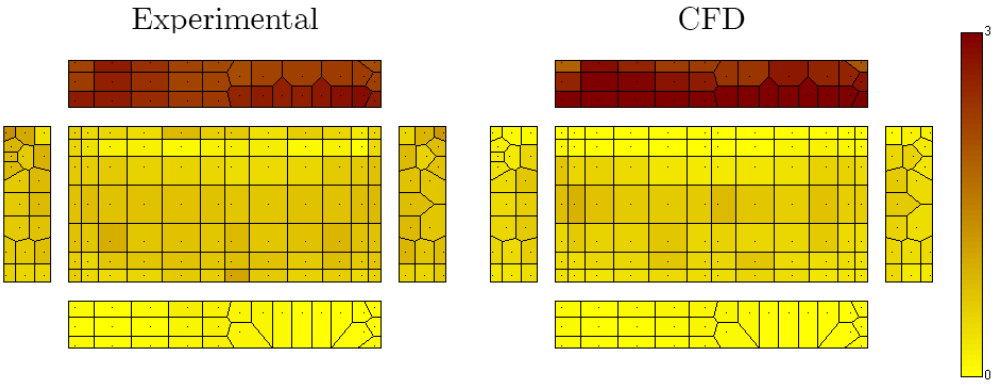

Figure 6.6: $C^+_{p,pk}$ distribution in the experimental and in the CFD simulation

6.3 Comparison of pressure peak values between CFD and Wind Tunnel experiment

In the section below we will compare the peak pressure distribution obtained with the Wind Tunnel Test, with the distribution obtained with the CFD simulations. Based upon what have been said in the previous section, the peaks will be computed using the Gumbel method, dividing the time-history in 10 parts. For the CFD, this cause each part to be only $6sec$ long. Using the Cook and Maine method presented in section 6.1.1 this value will be projected to a $30sec$ model-scale return period, equal to a $10min$ full-scale one.

In figure 6.6 the positive peaks $C^+_{p,pk}$ can be compared. The comparison indicates a good agreement between the two case: in both experimental and CFD pressure maps the $C^+_{p,pk}$ is close to 3 on the windward face, while it is between 0.5 and 0.8 on the rear part of the roof and lateral walls and almost 0 on the leeward wall.

Some problems occurs behind the leading edge. In the experimental test the $C^+_{p,pk}$ in that area is just slightly lower than the rest of the roof. Instead in the CFD simulation the $C^+_{p,pk}$ behind the leading edge is close to 0, never

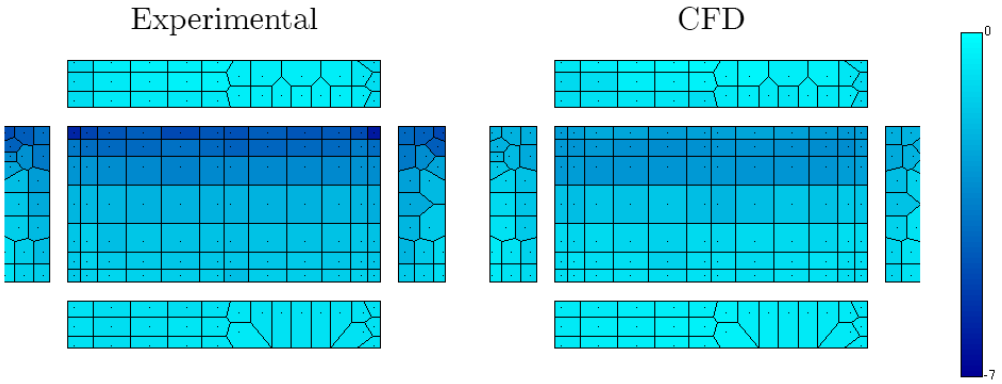

Figure 6.7: $C^-_{p,pk}$ distribution in the experimental and in the CFD simulation

exceeding 0.15.

In figure 6.7 the negative peaks $C^-_{p,pk}$ are compared . Again, the windward wall's $C^-_{p,pk}$ are similar in the two cases, with values between -0.4 and -1. The peaks are a little lower in the CFD simulation on the rear part of the roof and lateral walls: while the experimental test predicts values between -1.5 and -2.2, the CFD simulation never exceeds -1.9, with a difference between -0.2 and -0.8.

Again the most problematic area is the one behind the leading edge. Here the separation bubble generates strongly negative peaks in the experimental test, that lead to $C^-_{p,pk}$ up to -4.7 and even -6.2 on the corner. The CFD simulation, probably due to a too much coarse mesh, does not catch this behaviour and the $C^-_{p,pk}$ never exceeds -3.

Chapter 7

Conclusions

In the present work is presented a cross validation among the experimental results obtained inside the Wind Tunnel of the Politecnico di Milano and CFD simulation on a low rise building using an LES turbulence model. The purpose of this cross validation was to demonstrate that using the LES technique is possible to obtain realistic peak pressures, and not only a realistic mean value.

Literature survey clearly shows that a necessary condition for the correct simulation of unsteady pressures - e.g. the dimensioning negative peak pressures - is the correct simulation of the incoming turbulent Atmospheric Boundary Layer (correctly scaled with respect to the full-scale ABL). At this purpose several strategies exist; these can be divided into three main categories: the recycle technique, the synthetic turbulence technique and the direct simulation of the ground roughness.

The recycle technique, that has been largely validated in the past years, cannot be applied in the case of a not completely developed boundary layer, such as the POLIMI Wind Tunnel one, as well as most of the other Boundary Layer Wind Tunnels for Wind Engineering applications. The presence of the spires, moreover, makes the domain non-periodic, excluding this technique.

Synthetic turbulence inlet techniques have been developed, but a completely validated one still does not exists. An attempt to use this technique coordinated with the present thesis work has been carried out by Gorlé and

Kóti (2014). Due to the absence of a wide validation, however, it is difficult to ascribe the differences of the surface pressure to the CFD-LES technique rather than to an error in the simulation of the incoming flow.

A second, but not less important, problem with the cross validation of the Wind Tunnel test with a synthetic turbulent inlet is that a complete knowledge of the flow characteristics on a plane in the middle of the domain is not experimentally available; introducing additional uncertainties.

For the reasons above, the direct simulation of the actual upwind channel geometry of the Wind Tunnel - although extremely expensive - is mandatory in the case of a non-periodic domain with a not completely developed boundary layer, such as the present one.

The preliminary benchmarks have hinted that the correct reproduction of the Wind Tunnel ground roughness requires a very fine mesh near the floor. The simulation of the whole wind tunnel, thus, required to find a compromise between the necessary spatial resolution and the available computational power (that was equal to 256 CPUs and ∼1TB of memory). This compromise has been only partially found . The obtained data showed promising results for this technique: the mean pressure distribution and the peaks pressures obtained on most of the surface of the building are close to the experimental ones. However the results indicate that a correct reproduction of the incoming flow would require a finer mesh on the ground. Moreover the pressure distribution on the building showed that the separation bubble behind the leading edge was not correctly reproduced, again likely because of a too coarse mesh. This suggests that - with a refined mesh - better results are obtainable.

Future work should try to refine the mesh close to the building and add more refined wall layers. This will result in a lower time-step and thus in a longer computation time.

Although the direct simulation of the actual Wind Tunnel geometry has proved to be extremely expensive from the computational point of view, it's important to this technique is not intended to be itself the best inlet condition for future CFD simulation work concerning wind-building interaction. Instead, the results of this research can be used as an intermediate benchmark

between the Wind Tunnel simulation and computationally lighter techniques, such as the recycling or the synthetic turbulence ones presented in section 5.1 and 5.8.

In chapter 6 we introduced some methods for the estimation of the peak pressure. The aim of this comparison was to find a method able to predict the peak pressure with an acceptable error, even with a short time base. The Gumbel method, originally meant to be used with long time series, revealed a good accuracy also when used on short ones, if corrected using the Cook and Mayne (1980) correction equation. This could allow to reduce the simulated duration of the experiment, drastically reducing the CFD computational cost and the Wind Tunnel test duration.

The peak factor methods showed a quick convergence, but predicted value was usually $10 \div 15\%$ higher than the observed peaks. Future work should benchmark the Yang et al. (2013) method that in **?** demonstrated a very good accuracy compared with the Gumbel method, but that has not been tested in this thesis.

The key result of the present research is that using a consistent incoming ABL flow, the pressure time-space distribution simulated promisingly compare with the experimental one, allowing future research to investigate in depth existing correlations among the structure of the incoming turbulence and the structure of the time dependent pressure field, still not fully understood.

Bibliography

Anderson, J. (1995). *Computational fluid dynamics : the basics with applications*. New York: McGraw-Hill.

Ben Ayed, S., L. Aponte-Bermudez, M. Hajj, H. W. Tieleman, K. R. Gurley, and T. Reinhold (2011, December). Analysis of hurricane wind loads on low-rise structures. *Engineering Structures 33*(12), 3590–3596.

Calderone, I. and W. Melbourne (1993, September). The behaviour of glass under wind loading. *Journal of Wind Engineering and Industrial Aerodynamics 48*(1), 81–94.

Cao, J., Y. Tamura, and A. Yoshida (2012, April). Wind pressures on multi-level flat roofs of medium-rise buildings. *Journal of Wind Engineering and Industrial Aerodynamics 103*, 1–15.

Cook, N. J. (1990). *The Designer's Guide to Wind Loading of Building Structures - Part 2: Static structures*. Building Research Establishment Report. Building Research Establishment, Department of the Environment.

Cook, N. J. and J. R. Mayne (1980). A refined working approach to the assessment of wind loads for equivalent static design. *Journal of Wind Engineering and Industrial Aerodynamics 6*(1-2), 125–137.

Davenport, A. G. (1964). Note on the distribution of the largest vaue of a random function with application to gust loading. *ICE Proceedings 28*(Volume 28, Issue 2), 187–196(9).

Easom, G. (2000). *Improved Turbulence Models for Computational Wind Engineering*. Ph. D. thesis, University of Nottingham.

Gavanski, E., K. R. Gurley, and G. Kopp (2013). Uncertainties in the estimation of peak pressures on low-rise buildings with Gumbel fitting approach. In *Proceedings of the 12th Americans Conference on Wind Engineering*, Seattle, WA.

Geetha Rajasekharan, S., M. Matsui, and Y. Tamura (2013, January). Characteristics of internal pressures and net local roof wind forces on a building exposed to a tornado-like vortex. *Journal of Wind Engineering and Industrial Aerodynamics 112*, 52–57.

Gioffrè, M., V. Gusella, and M. Grigoriu (2000, October). Simulation of non-Gaussian field applied to wind pressure fluctuations. *Probabilistic Engineering Mechanics 15*(4), 339–345.

Gorlé, C. and D. Kóti (2014). Implementation of the 2D digital filter method based turbulent inlet boundary condition to OpenFOAM.

Griffith, A. A. (1921). The phenomena of rupture and flow in solids. *Philosophical Transactions of the Royal Society of London. Series A, Containing Papers of a Mathematical of Physical Character 221*(582-593), 163–198.

Haldimann, M. (2006). *Fracture strength of structural glass elements - analytical and numerical modelling , testing and design*. Ph. D. thesis.

Haldimann, M. (2008). *Structural use of glass*. Zurich, Switzerland: International Association for Bridge and Structural Engineering.

Ho, T., D. Surry, D. Morrish, and G. Kopp (2005, January). The UWO contribution to the NIST aerodynamic database for wind loads on low buildings: Part 1. Archiving format and basic aerodynamic data. *Journal of Wind Engineering and Industrial Aerodynamics 93*(1), 1–30.

Holmes, J. D. (1985, October). Wind action on glass and Brown's integral. *Engineering Structures 7*(4), 226–230.

Holmes, J. D. and A. Allsop (2013a). Averaging times and gust durations for codes and standards. Number 1, pp. 4–7.

Holmes, J. D. and A. Allsop (2013b). Gust durations and effective frontal areas – with applications to codes and standards.

Holmes, J. D. and R. Best (1981, May). An approach to the determination of wind load effects on low-rise buildings. *Journal of Wind Engineering and Industrial Aerodynamics 7*(3), 273–287.

Holmes, J. D. and L. Cochran (2003, June). Probability distributions of extreme pressure coefficients. *Journal of Wind Engineering and Industrial Aerodynamics 91*(7), 893–901.

Holmes, J. D., G. R. Walker, W. H. Melbourne, and A. W. E. Society (1989). *A Commentary on the Australian Standard for Wind Loads AS 1170*. Number pt. 2;pt. 1989. Melbourne: Australian Wind Engineering Society.

Hoxey, R., P. Richards, and J. Short (2002, April). A 6 m cube in an atmospheric boundary layer flow -Part 1. Full-scale and wind-tunnel results. *Wind and Structures 5*(2_3_4), 165–176.

Huang, M. F., W. Lou, C. M. Chan, N. Lin, and X. Pan (2013, December). Peak Distributions and Peak Factors of Wind-Induced Pressure Processes on Tall Buildings. *Journal of Engineering Mechanics 139*(12), 1744–1756.

ISO (2009). *ISO 4354: 2009 Wind actions on structures*, Volume 2009. International Standard Organization.

Kareem, A. and J. Zhao (1994, August). Analysis of Non-Gaussian Surge Response of Tension Leg Platforms Under Wind Loads. *Journal of Offshore Mechanics and Arctic Engineering 116*(3), 137–144.

Kasperski, M. (2003, March). Specification of the design wind load based on wind tunnel experiments. *Journal of Wind Engineering and Industrial Aerodynamics 91*(4), 527–541.

Kasperski, M. (2007, October). Design wind loads for a low-rise building taking into account directional effects. *Journal of Wind Engineering and Industrial Aerodynamics 95*(9-11), 1125–1144.

Kataoka, H. and M. Mizuno (2002, April). Numerical flow computation around aeroelastic 3D square cylinder using inflow turbulence. *Wind and Structures 5*(2_3_4), 379–392.

Kim, Y., I. P. Castro, and Z. T. Xie (2013, September). Divergence-free turbulence inflow conditions for large-eddy simulations with incompressible flow solvers. *Computers & Fluids 84*, 56–68.

Kwon, D. K. and A. Kareem (2011, December). Peak Factors for Non-Gaussian Load Effects Revisited. *Journal of Structural Engineering 137*(12), 1611–1619.

Li, Q. and G. Li (2005, September). Time-dependent reliability analysis of glass cladding under wind action. *Engineering Structures 27*(11), 1599–1612.

Lund, T. S. (1998). Generation of Turbulent Inflow Data for Spatially-Developing Boundary Layer Simulations. *Journal of Computational Physics 140*, 233–258.

Lund, T. S. (2003, August). The use of explicit filters in large eddy simulation. *Computers & Mathematics with Applications 46*(4), 603–616.

Maruyama, Y., T. Tamura, Y. Okuda, and M. Ohashi (2013, November). LES of fluctuating wind pressure on a 3D square cylinder for PIV-based inflow turbulence. *Journal of Wind Engineering and Industrial Aerodynamics 122*, 130–137.

Montazeri, H. and B. Blocken (2013, February). CFD simulation of wind-induced pressure coefficients on buildings with and without balconies: Validation and sensitivity analysis. *Building and Environment 60*, 137–149.

Muehleisen, R. T. and S. Patrizi (2013, February). A new parametric equation for the wind pressure coefficient for low-rise buildings. *Energy and Buildings 57*, 245–249.

Overend, M. and K. Zammit (2006). Wind loading on cladding and glazed façades. In *International Symposium on the Application of Architectural Glass*, pp. 1–10.

Peng, X., L. Yang, E. Gavanski, K. R. Gurley, and D. Prevatt (2014, March). A comparison of methods to estimate peak wind loads on buildings. *Journal of Wind Engineering and Industrial Aerodynamics 126*, 11–23.

Peterka, J. (1983, December). Selection of local peak pressure coefficients for wind tunnel studies of buildings. *Journal of Wind Engineering and Industrial Aerodynamics 13*(1-3), 477–488.

Pierre, L. S., G. Kopp, D. Surry, and T. Ho (2005, January). The UWO contribution to the NIST aerodynamic database for wind loads on low buildings: Part 2. Comparison of data with wind load provisions. *Journal of Wind Engineering and Industrial Aerodynamics 93*(1), 31–59.

Pillai, S. N. and Y. Tamura. Generalized peak factor and its application to stationary random processes in wind engineering applications. (285).

Piomelli, U. (2010). Large-eddy simulation of turbulent flows.

Raupach, M. R., A. S. Thom, and I. Edwards (1980, June). A wind-tunnel study of turbulent flow close to regularly arrayed rough surfaces. *Boundary-Layer Meteorology 18*(4), 373–397.

Rice, S. (1944). Mathematical Analysis of Random Noise. *15*(July), 1–89.

Richards, P., R. Hoxey, and L. Short (2001, December). Wind pressures on a 6m cube. *Journal of Wind Engineering and Industrial Aerodynamics 89*(14-15), 1553–1564.

Rocchi, D., P. Schito, and A. Zasso (2010). Evaluation of unsteady pressure fluctuations on surfaces using CFD. In *The Fifth International Symposium on Computational Wind Engineering (CWE2010)*, pp. 1–8.

Rocchi, D., P. Schito, and A. Zasso (2011). Investigation on the relation between incoming wind characteristics and surface pressure distribution.

Sadek, F. and E. Simiu (2002, May). Peak Non-Gaussian Wind Effects for Database-Assisted Low-Rise Building Design. *Journal of Engineering Mechanics 128*(5), 530–539.

Stathopoulos, T. (1983, January). Fluctuating Wind Pressures on Low Building Roofs. *Journal of Structural Engineering 109*(1), 266–271.

Stathopoulos, T. and B. nationale du Canada (1981). *Turbulent Wind Action on Low Rise Buildings*. Canadian theses on microfiche. National Library of Canada.

Tamura, Y., H. Kikuchi, and K. Hibi (2001, December). Extreme wind pressure distributions on low-rise building models. *Journal of Wind Engineering and Industrial Aerodynamics 89*(14-15), 1635–1646.

Tieleman, H. W., R. Akins, and P. Sparks (1981, July). A comparison of wind-tunnel and full-scale wind pressure measurements on low-rise structures. *Journal of Wind Engineering and Industrial Aerodynamics 8*(1-2), 3–19.

Tieleman, H. W., M. Elsayed, and M. Hajj (2006, July). Peak Wind Load Comparison: Theoretical Estimates and ASCE 7. *Journal of Structural Engineering 132*(7), 1150–1157.

Tieleman, H. W., Z. Ge, and M. R. Hajj (2007, February). Theoretically estimated peak wind loads. *Journal of Wind Engineering and Industrial Aerodynamics 95*(2), 113–132.

Vazzana, G., F. Ricciardelli, A. Zasso, and S. Giappino (2013). Wind tunnel measurement of internal and external pressures on a rectangular low-rise building with different opening patterns. In *6th European and African Conference on Wind Engineering EACWE 6, 7th-11th July 2013*, pp. 1–8.

Versteeg, H. K. (2007). *An introduction to computational fluid dynamics : the finite volume method*. Harlow, England New York: Pearson Education Ltd.

Winterstein, S. R. and T. Kashef (2000, May). Moment-Based Load and Response Models With Wind Engineering Applications. *Journal of Solar Energy Engineering 122*(3), 122–128.

Winterstein, S. R. and C. A. MacKenzie (2013, February). Extremes of Nonlinear Vibration: Comparing Models Based on Moments, L-Moments, and Maximum Entropy. *Journal of Offshore Mechanics and Arctic Engineering 135*(2), 21602.

Xie, Z. T. and I. P. Castro (2008). Efficient generation of inflow conditions for large eddy simulation of street-scale flows. *Flow, Turbulence and Combustion 81*, 449–470.

Yang, L., K. R. Gurley, and D. O. Prevatt (2013, March). Probabilistic modeling of wind pressure on low-rise buildings. *Journal of Wind Engineering and Industrial Aerodynamics 114*, 18–26.

Zasso, A., D. Rocchi, and P. Schito (2009). Experimental and numerical study of the flow around a low rise building (CC). In *EACWE 5*, Number July.